

VOL.107 NO.WW3. AUG. 1981

JOURNAL OF THE WATERWAY PORT COASTAL AND OCEAN DIVISION

PROCEEDINGS OF
THE AMERICAN SOCIETY
OF CIVIL ENGINEERS





VOL.107 NO.WW3. AUG. 1981

JOURNAL OF THE WATERWAY PORT COASTAL AND OCEAN DIVISION

PROCEEDINGS OF
THE AMERICAN SOCIETY
OF CIVIL ENGINEERS



Charles B. Chesnutt
U.S. Army Coastal Engineering
Research Center

Copyright© 1981 by
American Society
of Civil Engineers
All Rights Reserved
ISSN 0148-9895

AMERICAN SOCIETY OF CIVIL ENGINEERS

BOARD OF DIRECTION

President

Irvan F. Mendenhall

Past President

Joseph S. Ward

President Elect

James R. Sims

Vice Presidents

Robert D. Bay
Francis J. Connell

Lyman R. Gillis
Albert A. Grant

Directors

Martin G. Abegg	Paul R. Munger
Floyd A. Bishop	William R. Neuman
L. Gary Byrd	Leonard S. Oberman
Larry J. Feeser	John D. Parkhurst
John A. Focht, Jr.	Celestino R. Pennoni
Sergio Gonzalez-Karg	Robert B. Rhode
James E. Humphrey, Jr.	S. Russell Stearns
Richard W. Karn	William H. Taylor
Leon D. Luck	Stafford E. Thornton
Arthur R. McDaniel	Robert E. Whiteside
Richard S. Woodruff	

EXECUTIVE OFFICERS

Eugene Zwayer, *Executive Director*
Julie E. Gibouleau, *Assistant to the Executive Director*
Louis L. Meier, *Washington Counsel/Assistant Secretary*
William H. Wisely, *Executive Director Emeritus*
Michael N. Saigo, *Treasurer*
Elmer B. Isaak, *Assistant Treasurer*

STAFF DIRECTORS

Donald A. Buzzell, *Managing Director for Education and Professional Affairs*
Robert A. Crist, Jr., *Managing Director for Publications and Technical Affairs*
Alexandra Bellcw, *Director, Human Resources*
David Dresia, *Director, Publications Production and Marketing*
Barker D. Herr, *Director, Membership*
Richard A. Jeffers, *Controller*
Carl E. Nelson, *Director, Field Services*
Don P. Reynolds, *Director, Policy, Planning and Public Affairs*

Bruce Rickerson, *Director, Legislative Services*
Albert W. Turchick, *Director, Technical Services*

George K. Wadlin, *Director, Education Services*

R. Lawrence Whipple, *Director, Engineering Management Services*

COMMITTEE ON PUBLICATIONS

Stafford E. Thornton, <i>Chairman</i>	
Martin G. Abegg	Richard W. Karn
John A. Focht, Jr.	Paul R. Munger
William R. Neuman	

WATERWAY, PORT, COASTAL AND OCEAN DIVISION

Executive Committee

George M. Watts, <i>Chairman</i>	
J. Richard Weggel, <i>Vice Chairman</i>	
Jon T. Moore	William J. Nordell
William F. Baird, <i>Secretary</i>	
Austin Brant, Jr., <i>Management Group D Contact Member</i>	

Publications Committee

Charles B. Chesnutt, <i>Chairman and Editor</i>	
Yuan Jen, <i>Vice Chairman</i>	J. J. Lee
John A. Armstrong	Jerry Machemehl
Subrata Chakrabarti	Thomas Prokrefke
John Franco	J. R. Weggel
Robert T. Hudspeth	Robert W. Whalin
Theodore R. Kretschmer	

PUBLICATION SERVICES DEPARTMENT

David Dresia, *Director, Publications Production and Marketing*

Technical and Professional Publications

Richard R. Torrens, *Manager*
Chuck Wahrhaftig, *Chief Copy Editor*
Corinne Bernstein, *Copy Editor*
Linda Ellington, *Copy Editor*
Shiela Menaker, *Production Co-ordinator*
Richard C. Scheblein, *Draftsman*

Information Services

Elan Garonzik, *Editor*

PERMISSION TO PHOTOCOPY JOURNAL PAPERS

Permission to photocopy for personal or internal reference beyond the limits in Sections 107 and 108 of the U.S. Copyright Law is granted by the American Society of Civil Engineers for libraries and other users registered with the Copyright Clearance Center, 21 Congress Street, Salem, Mass. 01970, provided the appropriate fee is paid to the CCC for all articles bearing the CCC code. Requests for special permission or bulk copying should be addressed to the Manager of Technical and Professional Publications, American Society of Civil Engineers.

CONTENTS

Plume Development using a Lagrangian Marker Method <i>by Gordon J. Oman and Michael Sydor</i>	131
Distribution of Crest-to-Trough Wave Heights <i>by M. Aziz Tayfun</i>	149
Extended Velocity Potential Wave Kinematics <i>by Kostas F. Lambrakos</i>	159
Oscillatory Rough Turbulent Boundary Layers <i>by Iver Brevik</i>	175

TECHNICAL NOTES

Proc. Paper 16414

Linearized Solution to Inlet Equation with Inertia <i>by Todd L. Walton, Jr. and Francis F. Escoffier</i>	191
---	-----

The Journal of the Waterway, Port, Coastal and Ocean Division (ISSN 0148-9895) is published quarterly by the American Society of Civil Engineers. Publications office is at 345 East 47th Street, New York, N.Y. 10017. Address all ASCE correspondence to the Editorial and General Offices at 345 East 47th Street, New York, N.Y. 10017. Allow six weeks for change of address to become effective. Subscription price to members is \$8.00. Nonmember subscriptions available; prices obtainable on request. Second-class postage paid at New York, N.Y. and at additional mailing offices. WW.

POSTMASTER: Send address changes to American Society of Civil Engineers, 345 East 47th Street, New York, NY 10017.

The Society is not responsible for any statement made or opinion expressed in its publications.

Stability of Rubble Mound Breakwaters <i>by Todd L. Walton, Jr. and J. Richard Weggles</i>	195
--	-----

Particle Motion under Stokes Waves <i>by Eliezer Kit and Michael Stiassnie</i>	202
--	-----

DISCUSSION

Proc. Paper 16411

Mixing of Buoyant Surface Jet over Sloping Bottom , by Bijan Safaie (Nov., 1979, Prior Discussions: Nov., 1980). <i>closure</i>	207
--	-----

Inlet Stability Solutions for Tributary Inflow , by Francis F. Escoffier and Todd L. Walton, Jr. (Nov., 1979, Prior Discussions: Nov., 1980, Feb., 1981). <i>closure</i>	208
--	-----

Wave Force Analysis: An Alternate Procedure , by Yuan Yen (Feb., 1980, Prior Discussions: Feb., 1981). <i>closure</i>	209
--	-----

Perturbation Methods in Diffraction , by John V. Wehausen (May, 1980, Prior Discussions: Feb., 1981). <i>closure</i>	210
---	-----

Wave Population of Spar Buoys,* by Thomas A. McClimans (Aug., 1980). <i>by R. M. Carson</i>	211
--	-----

Longshore Currents with Wave Current Interaction,* by Robert A. Dalrymple (Aug., 1980). <i>by A. Swain</i>	213
---	-----

Water Level Variations along California Coast,* by Raymond A. Smith and Robert J. Leffler (Aug., 1980). <i>by Morrough P. O'Brien</i>	216
--	-----

Knickpoint Migration due to Baselevel Lowering,* by Ze'ev B. Begin, David F. Meyer, and Stanley A. Schumm (Aug., 1980). <i>by Saburo Komura</i>	218
--	-----

*Discussion period closed for this paper. Any other discussion received during this discussion period will be published in subsequent Journals.

INFORMATION RETRIEVAL

The key words, abstract, and reference "cards" for each article in this Journal represent part of the ASCE participation in the EJC information retrieval plan. The retrieval data are placed herein so that each can be cut out, placed on a 3 × 5 card and given an accession number for the user's file. The accession number is then entered on key word cards so that the user can subsequently match key words to choose the articles he wishes. Details of this program were given in an August, 1962 article in CIVIL ENGINEERING, reprints of which are available on request to ASCE headquarters.

*Discussion period closed for this paper. Any other discussion received during this discussion period will be published in subsequent Journals.

U.S. CUSTOMARY-SI CONVERSION FACTORS

In accordance with the October, 1970 action of the ASCE Board of Direction, which stated that all publications of the Society should list all measurements in both U.S. Customary and SI (International System) units, the following list contains conversion factors to enable readers to compute the SI unit values of measurements. A complete guide to the SI system and its use has been published by the American Society for Testing and Materials. Copies of this publication (ASTM E-380) can be purchased from ASCE at a price of \$3.00 each; orders must be prepaid.

All authors of *Journal* papers are being asked to prepare their papers in this dual-unit format. To provide preliminary assistance to authors, the following list of conversion factors and guides are recommended by the ASCE Committee on Metrication.

To convert	To	Multiply by
inches (in.)	millimeters (mm)	25.4
feet (ft)	meters (m)	0.305
yards (yd)	meters (m)	0.914
miles (miles)	kilometers (km)	1.61
square inches (sq in.)	square millimeters (mm ²)	645
square feet (sq ft)	square meters (m ²)	0.093
square yards (sq yd)	square meters (m ²)	0.836
square miles (sq miles)	square kilometers (km ²)	2.59
acres (acre)	hectares (ha)	0.405
cubic inches (cu in.)	cubic millimeters (mm ³)	16,400
cubic feet (cu ft)	cubic meters (m ³)	0.028
cubic yards (cu yd)	cubic meters (m ³)	0.765
pounds (lb) mass	kilograms (kg)	0.453
tons (ton) mass	kilograms (kg)	907
pound force (lbf)	newtons (N)	4.45
kilogram force (kgf)	newtons (N)	9.81
pounds per square foot (psf)	pascals (Pa)	47.9
pounds per square inch (psi)	kilopascals (kPa)	6.89
U.S. gallons (gal)	liters (L)	3.79
acre-feet (acre-ft)	cubic meters (m ³)	1,233

16462 PLUME DEVELOPMENT

KEY WORDS: Currents (water); Dispersion; Lagrangian functions; Lake Superior; Numerical analysis; Plumes; Remote sensing; Runoff; Sedimentation; Suspended solids; Turbidity; Water pollution; Water pollution effects; Wind direction

ABSTRACT: Currents as a function of wind were calculated by a depth integrated model of Lake Superior. Using the calculated currents, the development of large turbidity plume was numerically simulated. Good agreement between the simulated plume, remote sensing, and ground truth data provided verification of calculated current patterns and much insight into the ultimate fate of pollutants in western Lake Superior as a function of wind. The long range transport of a conservative pollutant from the Duluth-Superior harbor was simulated for westerly winds and for variable winds. For westerly winds, the model predicted that the contaminant would be transported along the Wisconsin shore away from the harbor area. For variable winds, the pollutant remained trapped in the southwest corner of the lake.

REFERENCE: Oman, Gordon J. (Assoc. Scientist, Dept. of Physics, Univ. of Minnesota at Duluth, Duluth, Minn. 55812), and Sydor, Michael, "Plume Development Using a Lagrangian Marker Method," *Journal of the Waterway, Port, Coastal and Ocean Division*, ASCE, Vol. 107, No. WW3, **Proc. Paper 16462**, August, 1981, pp. 131-148

16460 DISTRIBUTION OF CREST-TO-TROUGH WAVE HEIGHTS

KEY WORDS: Field data; Probability density functions; Probability distribution functions; Rayleigh waves; Troughs; Wave height; Wave measurement; Wave spectrum

ABSTRACT: The theoretical distribution of wave heights as given by the Rayleigh law is based on the wave envelope. However, empirical distributions derived from field data utilize a crest-to-trough representation. The latter definition corresponds to an averaging operation on the envelope which results in an excess of waves with heights near the midrange and in deficiencies at the two extremes in a manner increasing with the spectrum band width. The ultimate effect of a deficiency towards the high wave tail is an underestimate in the exceeding probability of larger wave heights. Hence, this kind of discrepancy (systematically observed between the Rayleigh law and various field data) can be explained on this basis.

REFERENCE: Tayfun, M. Aziz (Assoc. Prof., Civ. Engrg. Dept., Kuwait Univ., P.O. Box 5969, Kuwait), "Distribution of Crest-to-Trough Wave Heights," *Journal of the Waterway, Port, Coastal and Ocean Division*, ASCE, Vol. 107, No. WW3, **Proc. Paper 16460**, August, 1981, pp. 149-158

16461 EXTENDED VELOCITY POTENTIAL WAVE KINEMATICS

KEY WORDS: Boundary conditions; Coastal engineering; Deformation; Fourier series; Ocean engineering; Stokes law; Velocity; Water depth; Wave height; Wave period; Waves (water); Wave velocity

ABSTRACT: A double Fourier series expansion of the velocity potential for water waves was used to treat nonlinear single harmonic waves and irregular waves measured in the ocean test structure experiment. The (extended) velocity potential (EXVP) satisfies the governing hydrodynamic equations in the body of the water and matches the boundary conditions at the waves surface in the least-squares sense. The waves that are treatable with this velocity procedure can have a range of crest values for a specified wave height, period and water depth. In contrast, the common Stokes velocity procedures can treat only waves of fixed crest, for a given wave height, period and water depth. The water velocities measured for irregular waves in the ocean test structure experiment are in good agreement with the velocities predicted by this procedure; these correlations are significantly better than velocity correlations with the Stokes wave representation.

REFERENCE: Lambrakos, Kostas F. (Sr. Research Specialist, Exxon Production Research Co., Houston, Tex. 77001), "Extended Velocity Potential Wave Kinematics," *Journal of the Waterway, Port, Coastal and Ocean Division*, ASCE, Vol. 107, No. WW3, **Proc. Paper 16461**, August, 1981, pp. 159-174

16478 OSCILLATORY ROUGH TURBULENT BOUNDARY LAYERS

KEY WORDS: Boundary layer; Fluid mechanics; **Hydrodynamics;** Laboratory tests; **Mathematical analysis; Mathematical models; Turbulence;** **Turbulent boundary layers;** Turbulent flow; **Water flow**

ABSTRACT: Kajiura's three-layer model (1968) of an oscillatory rough turbulent layer is simplified to a two-layer model. This model consists of an overlap layer in which the turbulent viscosity varies linearly with height, and an outer layer in which the viscosity is constant. The analytic expressions are compared with Jonsson's Test No. 1 (1963, 1976, 1980). Reasonable agreement between theory and experiment is found, thus supporting the usefulness of the two-layer model.

REFERENCE: Brevik, Iver (Lect., Division of Port and Ocean Engineering, University of Trondheim, Trondheim, Norway), "Oscillatory Rough Turbulent Boundary Layers," *Journal of the Waterway, Port, Coastal and Ocean Division, ASCE*, Vol. 107, No. WW3, **Proc. Paper 16478**, August, 1981, pp. 175-188

PLUME DEVELOPMENT USING LAGRANGIAN MARKER METHOD

By Gordon J. Oman¹ and Michael Sydor²

INTRODUCTION

Numerical lake models are normally tested by comparing their results with measured currents. Extensive current measurements are generally needed to distinguish general current patterns from locally generated turbulences. When modeling a particular event, such measurements are costly and difficult to obtain. Sequential remote sensing data on the transport of a large turbidity plume provides an alternative to extensive current measurements. In the past, remote sensing data has been used to qualitatively verify calculated current patterns in western Lake Superior for various winds (3). In order to more fully utilize the potential of remote sensing data as a means of verification of calculated current patterns, we numerically simulated the development and transport of the 1976 spring runoff plume from the Nemadji River, Wisconsin (Fig. 1).

The use of plume simulation as a means of verifying calculated current patterns requires an accurate numerical solution of the equations which govern the transport and diffusion of turbidity and a detailed knowledge of all major sources and sinks of turbidity. Most numerical solutions of advection suffer from distortion near the edge of the plume where concentration gradients are necessarily large. In a first attempt at plume simulation, an explicit integration of the advection-diffusion equation was used. The problem of distortion was alleviated by use of upstream concentration gradients at all points, but the numerical scheme still suffered from excessive dispersion at the edge of the plume. In order to avoid this problem a Lagrangian marker technique was tried (14). This solution technique was ideally suited for modeling of a point source of pollution and proved capable of handling large concentration gradients without significant distortion.

Accurate plume simulation also requires a detailed knowledge of the major sources and sinks of turbidity. The major sources of red clay turbidity in western Lake Superior are shore erosion, resuspension, and river runoff (16,21). During the 1976 spring runoff period, March 31–April 6, river runoff was the most

¹ Assoc. Scientist, Dept. of Physics, Univ. of Minnesota at Duluth, Duluth, Minn. 55812.

² Prof., Dept. of Physics, Univ. of Minnesota at Duluth, Duluth, Minn. 55812.

Note.—Discussion open until January 1, 1982. To extend the closing date one month, a written request must be filed with the Manager of Technical and Professional Publications, ASCE. Manuscript was submitted for review for possible publication on April 15, 1980. This paper is part of the Journal of the Waterway, Port, Coastal and Ocean Division, Proceedings of the American Society of Civil Engineers, ©ASCE, Vol. 107, No. WW3, August, 1981. ISSN 0148-9895/81/0003-0131/\$01.00.

significant source of lake turbidity. A protective ice shelf and mild weather prevented substantial shore erosion, and strong northeasterly winds needed to generate significant resuspension occurred only on April 3. The Nemadji River puts out about 90% of all suspended solids from river runoff in the extreme western arm of Lake Superior. As part of our effort for PLUARG (Pollution from Land Use Activities Reference) we monitored the 1976 spring runoff peak of the Nemadji (18). These observations together with a rough approximation of resuspension on April 3 made possible a fairly accurate simulation of the major sources of lake turbidity. The only sink of lake turbidity is settling. Consecutive Landsat images on April 5 and April 6 indicated the settling rate was about 6% per day during the runoff period. This settling rate is consistent with past observations.



FIG. 1.—Extreme Western Lake Superior: Study Area

In large lakes the horizontal movement of contaminants is dominated by advection (4,6). In a number of model studies, including the present one, horizontal diffusion has had little effect upon model predictions (4,7,11). Since our plume simulation model incorporates an accurate, unconditionally stable numerical solution of the advection diffusion equation with a detailed knowledge of the major sources and sinks of turbidity, its accuracy should therefore depend primarily upon the accuracy of the current patterns it employs. An accurate simulation of plume development would confirm calculated current patterns.

Numerical simulation of turbidity transport is useful in other ways. Suspended red clay is one of the major pollutants in western Lake Superior. In addition, the highly turbid water from the Nemadji River is easily detectable in Landsat satellite images and serves as a natural tracer for water from the Duluth-Superior

harbor. Together with the St. Louis River, the Duluth-Superior harbor constitutes the major United States source of man-made pollution into Lake Superior. Numerical simulation of plume development yields a better understanding of the processes involved in pollutant transport and provides much insight into the ultimate fate of pollutants as a function of wind.

RUNOFF MONITORING

The 1976 spring runoff of the Nemadji River was monitored by several groups under project PLUARG. High altitude manned overflights by NASA's Lewis Research Center, Cleveland, Ohio, provided multispectral remote sensing data of western Lake Superior on April 1, 2, 4, 5, 6. The western arm of the lake was also visible in consecutive Landsat satellite images on April 5 and 6. Water samples were taken by ship cruises on March 31, and April 1, 4, 5, and 6.

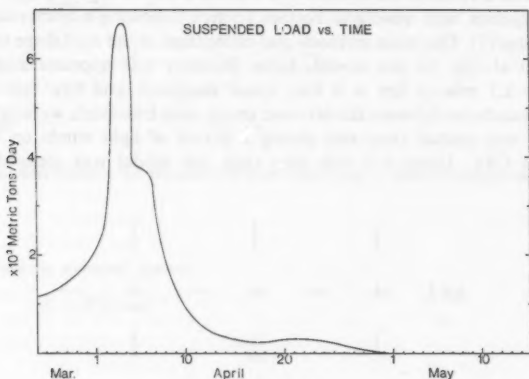


FIG. 2.—Suspended Load Output of Nemadji River

Sampling stations were distributed to monitor conditions representative of clean lake water, St. Louis River effluent, Nemadji River effluent, and lake water along the Wisconsin shore affected by resuspension, erosion, and output from minor rivers. At each station vertical profiles of turbidity, temperature, and conductivity were measured. Samples were taken at the surface, the mid-secchi layer, and the bottom and later analyzed for suspended solids concentration and turbidity.

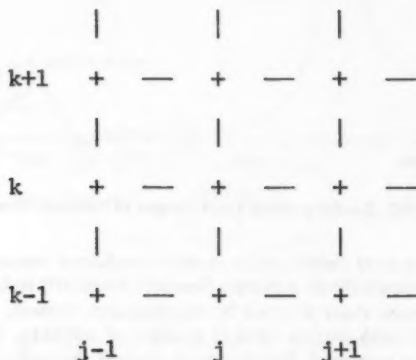
The data from the sampling cruises are tabulated by Sydor and Oman (18). As Storz et al. (16) have shown, suspended red clay concentrations in western Lake Superior and Landsat remote sensing data are extremely well correlated. Sydor and Oman (18) were also able to identify various types of particulates using Landsat data. In correlating their remote sensing data from April 1, 2, 4, 5, and 6 to measured concentrations of suspended solids, NASA's Lewis Research Center, obtained correlation coefficients varying between 0.93–0.99 (9). Because ground truth and remote sensing data correlated well, maps of

actual suspended red clay concentrations could be derived from remote sensing imagery.

Monitoring of the Nemadji River began in mid March. The river sampling station was located near South Superior, Wisconsin, at the upper end of the estuary zone. Measurements of suspended solids, stage, and flow rate were taken at least once every day during the entire runoff. The suspended load output of the river for the runoff was derived (Fig. 2). The total load output for the runoff was estimated at 60,000 metric tons. This figure pertains only to the red clay particles less than 60μ in diameter. Generally, particles smaller than 4μ comprise the major part of the immediate contaminant output into the lake.

HYDRODYNAMIC MODEL

Currents as a function of winds were calculated by a depth integrated model of Lake Superior with quadratic bottom friction following a numerical scheme by Leendertse (5). The basic methods and calibration of the model are considered by Diehl et al. (3). In this model, Lake Superior was approximated using a 3.7 mile \times 3.7 mile (6 km \times 6 km) space staggered grid like that shown in Fig. 3. At boundaries between the lake and shore, zero transports were maintained. The model was started from rest during a period of light winds on March 29 at 2200 hrs CST. Using a 5 min time step, the model was stepped forward to April 7.



| y component of current
 — x component of current
 + water level

FIG. 3.—Staggered Grid Employed in Lagrangian Marker Particle Model

Since no pronounced pressure system was evident during the runoff period, winds were the only driving force used in the model. National Oceanic and Atmospheric Administration (NOAA) wind data from seven stations around

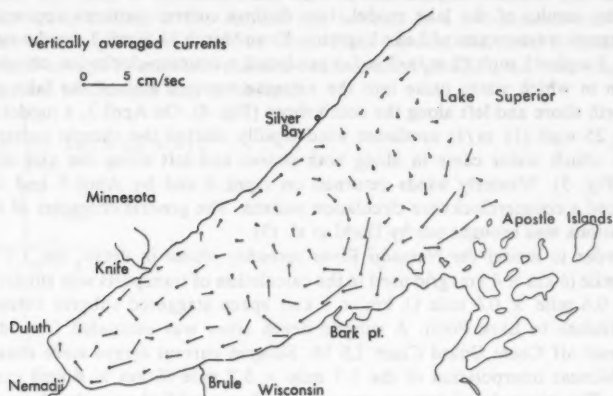


FIG. 4.—Current Pattern for Westerly Winds Predicted by Depth Integrated Transport Model

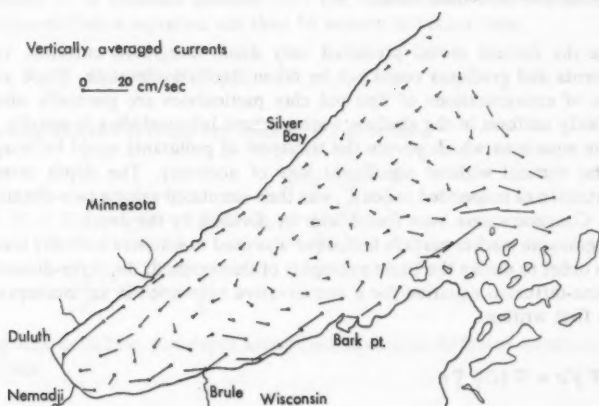


FIG. 5.—Current Pattern for Easterly Winds Predicted by Depth Integrated Transport Model

the lake were used. At each grid point the wind velocity was calculated taking a weighted average of the measured wind velocities using the squared reciprocal distance between the grid point and the stations as weighting factors. The surface stress was assumed proportional to the wind speed squared. The model was

calibrated by varying the wind stress coefficient so that the magnitude of predicted and measured water-level oscillations around the lake matched. Aircraft overflights, land sightings, and observations of the plumes during sampling cruises qualitatively verified the predicted transport directions.

In the results of the lake model, two distinct current patterns appeared in the extreme western arm of Lake Superior. From March 31–April 2, northwesterly winds 5 mph–15 mph (2 m/s–7 m/s) produced a counter-clockwise circulation pattern in which water came into the extreme western arm of the lake along the north shore and left along the south shore (Fig. 4). On April 3, a moderately strong 25 mph (11 m/s) northeast wind rapidly shifted the current pattern to one in which water came in along both shores and left along the axis of the lake (Fig. 5). Westerly winds returned on April 4 and by April 5 had again produced a counterclockwise circulation pattern. The general character of these circulations was brought out by Diehl et al. (3).

In order to model the Nemadji River turbidity plume in detail, the 3.7 mile \times 3.7 mile (6 km \times 6 km) grid used in the calculation of transports was subdivided into a 0.6 mile \times 0.6 mile (1 km \times 1 km) space staggered subgrid extending from Duluth to Bark Point. A subgrid depth array was estimated from depth data read off Coast Guard Chart LS 96. Subgrid current arrays were obtained from bilinear interpolation of the 3.7 mile \times 3.7 mile (6 km \times 6 km) current arrays. The interpolated current arrays were then modified to make them meet the continuity equation on a 0.6 mile \times 0.6 mile (1 km \times 1 km) basis.

LAGRANGIAN MARKER PARTICLE MODEL

Since the current model predicted only depth integrated currents, vertical movements and gradients could not be taken into consideration. Since vertical profiles of concentrations of fine red clay particulates are generally observed to be fairly uniform in the shallow waters where lake turbidity is usually found (16), the equations which govern the transport of pollutants could be integrated over the vertical without significant loss of accuracy. The depth integrated concentration of suspended solids C , was then simulated using a two-dimensional model. Concentrations were found later by dividing by the depth.

A Lagrangian marker particle technique was used to simulate turbidity transport (14). In order to derive the basic principles of this method, the three-dimensional advection-diffusion equation for a conservative substance in an incompressible fluid is first written:

$$\frac{\partial c}{\partial t} + \nabla \cdot \mathbf{V}c = \nabla \cdot [D] \nabla c \quad (1)$$

The diffusivity matrix D is assumed to be diagonal. Letting D_o denote the horizontal diffusivity, Eq. 1 can be integrated from the bottom $z = -H$ to the free surface $z = h$ using the hydrodynamic boundary conditions and the mathematical definitions of surface and bottom flux:

$$\frac{\partial}{\partial t} \int_{-H}^h c dz + \frac{\partial}{\partial x} \int_{-H}^h u c dz + \frac{\partial}{\partial y} \int_{-H}^h v c dz = \frac{\partial}{\partial x} \int_{-H}^h D_o \frac{\partial c}{\partial x} dz$$

$$+ \frac{\partial}{\partial y} \int_{-H}^h D_o \frac{\partial c}{\partial y} dz + S \dots \dots \dots (2)$$

In this equation, S represents the sum of the diffusive fluxes into and out of the water column at the surface and bottom. In a two-dimensional model, S can be thought of as a source term. Since vertical diffusion is assumed to be rapid enough to maintain uniform concentration profiles, the following depth integrated parameters may be defined:

$$C_s = \int_{-H}^h c dz = (H + h) C \dots \dots \dots (3a)$$

$$U = \frac{\int_{-H}^h u dz}{H + h} \dots \dots \dots (3b)$$

$$V = \frac{\int_{-H}^h v dz}{H + h} \dots \dots \dots (3c)$$

In these equations, C_s represents the depth integrated concentration; C = the depth averaged concentration; and U and V = the depth-averaged components of the current. Since $h \ll H$, $H + h$ may be replaced by H . The horizontal diffusivity D_o is assumed constant over the vertical axis. The two-dimensional advection-diffusion equation can then be written in vector form

$$\frac{\partial C_s}{\partial t} + \nabla_2 [V_2 C_s - D_o \cdot H \cdot \nabla_2 C] = S \dots \dots \dots (4)$$

Following Sklarew (13) the net velocity V_T is defined

$$\begin{aligned} V_T &= V_2 - D_o \frac{H \cdot \nabla_2 C}{C_s} = V_2 - D_o \frac{H \cdot \nabla_2 \frac{C_s}{H}}{C_s} \\ &= V_2 - D_o \frac{\nabla_2 C_s}{C_s} + D_o \frac{\nabla_2 H}{H} \dots \dots \dots (5) \end{aligned}$$

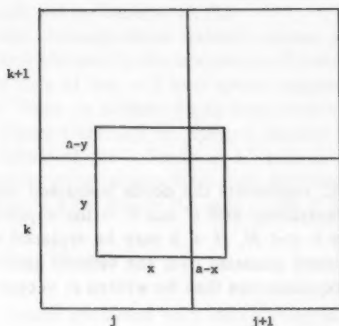
Using this definition the depth integrated advection-diffusion equation can be rewritten:

$$\frac{\partial C_s}{\partial t} + \nabla_2 V_T C_s = S \dots \dots \dots (6)$$

Eq. 6 has the following physical interpretation. The quantity C_s is being added at a rate specified by S and is then being moved with velocity V_T . This interpretation forms the basis of the Lagrangian marker particle method. In Eulerian methods, the region of interest is divided by a grid and contaminant concentration in each cell is tabulated. At each time step, material convected from neighboring cells is completely mixed within a given cell. This mixing

can lead to false numerical diffusion if an inaccurate formulation of the finite difference equation is used. Eulerian methods with little numerical diffusion often suffer from spurious oscillations near the edge of a plume where concentration gradients are large. The Lagrangian marker particle method solves this problem by dividing the contaminant load into a number of packets or marker particles. These particles are introduced into the lake at contaminant sources at a rate corresponding to contaminant loading and then allowed to move with the net transport velocity.

In the present model, the region of interest is first divided by a square Eulerian grid and the depths at the center of each grid square are specified. Locations of contaminant sources are specified and marker particles are introduced at these points. Each particle is assigned a size smaller than the Eulerian grid



Cell	C_{jk}	C_{j+1k}	C_{jk+1}	C_{j+1k+1}
Contribution	$\frac{x \cdot y \cdot C_g}{g^2 \cdot H_{jk}}$	$\frac{(a-x) \cdot y \cdot C_g}{g^2 \cdot H_{j+1k}}$	$\frac{x \cdot (a-y) \cdot C_g}{g^2 \cdot H_{jk+1}}$	$\frac{(a-x) \cdot (a-y) \cdot C_g}{g^2 \cdot H_{j+1k+1}}$

FIG. 6.—Contribution of Single Marker Particle of Size a to Four Concentration Cells of Size g

size and a depth integrated concentration. A marker particle may be thought of as a small square moving around in a square Eulerian grid. At each time step, a depth-integrated concentration array is derived from the locations, sizes, and depth-integrated concentrations of the marker particles. In this calculation, the contribution of a marker particle to a Eulerian grid square is given by the product of the area of overlap and the depth integrated concentration of the marker particle (Fig. 6).

The contribution of diffusion to the net transport velocity is then added to currents provided by the hydrodynamic model. Because the grid is staggered in space, whenever C_g or H in Eq. 5 is zero, its corresponding derivative is also zero and the quotient is set to zero. The marker particles are then moved

by the net transport velocity. A corrective scheme is used to assure marker particles move with the current. If the position of a particle is given by \underline{R}_{old} , the current \underline{V}_{old} is found by bilinear interpolation of current arrays. An intermediate position \underline{R}^* is found first:

$$\underline{R}^* = \underline{R}_{old} + \Delta t \cdot \underline{V}_{old} \quad (7)$$

The velocity at the intermediate position \underline{V}^* is found by interpolation and the new particle position \underline{R}_{new} is found by Eq. 8:

$$\underline{R}_{new} = \underline{R}_{old} + \frac{\Delta t}{2} (\underline{V}_{old} + \underline{V}^*) \quad (8)$$

This iterative scheme has been shown to greatly improve the accuracy of particle trajectories.

In addition, marker particles were allowed to expand or contract depending on whether they were above or below background concentrations. Based upon analogy with an analytic solution of diffusion of a square patch (15), the size of a marker particle A was approximated by a function of the particles initial size A_o , the time elapsed t , and the horizontal diffusivity D_o :

$$A^2 = 6 D_o t + A_o^2 = 6 D_o (t + t_o) \quad (9)$$

Differentiating Eq. 9 with respect to time gives

$$\frac{\partial A}{\partial t} = \frac{3 D_o}{A} \quad (10)$$

The background concentration C_b was defined as the average of the four closest elements of the concentration array. The change in size of the particle was given by a function of C_b and the concentration of the particle C_s :

$$\Delta A = \frac{C_s - C_b}{C_s} \left(\frac{3 D_o}{A} \right) \Delta t \quad (11)$$

In order to avoid numerical difficulties when A approaches zero in Eq. 11, particles were never allowed to get smaller than an eighth of the Eulerian grid size. If particles became larger than the Eulerian grid size, they were subdivided to make four new particles. This scheme made possible a more accurate representation of the dilute fringes of the plume.

With the new particle positions and sizes, a new concentration array is derived and the whole procedure is repeated. This numerical scheme was capable of accurately modeling a runoff plume at all stages of development with a limited number of particles and a limited amount of computer time (about 10 min on a CDC CYBER 74 for a one month simulation).

PLUME SIMULATION STUDIES

Observation of individual patches in consecutive Landsat images on April 5 and 6 made possible direct measurements of horizontal diffusivity and settling rates (12). Based upon these studies, a constant horizontal diffusivity of 11 sq ft/sec (1 m²/s) was used in plume simulation. This figure is consistent with empirical formulas for horizontal diffusivity (8).

Using currents predicted by the hydrodynamic model, the 1976 spring runoff plume of the Nemadji River was numerically simulated. The marker particle model was started on March 31 at 0000 CST and integrated using a 30 min time step. Marker particles were introduced every time step. The suspended load input at the Superior entry followed and measured output of the Nemadji for the 1976 spring runoff. Based on studies of the 1975 spring runoff (21), a suspended load equal to 5% of the Nemadji output was introduced at the mouth of the Amnicon River. Input prior to March 31 was approximated by an initial 3,728 tons at the mouth of the Poplar River, 1,912 tons at the mouth of the Amnicon, and 4,875 tons at the Superior entry. A settling rate of 6% per day was allowed during the peak runoff period. Since high turbulence and resuspension are associated with strong northeast winds (21), all previously

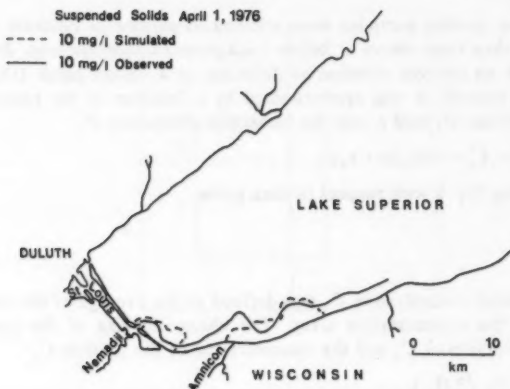


FIG. 7.—Simulated Turbidity Plume (Broken Line) 10 mg/L Concentration Contour for April 1, 1976, Compared to Surface Suspended Solids Concentration (Solid Line) Obtained from Manned Overflight Multispectral Data in Correlation with Sampling Measurements (Simulated Plume Takes Only Sources at Nemadji and Amnicon Rivers into Consideration)

settled material up to a maximum of 50 metric tons per grid square was resuspended at noon on April 3. Since a protective ice shelf prevented significant erosion during the runoff peak, this scheme of introducing and removing suspended load accounted for most of the major sources and sinks in the western arm of the lake. Some material in the actual plume came from resuspension of residual material along the Wisconsin shore. This source was neglected.

The predicted plume followed the observed plume reasonably well. From March 31 to April 2 the predicted plume (Fig. 7) filled the southern corner of the lake, as was anticipated from currents shown in Fig. 5. The NASA overflights and boat observations from that time showed a well-defined high density plume moving south along the shore. On April 4, the model and manned overflights clearly showed (Figs. 8 and 9) the sweeping of the plume straight out along the axis of the lake following the northeast winds on April 3.

Subsequently, as the westerly wind returned, the plume broadened and began moving east. The predicted plume for April 6, (Fig. 10) displayed many of the features observed in the Landsat satellite image for that day. The observed

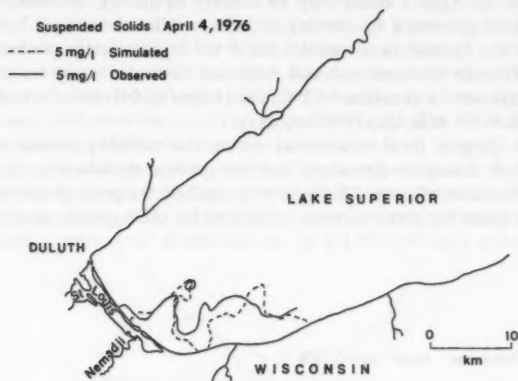


FIG. 8.—Simulated Plume for April 4, 1976 (Broken Line) and Surface Suspended Solids (Solid Line) from Manned Overflights, Compared at 5 mg/L Concentrations

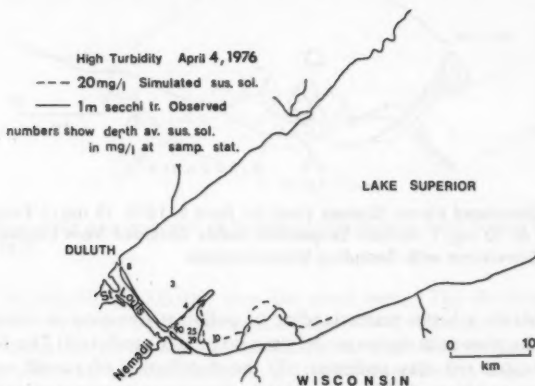


FIG. 9.—High Density Suspended Solids Simulated Plume (Solid Line) for 20 mg/L Concentration, Compared with High Density Plume Represented by 1 m Secchi Transparency Contour (Broken Line) from Manned Overflights in Correlation with Sampling Data (Numbers Represent Averages of Surface, Mid-secchi and Bottom Suspended Solids Concentrations at Sampling Stations)

plume, however, contains a certain amount of material originating from resuspension along the south shore which, as pointed out, could not be simulated for lack of data. The total suspended load in the Landsat image on April 6, 29,000

tons, agreed well with the 27,000 tons in the simulated plume.

A number of factors contributed to the differences in the observed and predicted contour lines in Figs. 7-10. First, the initial distribution of turbidity and resuspension on April 3 could only be crudely estimated. Second, features in the real plume generated by current patterns smaller than the 3.7-mile (6-km) grid size of the hydrodynamic model could not be accurately predicted. Third, a small difference between real and predicted currents would be amplified in time. For instance, a constant 0.03 ft/sec (1 cm/s) difference would shift the plume position 0.5 mile/day (0.9 km/day).

However, despite these sources of error, the turbidity model realistically predicted both transport directions and the general distribution of suspended solids as a function of time. This accuracy verified the general current patterns but not the point by point currents predicted by the hydrodynamic model. In



FIG. 10.—Simulated Plume (Broken Line) for April 6, 1976, 10 mg/L Concentration Compared to 10 mg/L Surface Suspended Solids Obtained from Landsat Data for April 6 in Correlation with Sampling Measurements

order to obtain a better understanding of pollutant transport in western Lake Superior, the plume simulation model was also used to predict: (1) The distribution of accumulated red clay sediment; (2) the distribution of runoff water from the St. Louis and Nemadji Rivers; and (3) the long-range transport of contaminants from the Duluth-Superior harbor.

The distribution of sediment accumulation is important because resuspension of previously settled material is one of the major causes of poor water quality in western Lake Superior. Resuspension appears to be largely confined to an area along the Wisconsin shore east of the Superior entry. Generally, the near-shore zone up to a depth of 65 ft (20 m) is scoured (1,2) with the exception of the area east of Wisconsin Point where thick deposits of red clay are found in shallower waters. The predicted distribution of accumulated sediment on April 6 (Fig. 11) is consistent with these observations. The area of maximum

deposition of sediment east of Wisconsin Point was the result of an eddy circulation in the southern corner of the lake. Since the near shore zone is scoured, about 50% of the runoff sediment would later be resuspended and moved to deeper parts of the lake.

In a second application of the model, the discharge from the St. Louis and Nemadji Rivers was traced in order to simulate the transport of a conservative pollutant from each of these rivers. The model was modified to keep track of the fraction of river water in the water column. For the Nemadji, the input at the south entry followed the river's measured discharge. The initial distribution was approximated by 14,000,000 cu yd (11,000,000 m³) of Nemadji water near the south entry. Based upon the results of a numerical model of the harbor (19), 60% of the St. Louis River's measured discharge was loaded at the north entry and the remaining 40% at the south entry. The initial distribution of St. Louis effluent consisted of 41,000,000 cu yd (31,000,000 m³) near the north

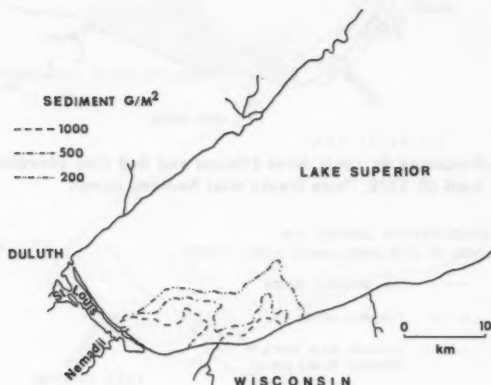


FIG. 11.—Simulated Accumulation of Sediment Distribution from Spring Runoff up to April 6, 1976

entry and 26,000,000 (20,000,000) near the south entry. The discharges from each of these two rivers during the peak of the 1976 spring runoff were traced separately using the seven days of calculated currents. The results compared reasonably well with Landsat imagery and field observations. Fig. 12 shows calculated lines of 10% St. Louis River water and the 5 mg/L suspended solids line for simulated variable wind conditions three weeks after the spring runoff of the Nemadji River.

In a third application of the model, the long-range transport of contaminants in western Lake Superior was simulated by tracing St. Louis and Nemadji River waters for one month. In order to reduce costs, the time step was increased to 2 hr. Based upon past studies, the settling rate was increased to 15% (21). Two cases were run. In one case, the seven days of calculated currents were recycled, in effect simulating one month of transports which could arise as the result of variable winds. In the second case, only current patterns driven

by westerly wind patterns were used. The results for simulated effluent dispersion for both cases are shown in Fig. 13. In the case of variable winds, the runoff remained west of the Brule River. It is anticipated that the effluent would

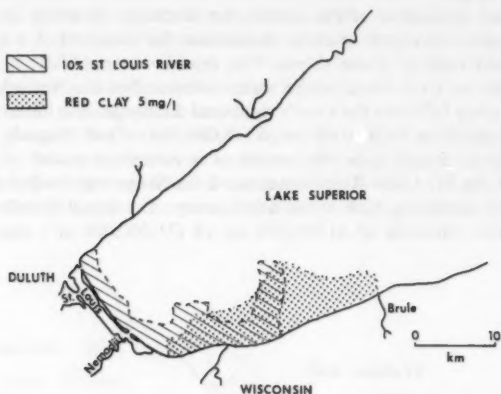


FIG. 12.—Simulated St. Louis River Effluent and Red Clay Distribution for Variable Winds on April 20, 1976, Three Weeks after Nemadji Runoff

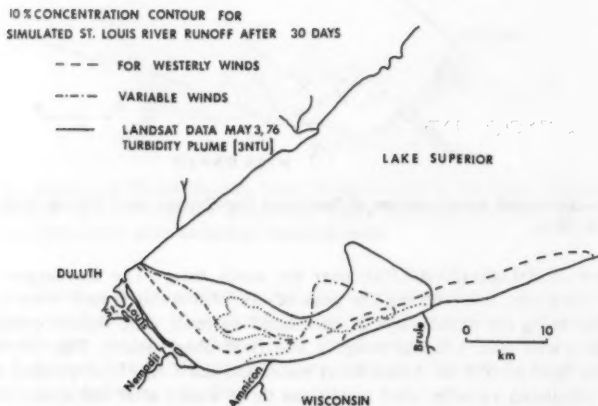


FIG. 13.—Simulated Distribution of Runoff from St. Louis One Month after Onset of Runoff: Broken Dotted Line Shows Contour for Variable Winds; Broken Line Shows Contaminant Distribution for Westerly Winds; and Solid Line Shows Outline of Turbidity Plume for May 3, 1976, One Month after 1976 Runoff

disperse slowly and remain in the Duluth area for extended periods of time. The tendency of contaminants to accumulate in the western arm of Lake Superior

has been inferred from the investigations by Ruschmeyer et al. (10). The apparent trapping of runoff water is also evident from Landsat images. In the case of westerly winds, St. Louis River water (Fig. 13), was transported along the Wisconsin shore, toward Bark Point (Fig. 4). Apparently easterly winds are needed to drive contaminants away from the south shore and trap them in the southwest corner of the lake.

Direct verification of the long-range dispersion of runoff cannot be made, since it would be cost prohibitive to run the model for thirty days of actual winds until the next useful Landsat image is available. However, an indication of whether the modeled results in Figs. 12 and 17 are realistic can be made from consideration of Landsat data. Using criteria developed from analysis of optical properties of the contaminants and correlation of Landsat multispectral data with ground truth observations (17,18,20), the distribution of runoff three weeks after the 1975 peak runoff of the Nemadji was derived (Fig. 14). The

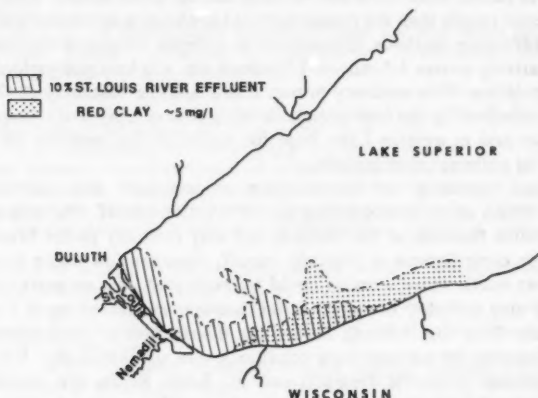


FIG. 14.—St. Louis River Effluent and Red Clay Concentration Three Weeks after 1975 Spring Runoff Obtained Using Landsat Data for May 18, 1975

1975 runoff occurred later in the season, and was larger than the 1976 runoff. However, the winds following the 1975 runoff were variable, and produced a distribution of red clay and St. Louis River runoff quite similar to the simulated distribution of these contaminants shown in Fig. 12 for comparable time and winds.

A rough check on the validity of the simulated runoff dispersion after one month can be made from examination of Landsat data for early May 1976. Fig. 13 shows a comparison of the simulated dispersion with the actual plume distribution on May 3 1976. The remnant red clay plume due to runoff, indicated in Fig. 13 by the turbidity hook (solid line) north of Brule River, is quite comparable to the simulated runoff plume shown by the dotted broken line. Both hooks have roughly 3 mg/L concentration of red clay. Comparison of the plumes in Fig. 13 near Duluth is not meaningful because strong northeast winds in late April 1976 generated significant shore erosion and resuspension. The simulated

plume density and the actual plume density for May 3, 1976 differ north of the Amnicon River because the simulated plume accounts only for turbidity due to runoff. The general character of confinement of the runoff in the area west of Brule River is still quite evident in the May 3, 1976 image. Landsat data and simulated results show that the lower contaminant concentration contours are confined to the area of the lake west of the line between Knife River, Minnesota, and Brule River, Wisconsin (Fig. 1). Comparison of lower concentration is, however, difficult because of the uncertainty in effluent identification.

CONCLUSIONS

The Lagrangian marker solution technique worked well in simulating both the development of the Nemadji red clay turbidity plume and the long-range transport of runoff water from the Nemadji and St. Louis Rivers. This technique yielded better results than the straightforward application of mixing and diffusion in finite difference methods. Currents from a depth integrated transport model with a relatively coarse 3.7 mile \times 3.7 mile (6 km \times 6 km) grid yielded accurate plume simulation. This accuracy in turn confirmed the reliability of the current patterns calculated by the lake model. Development of a layered transport model with a finer grid in western Lake Superior would further improve the accuracy of predicted pollutant distributions.

Numerical simulation of the transport of pollutants also answered many questions which arose in monitoring the 1976 spring runoff. The origin of many distinguishable features of the Nemadji red clay turbidity plume became clear. The relative contributions of Nemadji runoff, resuspension, shore erosion, and runoff from south shore streams could be estimated. We estimate about 65% of the red clay turbidity observed in the Landsat images of April 5 and April 6 1976 came from the Nemadji River. The distribution of contaminated water in Lake Superior for various wind conditions was also explained. For westerly winds, effluents from the Nemadji and St. Louis Rivers are carried out of western Lake Superior along the south shore. The onset of easterly winds generated eddy circulations which tend to trap these river effluents in the western arm of the lake. The model indicates a conservative contaminant from the St. Louis and Nemadji Rivers might not be flushed from the Duluth area until the severe storms of November change the prevailing current patterns.

ACKNOWLEDGMENTS

Our sincere thanks to Wayland Swain, U.S. E.P.A. Grosse Ile Laboratory for his work on plume sampling and for helpful discussions. We wish also to express our gratitude to Richard Gedney and Charles Raquet of N.A.S.A. Lewis Research Center for providing us with photographic renditions of multi-spectral images of the plumes. The processing of remote sensing data was performed by our colleague K. R. Stortz, his contribution to the program is gratefully acknowledged.

Research for this paper was supported in part by National Aeronautics and Space Administration (NASA) Grant NGL 24-005-263.

APPENDIX I.—REFERENCES

1. Bahnick, D. A., et al., "Effects of South Shore Drainage Basin and Clay Erosion on the Physical and Chemical Limnology of Western Lake Superior," *Proceeding of the 15th Conference on Great Lakes Research*, International Association for Great Lakes Research, 1972, pp. 237-248.
2. Bahnick, D. A., "Chemical Effects of Red Clay on Western Lake Superior," *Final Report U.S. E.P.A. Grant R-005169-01*, Department of Chemistry and Center for Lake Superior Environmental Studies, University of Wisconsin—Superior, 1976, 89 pp. plus 3 appendices.
3. Diehl, S. R., et al., "Transports in Lake Superior," *Journal of Geophysical Research*, Vol. 82, No. 6, 1977, pp. 977-78.
4. Katz, P. L., and Schwab, G. M., "Currents and Pollutant Dispersion in Lake Michigan, Modeled with Emphasis on the Calumet Region," *Research Report No. III*, University of Illinois at Urbana-Champaign, Water Resource Center, Mar., 1976.
5. Leendertse, J. J., "Aspects of a Computational Model for Long-Period Water-Wave Propagation," *Memorandum RM-5294*, The Rand Corporation, Santa Monica, Calif., 1967, 165 pp.
6. Leendertse, J. J., "A Water-Quality Simulation Model For Well-Mixed Estuaries and Coastal Seas: Volume I, Principles of Computation," *Memorandum RM-6230-RC*, The Rand Corporation, Santa Monica, Calif., 1970, 71 pp.
7. Lick, W., Paul, J., and Sheng, Y. P., "The Dispersion of Contaminants in the Near-Shore Region," *Modeling Bio Chemical Processes in Aquatic Ecosystems*, R. P. Canal, ed., Ann Arbor Science Publishers, Inc., Ann Arbor, Mich., 1976.
8. Murty, C. R., Kullenberg, G., Westenberg, H., and Miners, K. C., "Large Scale Diffusion Studies," *Canadian Center for Inland Waters Paper 14*, 1974, 14 pp.
9. Raquet, C. A., et al., "Coordinated Aircraft/Ship Surveys for Determining the Impact of River Inputs on Great Lakes Waters—Remote Sensing Results," Lewis Research Center, National Aeronautics and Space Administration, Cleveland, Ohio, 1977, 200 pp.
10. Ruschmeyer, O. R., et al., "Lake Superior Studies 1956-61," School of Public Health, University of Minnesota-Minneapolis, 1961.
11. Sheng, Y. P., and Lick, W., "Currents and Contaminant Dispersion in the Nearshore Region and Modification by a Jetport," *Journal of Great Lakes Research*, Vol. 4, No. 2, 1976, pp. 402-414.
12. Shuter, V., et al., "Turbidity Dispersion in Lake Superior Through Use of Landsat Data," *Journal of Great Lakes Research*, Vol. 4, No. 3-4, 1978, pp. 359-360.
13. Sklarew, R. C., Fabrik, A. J., and Prager, J. E., "A Particle-in-Cell Method for Solution of Atmospheric Diffusion Equation and Air Pollution Problems," *Report No. 35R-884*, Systems, Science, and Software, La Jolla, Calif., 1971.
14. Spaulding, M., "Numerical Modeling of Pollutant Transport Using a Lagrangian Marker Particle Technique," *NASA Technical Memorandum TMX-73930*, Langley Research Center, Hampton, Va., 1976, 33 pp.
15. Stakgold, I., *Boundary Value Problems of Mathematical Physics, Volume II*, Macmillan Co., New York, N.Y., 1968, pp. 59-60.
16. Stortz, K. R., Clapper, R. T., and Sydor, M., "Turbidity Sources in Lake Superior," *Journal of Great Lakes Research*, Vol. 2, No. 2, 1976, pp. 393-401.
17. Sydor, M., "Analysis of Suspended Solids in Lakes Using Landsat Multi-spectral Data," *Canadian Journal of Spectroscopy*, Vol. 73, No. 3, 1978, pp. 91-97.
18. Sydor, M., and Oman, G. J., "Effects of Nemadji Runoff on Lake Superior," *Final Report, U.S. E.P.A. Grant R-005286-01*, Department of Physics, University of Minnesota, Duluth, Minn., 1977, 197 pp.
19. Sydor, M., and Stortz, K. R., "Sources and Transports of Coal in the Duluth-Superior Harbor," *EPA-600/3-80-007*, Environmental Research Laboratory-Duluth, Duluth, Minn., Jan., 1980, 94 pp.
20. Sydor, M., Stortz, K. R., and Swain, W. R., "Identification of Contaminants in Lake Superior Through Landsat Data," *Journal of Great Lakes Research*, Vol. 4, No. 2, 1978, pp. 142-148.
21. Sydor, M., et al., "Red Clay Turbidity and its Transport in Western Lake Superior,"

Final Report U.S. E.P.A. Grant R-005175-01, Department of Physics, University of Minnesota-Duluth, 1979, 136 pp.

APPENDIX II.—NOTATION

The following symbols are used in this paper:

- A = marker particle size;
- A_o = initial size of marker particle before diffusive change;
- C = depth averaged concentration;
- C_b = background concentration for individual marker particle;
- C_s = depth integrated concentration;
- c = concentration of contaminant;
- $[D]$ = diffusivity matrix;
- D_o = horizontal diffusivity;
- H = undisturbed water depth;
- h = elevation of surface of water;
- R_{old} = marker particle position before translation by net transport current;
- R^* = first approximation of new marker particle net transport position;
- R_{new} = marker particle position after translation by current;
- t = time;
- U = depth averaged x component of current;
- u = x component of current;
- V = depth averaged y component of current;
- V_{old} = net transport current at R_{old} ;
- V^* = net transport current at R^* ;
- V = three-dimensional current;
- V_2 = depth averaged current;
- V_T = two-dimensional net transport current;
- v = y component of current;
- x, y = horizontal Cartesian coordinates;
- z = vertical Cartesian coordinate;
- ΔA = diffusive change in particle size;
- Δt = time increment;
- ∇ = three-dimensional divergence operation;
- $\bar{\nabla}$ = three-dimensional gradient operation;
- ∇_2 = two-dimensional divergence operation; and
- $\bar{\nabla}_2$ = two-dimensional gradient operation.

DISTRIBUTION OF CREST-TO-TROUGH WAVE HEIGHTS

By M. Aziz Tayfun,¹ A. M. ASCE

INTRODUCTION

It is known that the distribution of wave heights in a sea state is described well by the Rayleigh law under certain conditions. Specifically, it is assumed that the sea surface is linear Gaussian with a narrow-band spectrum. However, it is also known that the characteristics of a realistic wave field are not always consistent with these assumptions, and various discrepancies are often noted between field observations and the Rayleigh theory. Likely causes for these have been considered in a series of studies by Forristall (2), Nolte and Hsu (8), Longuet-Higgins (6), and the writer (9,10). They include: (1) The nonlinear, non-Gaussian characteristics of the sea surface; (2) effects associated with wide-band spectra; and (3) wave-breaking in deep and shallow water depths.

A further cause for the discrepancy between the Rayleigh law and empirical data is related to a difference in definitions. The Rayleigh distribution is especially relevant to wave envelopes, which can be viewed in time or space as a pair of symmetrical curves passing through wave crests and troughs, respectively. If the spectrum is strictly narrow-band, envelopes are smooth and slowly varying so that maxima and minima of the upper and lower envelopes exactly coincide with wave crests and troughs. At the other extreme, if the sea state is characterized with a wide-band spectrum, the wave profile and its envelopes vary rather rapidly, and local maxima and minima of the upper and lower envelopes do not necessarily correspond to wave crests and troughs [see, e.g., Ref. 11]. In either case, the difference between the upper and lower envelopes, or, equivalently, twice the local wave amplitude, represents a wave height which is Rayleigh-distributed.

Almost all empirical distributions derived from field data are based on a crest-to-trough representation which differs fundamentally from the envelope-based definition. In fact, a crest-to-trough wave height corresponds to the sum of two values of the upper envelope separated by approximately half the local period or wavelength, and represents an averaging operation on the envelope. Therefore, the objective here is to examine explicitly the distribution of wave heights based on this latter definition and to compare it with the Rayleigh law. Retaining the assumption concerning the linear Gaussian nature of the sea surface,

¹ Assoc. Prof., Civil Engrg. Dept., Kuwait Univ., P.O. Box 5969, Kuwait.

Note.—Discussion open until January 1, 1982. To extend the closing date one month, a written request must be filed with the Manager of Technical and Professional Publications, ASCE. Manuscript was submitted for review for possible publication on May 6, 1980. This paper is part of the *Journal of the Waterway, Port, Coastal and Ocean Division*, August, 1981. ISSN 0148-9895/81/0003-0149/\$01.00.

we aim to show that the density of crest-to-trough wave heights is fundamentally different from the Rayleigh form, showing an excess of waves with heights near the midrange and a deficiency of the two extremes in a manner increasing with larger values of the spectrum bandwidth.

DENSITY OF WAVE HEIGHTS BASED ON WAVE ENVELOPE

Let the elevation of the sea surface at a given point be represented by

$$\eta(t) = \sum_{n=1}^N c_n \cos(\omega_n t + \epsilon_n) \quad (1)$$

in which ω_n = frequencies distributed densely in the interval $(0, \infty)$; ω_n = uniform random phases over an interval of 2π ; and, c_n = amplitudes such that over any frequency interval, $(\omega_n, \omega_n + d\omega_n)$

$$\frac{1}{2} \sum c_n^2 = S(\omega) d\omega \quad (2)$$

with $S(\omega)$ representing the one-sided one-dimensional spectrum. The j th spectral moment is defined as

$$\mu_j = \int_0^\infty \omega^j S(\omega) d\omega \quad (3)$$

In particular, μ_0 = variance of η ; and $\omega_0 = \mu_1/\mu_0$ = mean frequency. The spectrum is considered to be narrow-band if (4,5)

$$\nu^2 = \frac{\mu_2}{\mu_0 \omega_0^2} - 1 \ll 1 \quad (4)$$

In general, $\eta(t)$ can be rewritten as

$$\eta(t) = A(t) \cos(\omega_0 t + \theta) \quad (5)$$

in which $A(t)$ and $\theta(t)$ = the amplitude and phase functions, respectively, defined by

$$A \exp(i\theta) = \sum_n c_n \exp\{i[(\omega_n t + \epsilon_n)]\} \exp(-i\omega_0 t) \quad (6)$$

$$\text{Thus } A(t) = (\eta^2 + \hat{\eta}^2)^{1/2} \quad (7)$$

$$\text{in which } \hat{\eta} = \sum_{n=1}^N c_n \sin(\omega_n t + \epsilon_n) \quad (8)$$

The free surfaces, η and $\hat{\eta}$, become asymptotically Gaussian and independent as the number of terms, N , of cosine functions approaches infinity. Under this limiting condition, the probability density of A is the Rayleigh law (10). In particular, the density corresponding to the scaled amplitude, $\xi = A/A_{\text{rms}} = A/(2\mu_0)^{1/2}$, has the invariant form

$$f_\xi(x) = 2x \exp(-x^2); \quad x \geq 0 \quad (9)$$

The joint density of $\xi_1 = \xi(t)$ and $\xi_2 = \xi(t + \tau)$ is [see, e.g., Ref. (7)]

$$f_{\xi_1 \xi_2}(x_1, x_2; \tau) = \frac{4x_1 x_2}{1-r^2} I_0 \left(\frac{2x_1 x_2 r}{1-r^2} \right) \exp \left(-\frac{x_1^2 + x_2^2}{1-r^2} \right); \quad x_1, x_2 \geq 0. \quad (10)$$

in which $I_0(\cdot)$ = zero-order modified Bessel function of the first kind; and

$$r(\tau) = (\rho^2 + \lambda^2)^{1/2} \quad (11)$$

$$\text{with } \rho(\tau) = \mu_0^{-1} \int_0^\infty S(\omega) \cos(\omega - \omega_0) \tau d\omega \quad (12)$$

$$\lambda(\tau) = -\mu_0^{-1} \int_0^\infty S(\omega) \sin(\omega - \omega_0) \tau d\omega \quad (13)$$

Strictly speaking, $A(t)$ and $-A(t)$ represent formal definitions for the upper and lower wave envelopes (9,11). The basic character of these is intimately related to the spectral bandwidth measure, ν . In particular, $\dot{A} = dA/dt$ is zero-mean Gaussian with variance, $\nu^2 \omega_0^2 \mu_0$, (3), i.e.

$$f_{\dot{A}}(x) = (2\pi \nu^2 \omega_0^2 \mu_0)^{-1/2} \exp \left(\frac{-x^2}{2\nu^2 \omega_0^2 \mu_0} \right); \quad -\infty < x < \infty \quad (14)$$

Thus, the narrow-band condition $\nu^2 \ll 1$ suggests that the underlying spectrum, $S(\omega)$, and $f_A(x)$ are centered sharply around $\omega = \omega_0$ and $x = 0$, respectively, and behave as pseudo-delta-functions. Correspondingly, each realization of η depicted by Eq. 5 has the distinctive form of slowly modulated oscillations with an apparent mean frequency, ω_0 . By the same token, η and $\hat{\eta}$ are nearly out of phase by $\pi/2$ so that when η is maximum, corresponding to a wave crest, $\hat{\eta} \approx 0$ and $A \approx \eta$. Similarly, when $\hat{\eta}$ is maximum, corresponding to a trough, $\eta \approx 0$ and $A \approx \hat{\eta}$. Hence, we have the upper and lower envelopes, A and $-A$, from a pair of symmetrical curves which pass through wave crests and troughs respectively, and vary very slowly in between as implied by Eq. 14.

When the spectrum is wide-band so that the condition $\nu^2 \ll 1$ is not satisfied strictly, Eq. 14 suggests that the rate of change of A could be rather large. In this case, realizations of η can no longer be viewed as amplitude-modulated oscillations with an apparent mean frequency, ω_0 . Consequently, the physical interpretation of A as an amplitude is somewhat lost. Nonetheless, the formalism provided through Eqs. 5 and 6 remains valid, and a local wave height can still be defined as $H = 2A$. Noting that $H_{rms} = 2A_{rms}$, it then follows that the scaled height $\xi = H/H_{rms}$ has the invariant probability density depicted by the Rayleigh form of Eq. 9, regardless of whether the condition $\nu^2 \ll 1$ is satisfied or not.

DENSITY OF CREST-TO-TROUGH WAVE HEIGHTS

The crest-to-trough wave height is defined as

$$\bar{H} = A_1 + A_2 \quad (15)$$

in which $A_1 = A(t)$ and $A_2 = A(t + T/2)$ represent, respectively, two values

of the wave envelope separated by half the local period corresponding to the time interval between a crest and one of the adjacent troughs. The scaled height follows as

$$\bar{\xi} = \frac{\bar{H}}{2(2\mu_0)^{1/2}} = \frac{\xi_1 + \xi_2}{2} \quad (16)$$

The conditional distribution of $\bar{\xi}$, given $\tau = T/2$, is defined by

$$F_{\bar{\xi}|\tau} \left(x \left| \frac{T}{2} \right. \right) = \Pr \left(\bar{\xi} \leq x, \text{ given } \tau = \frac{T}{2} \right) = \Pr \left(\xi_1 + \xi_2 \leq 2x, \text{ given } \tau = \frac{T}{2} \right) \quad (17)$$

Making use of Eq. 10 and paying appropriate attention to the region of integration implied in this definition, we can write it as

$$F_{\bar{\xi}|\tau} \left(x \left| \frac{T}{2} \right. \right) = \int_{x_2=0}^{2x} \int_{x_1=0}^{2x-x_2} f_{\xi_1\xi_2} \left(x_1, x_2; \frac{T}{2} \right) dx_1 dx_2 \quad (18)$$

The derivative of the preceding with respect to x yields the conditional density

$$f_{\bar{\xi}|\tau} \left(x \left| \frac{T}{2} \right. \right) = 2 \int_0^{2x} f_{\xi_1\xi_2} \left(2x - u, u; \frac{T}{2} \right) du \quad (19)$$

Finally, allowing the period T to take all possible values, we obtain the marginal probability density of $\bar{\xi}$:

$$f_{\bar{\xi}}(x) = 2 \int_{t=0}^{\infty} \int_{u=0}^{2x} f_T(t) f_{\xi_1\xi_2} \left(2x - u, u; \frac{t}{2} \right) du dt \quad (20)$$

in which $f_T(t)$ = the density of T , with $t \geq 0$.

Since the joint density $f_{\xi_1\xi_2}$ is closely related to the surface spectrum through Eqs. 10-13, the probability density of crest-to-trough heights is a functional of both the spectral shape, $S(\omega)$, and the density of wave periods, $f_T(t)$. This essential characteristic is a distinct contrast to the Rayleigh law. It also renders the explicit evaluation of $f_{\bar{\xi}}$ numerically a rather tedious attempt in general. Therefore, in order to proceed with this objective with reasonable ease, Eq. 20 is further simplified by appealing to the narrow-band approximation, requiring that $\nu^2 \ll 1$. Under this condition $S(\omega)$ behaves as a pseudo-delta-function centered around $\omega = \omega_0$, and the Taylor series expansions

$$\cos(\omega - \omega_0)\tau \approx 1 - \frac{1}{2}(\omega - \omega_0)^2\tau^2 \quad (21)$$

$$\sin(\omega - \omega_0)\tau \approx (\omega - \omega_0)\tau \quad (22)$$

can be used in Eqs. 12 and 13 to show that $\lambda(\tau) \approx 0$, and

$$r(\tau) \approx \rho(\tau) \approx 1 - \frac{1}{2}(\omega_0\tau\nu)^2 \quad (23)$$

Proceeding further, the corresponding density, $f_T(t)$, is sharply centered around the mean apparent period, $T_0 = 2\pi/\omega_0$. Therefore, it behaves as a pseudo-delta-function with respect to the integrand in Eq. 20, reducing it to

$$f_{\xi}(x) \approx 2 \int_0^{2x} f_{\xi_1 \xi_2} \left(2x - u, u; \frac{\pi}{\omega_0} \right) du \dots \dots \dots (24)$$

The overall quality of this approximation should be fairly satisfactory provided that the condition $v^2 \ll 1$ is valid strictly, e.g., $v \leq 0.1$. The decreasing accuracy

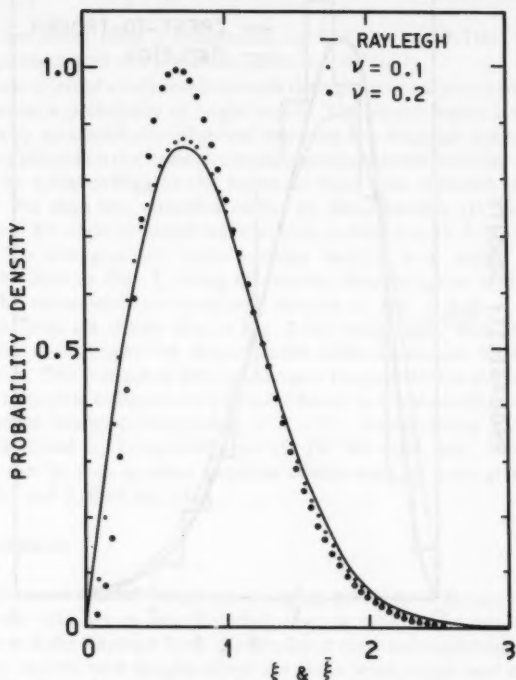


FIG. 1.—Comparison between Rayleigh Law and Density of Crest-to-Trough Wave Heights under Narrow-Band Conditions

as v becomes larger should still serve well enough to illustrate a qualitative picture of the basic behavior of f_{ξ} , which still has to be determined numerically but with far more ease and less information than that required by Eq. 20 in general.

Using Simpson's rule, Eqs. 10, 23, and 24, f_{ξ} was evaluated numerically for two illustrative cases as shown in Fig. 1, corresponding to $v = 0.1$, $r \approx 0.95$, and $v = 0.2$, $r \approx 0.80$, respectively. The Rayleigh density is shown also in the same figure for comparison. It is observed that the density of crest-to-trough

heights displays an excess of waves with heights near the midrange and a deficiency at the two extremes in a manner increasing with ν . As previously suggested in the Introduction, this is because the crest-to-trough height as defined by Eq. 16 represents an averaging or smoothing operation on the wave envelope, damping its oscillations about an average value. Thus, the resulting density must have the same mean, and show an excess about the mean and deficiencies away from it.

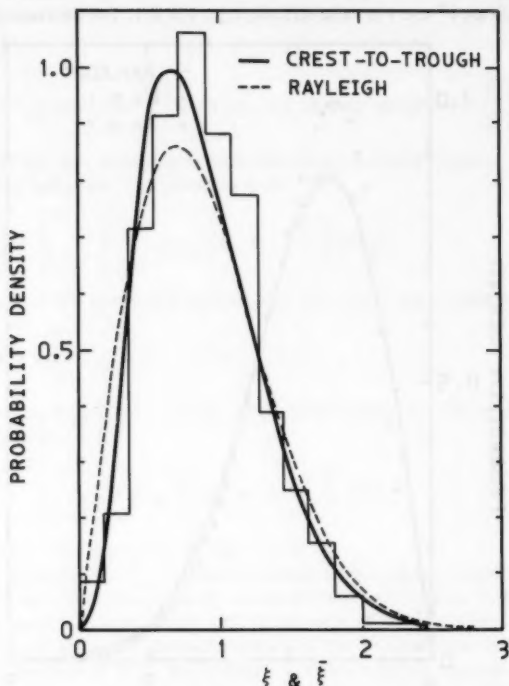


FIG. 2.—Histogram of Scaled Crest-to-Trough Wave Heights from Bretschneider (1) in Comparison with Rayleigh Law and Theoretical Density of Crest-to-Trough Wave Heights, $\nu = 0.2$

The theoretical mean and variance of $\bar{\xi}$ can be obtained exactly, by utilizing Eqs. 10, 16, and 20, as

$$E(\bar{\xi}) = E(\xi) = \frac{\sqrt{\pi}}{2} \dots \dots \dots (25)$$

$$\text{and } \sigma_{\bar{\xi}}^2 = \frac{1}{2} + \frac{\pi}{8} \int_0^\infty f_T(t) {}_2F_1\left(-\frac{1}{2}, -\frac{1}{2}; 1; r^2 \frac{t}{2}\right) dt - \frac{\pi}{4} \dots \dots (26)$$

in which ${}_2F_1(\cdot)$ = the hypergeometric function. The variance of ξ is

$$\sigma_\xi^2 = 1 - \frac{\pi}{4} \quad (27)$$

Since $r^2 < 1$ always (except when η is a monochromatic wave with a constant amplitude),

$${}_2F_1\left(-\frac{1}{2}, -\frac{1}{2}; 1; r^2\right) < \frac{4}{\pi} \quad (28)$$

Therefore, it follows from a comparison of Eqs. 26 and 27 that $\sigma_\xi^2 < \sigma_\xi^2$, which is consistent with the preceding analysis and Fig. 1.

The ultimate effect of a deficiency towards the high wave tail is an underestimate in the exceedance probability of larger waves. The partial reason for this kind of discrepancy systematically observed between the Rayleigh form and field data can be explained on this basis. A case of practical interest has been considered previously by Longuet-Higgins (5), based on field data collected in the Gulf of Mexico. The data was compiled earlier by Bretschneider (1) and contains approximately 400 crest-to-trough wave heights in records e-11-3-15 of the same reference. The histogram of crest-to-trough heights in a scaled form was reconstructed here in Fig. 2, using the scatter diagram given in Fig. 5.1 of Ref. (1). The theoretical crest-to-trough density of Fig. 1 with $\nu = 0.2$ and the Rayleigh form are shown also in Fig. 2 for comparison. It is evident that the histogram does display the discrepancies under discussion relative to the Rayleigh form. This was noted also by Longuet-Higgins (5). On the other hand, most of the histogram ordinates are predicted better by the theoretical zero-crossing wave-height density corresponding to $\nu = 0.2$, which closely approximates the 0.234 estimated by Longuet-Higgins (5) for the same data. Discrepancies of this sort can be seen in other empirical results such as those given in Figs. 4.21-23, 4.28, and 4.30 of Ref. (1).

CONCLUDING REMARKS

The definition of crest-to-trough wave heights differs from the envelope-based representation relevant to the Rayleigh law. It was demonstrated that, in comparison with the Rayleigh form, the density of crest-to-trough heights displays an excess of waves, with heights about the mean wave height and deficiencies at both ends away from the mean. A principal effect of a deficiency towards the high wave tail is an underestimate in the exceedance probability of larger waves associated with the greatest engineering concern. Considering that the representation of wave heights based on the wave envelope is consistent with the theoretical and physical specifications of narrow-band sea waves, there is no obvious justification for using a crest-to-trough definition. This plea is supported ultimately by the need to explain the differences observed between field data and the Rayleigh theory. The rationale is that, if future field data is also analyzed on the basis of an envelope definition, possible discrepancies arising from the crest-to-trough definition would be eliminated, and, thereby, effects of other physical mechanisms such as wave breaking could perhaps be isolated.

Most crest-to-trough data are derived from records of 15-min-20-min duration, usually providing 100-150 sample points for the construction of a histogram. In principle, a sample of this size is insufficient to estimate a stable, well-resolved distribution. Very often gaps exist in the data so that the analyst is forced to enlarge intervals. The histogram displayed in Fig. 2 would actually have no ordinates in several intervals if the mesh presently used for the abscissa were halved (see, Ref. 1, Fig. 5.1). For the same record, the envelope presents a continuous sample space with a much larger size. To be specific, a 20-min record sampled at a periodic interval of $\Delta = 0.5$ sec would yield 2,400 sample points, which would allow more flexibility in performing data analysis and obtaining histograms ordinates with varying degrees of statistical quality.

The construction of sample points from an envelope is simple, and can be carried out efficiently if coupled with FFT operations, routinely used in the spectral analysis of sea surface elevations. Consider, for instance, the finite record $\eta_0, \eta_1, \dots, \eta_{M-1}$, in which $\eta_t = \eta(t\Delta)$. The FFT coefficients are given by

$$Y_k = M^{-1} \sum_{t=0}^{M-1} \eta_t \exp \left(2\pi i k \frac{t}{M} \right) \dots \dots \dots (29)$$

in which $k = 0, 1, \dots, M-1$; and, $i = \sqrt{-1}$. Correspondingly

$$\eta_t = \sum_{k=0}^{M-1} Y_k \exp \left(-2\pi i k \frac{t}{M} \right) \dots \dots \dots (30)$$

or, since η_t is real

$$\eta_t = \frac{1}{2} \sum_{k=0}^{M-1} (Y_k + Y_k^*) \cos \left(2\pi k \frac{t}{M} \right) \dots \dots \dots (31)$$

in which $Y_k^* = \text{complex conjugate of } Y_k$. Now define

$$\hat{\eta}_t = \frac{1}{2} \sum_{k=0}^{M-1} (Y_k + Y_k^*) \sin \left(2\pi k \frac{t}{M} \right) \dots \dots \dots (32)$$

in analogy with Eq. 8. Therefore, the sample of wave heights needed for histogram analysis is given by

$$H_t = 2(\eta_t^2 + \hat{\eta}_t^2); \quad t = 0, 1, \dots, M-1 \dots \dots \dots (33)$$

Finally, crest-to-trough wave heights from different records are grouped together often to increase the sample size artificially. This would be a valid procedure indeed if all samples came from a common probability law. Such is the case for Rayleigh-distributed variables by virtue of the invariant form of this distribution if the variates are scaled with respect to their means or root-mean-square values. However, if samples are not from a common probability law, it is obvious that the histogram constructed on this basis cannot be entirely meaningful. Therefore, any other physical reason associated with a sea state put aside, the reliance on the sole usage of crest-to-trough wave heights inherently requires that samples from different records with varying spectral bandwidth measures not be grouped together since they do not obey the same probability law.

ACKNOWLEDGMENTS

Thanks are due to Daisy Mathew for the preparation of the manuscript. The writer is grateful also to the computer center staff of Kuwait University for their generous assistance in the computational aspects of this research.

APPENDIX I.—REFERENCES

1. Bretschneider, C. L., "Wave Variability and Wave Spectra for Wind-Generated Gravity Waves," *Technical Memorandum 118*, U.S. Beach Erosion Board, Washington, D.C., 1959.
2. Forristall, G., "On the Statistical Distribution of Wave Heights in a Storm," *Journal of Geophysical Research*, Vol. 83, No. C5, May, 1978, pp. 2353-2358.
3. Lin, Y. K., *Probabilistic Theory of Structural Dynamics*, McGraw-Hill Book Co., Inc., New York, N.Y., 1967, p. 316.
4. Longuet-Higgins, M. S., "On the Statistical Distribution of the Heights of Sea Waves," *Journal of Marine Research*, Vol. XI, No. 3, 1952, p. 245.
5. Longuet-Higgins, M. S., "On the Joint Distribution of the Periods and Amplitudes of Sea Waves," *Journal of Geophysical Research*, Vol. 80, No. 18, 1975, p. 2688.
6. Longuet-Higgins, M. S., "On the Distribution of Sea Waves: Some Effects of Nonlinearity and Finite Band Width," *Journal of Geophysical Research*, Vol. 85, No. C3, 1980, pp. 1519-1523.
7. Middleton, D., *An Introduction to Statistical Communication Theory*, McGraw-Hill Book Co., Inc., New York, N.Y., 1960, pp. 396-436.
8. Nolte, K. G. and Hsu, F. H., "Statistics of Larger Waves in a Sea State," *Journal of the Waterway, Port, Coastal and Ocean Division*, ASCE, Vol. 105, No. WW4, Proc. Paper 14963, Nov., 1979, pp. 389-404.
9. Tayfun, M. A., "Narrow-Band Non-linear Sea Waves," *Journal of Geophysical Research*, Vol. 85, No. C3, 1980, pp. 1548-1552.
10. Tayfun, M. A., "Breaking-Limited Wave Heights," *Journal of the Waterway, Port, Coastal and Ocean Division*, ASCE, Vol. 107, No. WW2, Proc. Paper 16255, May, 1981, pp. 59-69.
11. Yang, J.-N., "Simulation of Random Envelope Processes," *Journal of Sound and Vibration*, Vol. 21, No. 1, 1972, pp. 73-85.

APPENDIX II.—NOTATION

The following symbols are used in this paper:

- A = wave envelope or amplitude;
 A_1, A_2 = values of A separated by half wave period;
 c_n = Fourier coefficient of n th component wave;
 $E(\cdot)$ = expected value operator;
 $F_{\xi|\tau}$ = conditional density of ξ , given τ ;
 ${}_2F_1$ = hypergeometric function;
 f_T = probability density of wave period;
 $f_{\xi|\tau}$ = conditional density of ξ , given τ ;
 $f_\xi, f_{\bar{\xi}}$ = density of ξ and $\bar{\xi}$, respectively;
 H = wave height based on wave envelope;
 \bar{H} = crest-to-trough wave height;
 H_1, \bar{H}_1 = discrete values of H and \bar{H} , respectively;
 S = spectral density;
 T = wave period;

- t = time;
 u = integration variable, in Eqs. 19, 20, and 24;
 x_1, x_2 = integration variables, in Eq. 18;
 Y_k = complex FFT coefficient;
 Y_k^* = complex conjugate of Y_k ;
 Δ = sampling interval;
 ϵ_n = random phase associated with the n th component wavelet;
 $\eta, \hat{\eta}$ = sea surface elevations as a function of time;
 $\eta_i, \hat{\eta}_i$ = discrete values of η and $\hat{\eta}$, respectively;
 θ = random phase angle;
 λ = function defined by Eq. 13;
 μ_j = j th spectral moment;
 μ_0 = variance of η ;
 ν^2 = spectral bandwidth parameter defined by Eq. 4;
 ξ = $H/(2(2\mu_0)^{1/2})$ = nondimensional wave height based on wave envelope;
 $\bar{\xi}$ = $\bar{H}/(2(2\mu_0)^{1/2})$ = nondimensional crest-to-trough wave height;
 ξ_1, ξ_2 = values of ξ separated by half wave period;
 ρ = function defined by Eq. 12;
 $\sigma_\xi^2, \sigma_{\bar{\xi}}^2$ = variance of ξ and $\bar{\xi}$, respectively;
 τ = time lag or integration variable;
 ω = wave frequency, in radians; and
 ω_0 = apparent mean wave frequency.

EXTENDED VELOCITY POTENTIAL WAVE KINEMATICS

By Kostas F. Lambrakos¹

INTRODUCTION

Wave theories are an integral part of many design procedures for offshore and coastal structures. They are used with the design wave profile to predict flow quantities such as wave velocity, acceleration, and pressure from which design force calculations are made. Wave theories have also played a role in the determination of the empirical coefficients in relationships that translate wave velocity and acceleration to wave force, e.g., Morison's equation. In such applications, measurements of force are correlated with wave velocities and accelerations predicted by wave theories from measurements of wave profiles.

Several nonlinear wave theories (2,3,10) have worked the problem of symmetric harmonic waves (Stokes waves), and they have been used extensively by engineers to design offshore structures. These theories have also been used to calculate kinematics for measured waves on the basis of the zero-crossing wave height and period. The *stream function* procedure (3) can treat observed nonsymmetric (irregular) waves by achieving a best fit to the measured wave profile with a Stokes-type wave profile shifted in time (or space). The key assumption made in these procedures is that ocean or design waves propagate unaltered in form (shape). As a result, their domain of applicability includes only single waves of fixed wave-crest-to-wave-height ratios for a specified wave height, period, and water depth.

The procedure (EXVP) presented here allows for wave deformation (a characteristic feature of ocean waves) and its domain of applicability includes, in addition to Stokes waves, waves of various crest-to-height ratios and groups of waves. The ability to vary the crest-to-height ratio allows the design engineer greater flexibility in the choice of the design wave, whereas the ability to treat irregular waves may be used to improve the prediction of design wave forces through better correlations of measured waves and wave forces.

The EXVP procedure solves the wave velocity problem with a velocity potential function defined by a double Fourier series expansion in the frequency and wavelength domain. The procedure determines a velocity potential function that satisfies the governing equations in the body of water and at the bottom. Boundary

¹Sr. Research Specialist, Exxon Production Research Co., Houston, Tex. 77001.

Note.—Discussion open until January 1, 1982. To extend the closing date one month, a written request must be filed with the Manager of Technical and Professional Publications, ASCE. Manuscript was submitted for review for possible publication on October 15, 1980. This paper is part of the Journal of the Waterway, Port, Coastal and Ocean Division, Proceedings of the American Society of Civil Engineers, ©ASCE, Vol. 107, No. WW3, August, 1981. ISSN 0148-9895/81/0003-0159/\$01.00.

conditions at the wave surface are fitted numerically. The intrinsic assumption in the present form of the procedure is that waves are periodic in time and space—an assumption which is also made by all Stokes-type procedures.

This paper describes the theoretical and computational features of the procedure, presents examples of calculations for a Stokes wave and a cosine wave, and compares calculated and measured velocities from the Ocean Test Structure (OTS) experiment (1,4,6). The procedure has also been used to investigate the dependence of wave force on wave shape as reported at the 1974 Offshore Technology Conference (9). Additional theoretical analysis on EXVP and comparisons of EXVP with the Stokes wave solutions (2,3,10) are given in Ref. 8.

WAVE VELOCITY PROBLEM

Hydrodynamic Equations.—The water particle motion under waves at sea is defined on the basis of Fig. 1. The irregular wave profile extends indefinitely in the x direction, in water depth, d , over an impenetrable seafloor. With the

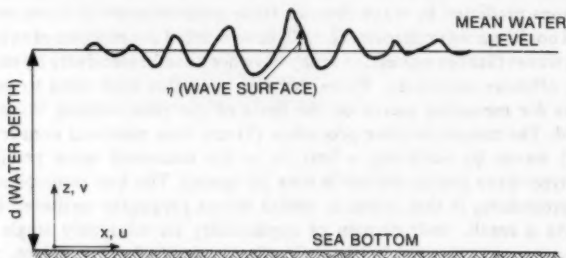


FIG. 1.—Definitions for Two-Dimensional Wave Flow Problem

assumptions of two dimensions, irrotational flow, and incompressible water, the equations of motion for the wave can be expressed in terms of the continuity and Bernoulli's equations (7):

$$\text{continuity: } \frac{\partial u}{\partial x} + \frac{\partial v}{\partial z} = 0 \quad \dots \dots \dots (1)$$

$$\text{Bernoulli: } z + \frac{p}{\rho g} + \frac{1}{2g} (u^2 + v^2) - \frac{1}{g} \frac{\partial \phi}{\partial t} = c \quad \dots \dots \dots (2)$$

in which x, z = the horizontal and vertical coordinates, respectively; p = the hydrodynamic pressure; ρ = the water density; g = the gravitational constant; and c = an undetermined constant. The horizontal and vertical components, u and v , of the water particle motion are related to the velocity potential function, ϕ , by its spatial derivatives as a consequence of the irrotational flow assumption:

$$u = -\frac{\partial \phi}{\partial x}; \quad v = -\frac{\partial \phi}{\partial z} \quad \dots \dots \dots (3)$$

The boundary conditions characteristic to this problem apply at the wave surface and at the sea floor over all space and time. There are two boundary conditions at the wave surface and one at the sea bottom:

1. The kinematic boundary condition assures that water particles do not escape from the wave surface and is expressed by

$$\frac{\partial \eta}{\partial t} + u \frac{\partial \eta}{\partial x} - v = 0 \quad (4)$$

in which η = the wave elevation (distance from mean water level). The velocities are evaluated at the wave surface.

2. The dynamic boundary condition is simply Bernoulli's equation evaluated at the wave surface:

$$\eta + \frac{p_s}{\rho g} + \frac{1}{2g} (u^2 + v^2) - \frac{1}{g} \frac{\partial \phi}{\partial t} = c \quad (5)$$

in which p_s = the atmospheric pressure.

3. The boundary condition at the sea floor requires that the vertical component of velocity be zero, i.e.

$$v = 0 \quad (6)$$

In view of Eq. 3, the solution to the wave velocity problem previously defined consists of finding a velocity potential which satisfies Eqs. 1 and 2 and boundary conditions, Eqs. 4, 5, and 6. There is difficulty in obtaining such a velocity potential since the boundary conditions at the wave surface are nonlinear. Consequently, it becomes virtually impossible to satisfy them exactly, especially when the wave profile is not known *a priori* over space and time, as is the case of ocean or design waves. Treating each wave individually and making the assumptions of wave periodicity and invariance in the wave shape, assumptions which the commonly known wave theories make, reduce the difficulty of the problem as previously stated since the boundary conditions need only be satisfied for one space point and over the period of the wave. Since profile deformation is a characteristic feature of almost all waves, the wave velocity procedure presented here attempts to satisfy the hydrodynamic equations and boundary conditions without the restriction of constancy in the wave profile.

Extended Velocity Potential (EXVP) Solution.—The velocity potential of the present approach is assumed to be given by a Fourier series expansion in the spatial coordinate, x :

$$\phi(x, z, t) = \sum_n \cosh(k_n z) [E_n(t) \cos(k_n x) + F_n(t) \sin(k_n x)] \quad (7)$$

in which E_n , F_n = functions of time; k_n = the wave number of the n th Fourier component; and E_n , F_n , and k_n are evaluated from the boundary conditions of the given wave problem. The aforementioned form for the velocity potential satisfies exactly the continuity equation and the boundary condition at the bottom. It is believed that this general expression could be used to obtain a numerical solution for the case where the wave profile is specified at more than one location.

If the functions E_n and F_n are defined appropriately, the velocity potential can be expressed in terms of progressive harmonics:

$$\phi(x, z, t) = \sum_{n,m}^{N,M} \cosh(k_n z) [A_{nm} \cos(k_n x - \omega_m t) + B_{nm} \sin(k_n x - \omega_m t)] \quad (8)$$

in which $k_n, \omega_m, A_{nm}, B_{nm} = \text{constants}$. This form of the potential function differs from previous definitions in a crucial way. For each frequency, ω_i , there is a corresponding set of wavelengths, $\{k_j\}$, and vice versa. Consequently, the harmonic wave components for a specific frequency value are allowed to propagate with different phase velocities defined by the ratio, ω_i/k_j . This feature of EXVP enables treatment of nondeforming (Stokes) as well as deforming wave shapes. The proposed method differs from other procedures that treat the nondeforming wave shapes based on one-to-one correspondence between frequency and wavelength, and on the same frequency-to-wavelength ratio (constant celerity) for all harmonics.

The constants, k_n, A_{nm}, B_{nm} , in the EXVP expansion, Eq. 8, are determined numerically by satisfying both boundary conditions, Eqs. 4 and 5, at the wave surface. Within the assumption of wave periodicity in space and time and with the specified pressure at the wave surface, the harmonic coefficients, A_{nm}, B_{nm} , that are dominant in the expansion depend on the wave profile. If the wave profile is of the Stokes shape, the dominant harmonic coefficients are only those with equal wave frequency-to-wave number ratios, and their values are the same with those for the Stokes-type solutions (10). If the wave profile differs from the Stokes shape, additional terms become important. In the case of a relatively small wave, the coefficients corresponding to Airy wave frequency-to-wave number ratios dominate.

The EXVP Computational Procedure.—The constants in EXVP are calculated by an iterative numerical procedure that minimizes the error in the kinematic and dynamic boundary conditions. The specified wave profile, which can be of more than one wave, is assumed periodic in time and space. Thus, the numerical fit to the boundary conditions is for an appropriate (and finite) number of points in space and time. Since the wave is deforming, matching to the boundary conditions is carried out over both distance and time; if the wave is nondeforming (same celerity for all Fourier components), the matching may be carried out over only distance or time.

Since the wave profile is normally specified at one space location, the error in the dynamic boundary condition (Bernoulli's equation) is computed for only that one location. For every other location the error is zero since Bernoulli's equation, Eq. 2, is used to calculate the wave profile for any location other than that for which the profile is known. At the end of the computation, a new wave profile may be calculated from Bernoulli's equation even for the location at which the profile was given; this wave profile should approximate well the initial profile and, along with the velocity potential coefficients, would satisfy Bernoulli's equation at the wave surface with arbitrary prescribed accuracy.

As was stated earlier, the EXVP calculation assumes that the specified wave profile is periodic in space and time. The fundamental period in time is normally equal to the time span, T_1 , of the specified wave profile. The frequencies,

$\{\omega_i\}$, for the Fourier series expansion are defined by

$$\omega_i = i\omega_1 \dots \dots \dots (9)$$

in which $\omega_1 = 2\pi/T_1$. The unknown fundamental period, L_1 , in space is calculated by the error minimization procedure; the corresponding wave number is $k_1 = 2\pi/L_1$, and the remaining wave numbers are defined by

$$k_i = ik_1 \dots \dots \dots (10)$$

The unknown coefficients, $\{A_{nm}\}$, $\{B_{nm}\}$, in the EXVP expansion are matrices each element of which corresponds to specific values of frequency and wave number, i.e.

$$\{A_{nm}\}_{N,M} = \begin{bmatrix} A_{11} & A_{12} & \dots & A_{1M} \\ A_{21} & A_{22} & \dots & A_{2M} \\ \vdots & \vdots & & \\ A_{N1} & A_{N2} & \dots & A_{NM} \end{bmatrix} \dots \dots \dots (11)$$

in which the rows correspond to the variation in the frequency, subscript m , and the columns to the variation in the wave number, subscript n , and each frequency and wave number is given by Eqs. 9 and 10. The diagonal elements correspond to the same celerity value, and they are the dominant elements in cases of nondeforming waves. Even for deforming profiles, not all elements in the coefficient matrices need be evaluated for a satisfactory fit to the boundary conditions, and the judicious choice of elements can save in computer time. The constant, c , in Bernoulli's equation, Eq. 2, is also considered an unknown.

The numerical procedure calculates the values of the unknowns in the EXVP expansion that minimize the error in the boundary conditions in a least-squares sense. With given values for the unknowns, errors in the kinematic boundary condition are calculated for every point in space, x_j , and time, t_i ; for the dynamic boundary condition only errors over time are calculated for the point in space for which the wave profile has been specified. The points may be given at equal increments, i.e., $x_j = (j-1)\Delta x$ and $t_i = (i-1)\Delta t$, in which the increments Δx and $\Delta t \leq$ half the shortest wave length and wave period expected in the wave, respectively.

The errors in the boundary conditions are calculated as follows. For the kinematic boundary condition

$$(E_k)_y = \frac{\partial \eta}{\partial t} + u \frac{\partial \eta}{\partial x} - v \dots \dots \dots (12)$$

For the dynamic boundary condition

$$(E_D)_y = \eta - \frac{1}{g} \frac{\partial \phi}{\partial t} + \frac{1}{2g} (u^2 + v^2) - c \dots \dots \dots (13)$$

in which the right-hand sides of Eqs. 12 and 13 are evaluated at the wave surface for time, t_i , and location, x_j . The least-squares sum of these errors is given by

$$Q = \sum_{i,j} [(E_D)_{ip}^2 + (E_K)_{ij}^2] \quad \dots \dots \dots (14)$$

This is the quantity which is minimized to obtain the optimum values for the coefficients; the subscript, p , designates the spatial location for which the wave profile is given. The minimization is achieved with a variant of the Gauss-Newton technique (5), which iterates on the first estimates of $\{A_{nm}\}$, $\{B_{nm}\}$, c , and $\{k_n\}$. A measure of quality of fit to the boundary conditions is obtained by dividing (weighting) the errors $\sum_i (E_D)_{ip}^2$ and $\sum_i (E_K)_{ij}^2$ by the root-mean-square values of the wave profile and its time derivative, respectively.

The first estimates of the coefficients are arbitrary but judiciously picked, as will be demonstrated in the examples given as follows. Some of them may be arrived at on the basis of linear (Airy) wave theory. Depending on how close the first estimates are to a good solution, the computer time required for the calculation can vary substantially.

If instead of the wave profile, the wave height and period of the wave are specified (for a given water depth), a variation of EXVP (EXVPD) can be used to calculate the wave shape. This case is the most common in the design of offshore structures, and has been treated with the Stokes procedures. For the EXVPD solution it is required that only the diagonal terms in the coefficient matrices be retained and that a constraint condition in the wave height be included as part of the least-squares minimization procedure. The initial estimate of the wave shape can be simple harmonic or a wave shape derived from linear or Stokes theory. In the end, EXVPD provides a wave that propagates without deformation and has the specified wave height.

The time requirements for executing EXVP in the IBM 168 computer may vary from several seconds, for the nondeforming waves, to several minutes for a wave segment of two irregular waves. In the final analysis, the time required in each case depends on the number of coefficients used, on how compatible these coefficients are with the given wave profile, and on the number of points in space and time required for fitting the boundary conditions. With present computer capabilities and EXVP's current numerical procedure, the computer time requirements for long irregular wave profiles (more than three waves) are nearly prohibitive.

EXVP WAVE ANALYSIS

For the purpose of illustrating some of the features of the EXVP solution and how it compares with field measurements of waves and velocities as well as with the Stokes type procedures, the EXVP procedure has been applied to two simple wave profiles and several irregular ocean wave profiles from the Ocean Test Structure measurements. The two simple wave profiles were of identical wave height, 40 ft (12 m), and wave period (12 sec), and the water depth was 100 ft (30 m). One was a cosine function of time and the other was a Stokes type wave profile. The irregular wave profiles were composed of two adjacent waves, one with a dominant crest; their crests and troughs are given in Table 3. The water depth was 66 ft (20 m).

Cosine Wave Profile.—The initial and final estimates of the EXVP coefficients for the cosine wave are given in Table 1. The improvement in the initial estimates

is clearly substantial, and this suggests that for a good solution the first guess does not need to be very close to the final solution. It is also evident from the final estimates that there is significant interaction between the various wave components since the off-diagonal terms are not negligible. The interaction manifests itself in the deformation of the wave profile and also in the wave velocities (8). During propagation the cosine wave deforms to wave forms of significantly higher crest-to-height ratios than the ratio of the Stokes wave of the same height and period. The near-surface water particle velocities reflect these differences in the wave crest—the velocities for the steeper waves are higher than the velocities for the Stokes wave.

Stokes Wave Profile.—The EXVP solution converges to the Stokes velocity potential solution for waves having the same profile as Stokes waves. The

TABLE 1.—EXVP Matrix Coefficients for Cosine Wave

INITIAL ESTIMATES				FINAL ESTIMATES			
(1)	(2)	(3)	(4)	(5)	(6)	(7)	(8)
(a) Matrix (A)							
-10.00	0.0	0.0	0.0	0.55	0.0	0.0	0.0
5.00	5.00	0.0	0.0	-4.03	1.72	0.0	0.0
-3.00	-3.00	-3.00	0.0	-0.02	-4.15	-0.87	0.0
-3.00	-3.00	-3.00	-3.00	1.67	-0.28	1.02	-0.08
0.0	-3.00	-3.00	-3.00	0.0	2.21	0.14	-0.13
0.0	0.0	2.00	2.00	0.0	0.0	0.90	0.24
0.0	0.0	0.0	2.00	0.0	0.0	0.0	0.09
(b) Matrix (B)							
-10.00	0.0	0.0	0.0	854.00	0.0	0.0	0.0
5.00	5.00	0.0	0.0	94.67	-100.90	0.0	0.0
-3.00	-3.00	-3.00	0.0	9.02	92.80	6.23	0.0
-3.00	-3.00	-3.00	-3.00	10.84	14.53	-22.18	0.74
0.0	-3.00	-3.00	-3.00	0.0	20.98	7.29	2.43
0.0	0.0	2.00	2.00	0.0	0.0	10.21	-3.60
0.0	0.0	0.0	2.00	0.0	0.0	0.0	-2.54

Stokes wave profile calculated with EXVPD for a wave height, period, and water depth of 40 ft (12 m), 12 sec, and 100 ft (30 m), respectively, was used with EXVP, and the results are shown in Table 2. The final EXVP coefficient matrices in Table 2 are dominated by the diagonal terms in the {B} matrix, which are very close to the velocity potential coefficients of the Stokes solution.

Irregular Wave Profiles.—The EXVP treatment of irregular waves from the ocean test structure experiment is very similar to the treatment of single waves. The OTS measured simultaneously storm wave profiles and water particle velocities at four elevations in the water column and, consequently, provides a unique opportunity for testing the velocity predictions from EXVP. Although the OTS data include a great number of waves, only 10 selected irregular waves were used for this study. These waves, however, are sufficient to demonstrate some of the EXVP capabilities for sea waves and to compare these capabilities

with those of the Stokes wave procedures.

The wave profiles in this study were composed of two adjacent waves, whose troughs, crests, and time span are given in Table 3. No particular criteria were used to choose these waves other than that the waves be large and cover a range of wave heights and periods. However, some bias toward two-dimensional

TABLE 2.—EXVP Matrix Coefficients for Stokes Wave

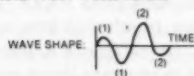
INITIAL ESTIMATES				FINAL ESTIMATES			
(1)	(2)	(3)	(4)	(5)	(6)	(7)	(8)
(a) Matrix (A)							
-10.00	0.0	0.0	0.0	-3.72	0.0	0.0	0.0
5.00	5.00	0.0	0.0	2.61	1.49	0.0	0.0
-3.00	-3.00	-3.00	0.0	-0.40	3.08	-0.16	0.0
-3.00	-3.00	-3.00	-3.00	-1.65	-0.00	-0.63	-0.12
0.0	-3.00	-3.00	-3.00	0.0	-4.21	0.23	0.16
0.0	0.0	2.00	2.00	0.0	0.0	-1.76	0.09
0.0	0.0	0.0	2.00	0.0	0.0	0.0	0.97
(b) Matrix (B)							
-10.00	0.0	0.0	0.0	883.20	0.0	0.0	0.0
5.00	5.00	0.0	0.0	4.47	-122.50	0.0	0.0
-3.00	-3.00	-3.00	0.0	-0.01	4.30	8.75	0.0
-3.00	-3.00	-3.00	-3.00	1.97	-1.61	-0.84	0.22
0.0	-3.00	-3.00	-3.00	0.0	3.83	-0.85	-0.21
0.0	0.0	2.00	2.00	0.0	0.0	1.33	-0.85
0.0	0.0	0.0	2.00	0.0	0.0	0.0	-0.92

Note: Stokes velocity potential coefficients: 877.50, -122.30, 8.84.

TABLE 3.—Irregular Ocean Test Structure Waves

WAVE NO. (1)	WAVE CREST 2 (IN FEET) (2)	WAVE TROUGH 1 (IN FEET) (3)	WAVE TROUGH 2 (IN FEET) (4)	WAVE CREST 1 (IN FEET) (5)	WAVE PERIOD (IN SEC) (6)
1	8.28	6.28	5.83	3.60	16.4
2	8.63	7.63	6.76	9.34	18.6
3	9.06	6.81	6.31	7.23	21.2
4	7.03	6.62	5.44	2.64	11.7
5	9.02	6.13	5.16	4.61	13.7
6	7.91	5.55	6.33	2.42	11.5
7	8.44	7.08	4.93	3.62	15.1
8	9.32	8.43	5.27	6.36	13.9
9	10.03	6.36	6.72	5.29	18.5
10	8.30	6.66	4.08	5.45	17.8

NOTE: 1 FOOT = 0.305 METERS



flow may be present since the troughs and adjacent crests are comparable to the wave crest of interest. The study focused on the velocities due to the larger of the two zero-crossing waves in the wave profile and compared the extreme (crest and trough) values of the measured velocity magnitudes for the crest and preceding and following troughs with the corresponding peak values predicted from the EXVP and Stokes (EXVPD) procedures. For one of the waves, no. 10, the study also compared the entire time record of the wave profile and the velocity magnitude for every elevation. Although the velocity direction changed within each wave record, no attempt was made to take direction

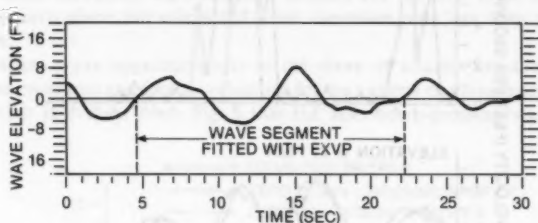


FIG. 2.—Ocean Test Structure Measured Wave Trace (Wave No. 10)

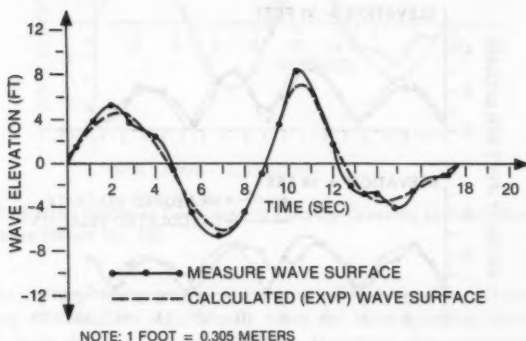
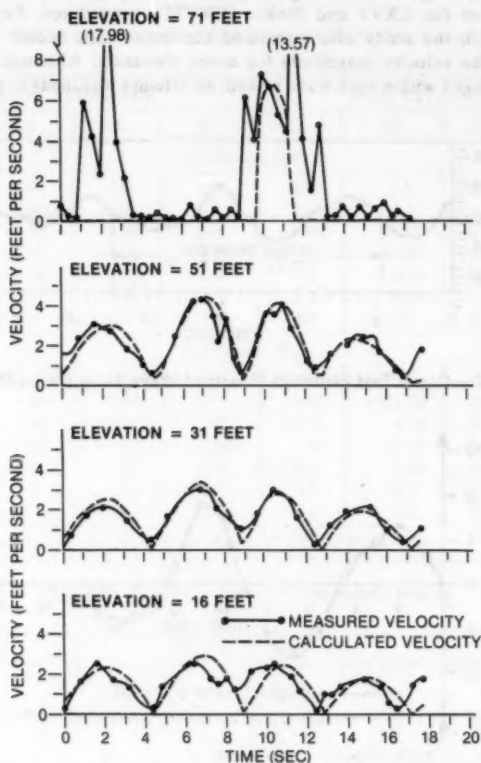


FIG. 3.—EXVP Wave Profile Fit to OTS-Measured Profile (Wave No. 10)

into account since the extreme velocities, which are of special interest, were nearly collinear. The velocities, however, were adjusted for the component of steady current (hourly velocity averages) which was present in the data. Also, the extreme velocities chosen for comparison were those that occurred within ± 0.5 sec from the instant of the maximum (crest) or the minimum (trough) profile value.

While in the EXVP analysis the fit to the wave profile was carried out in terms of the actual wave trace, the EXVPD analysis was performed on the basis of the zero up-crossing and zero down-crossing wave heights and periods,

which are the common approaches of approximating waves at sea with Stokes-type waves. The coefficient matrix members used in EXVP were identical to those used for the simple wave calculations above; it was assumed that the four frequencies would be sufficient to describe the wave velocities.



NOTE: 1 FOOT PER SECOND = 0.305 METERS PER SECOND

FIG. 4.—EXVP Wave Velocity Magnitude as Compared to OTS-Measured Velocity for Various Elevations (Wave No. 10)

The comparison of the EXVP solution with the entire measured wave and velocity traces has been carried out with wave profile no. 10, which has substantially different troughs, 6.66 ft (2.03 m) and 4.08 ft (1.24 m). The 30-sec wave trace from which wave profile 10 was chosen is shown on Fig. 2. Fig. 3 shows the two-wave segment of this trace that was used in EXVP and the profile that represents the EXVP fit to this segment. The EXVP profile closely fits the measured profile; the largest differences are in the crests and troughs

due to the lack of higher harmonics in the velocity potential. These differences, however, do not strongly affect the velocities since the measured and calculated velocity profiles for all lower three elevations are in very close agreement, as shown in Fig. 4. For the lowest elevation, a small phase shift between measurements and calculations for the crest velocities is present, but its origin has not been determined. For the elevation above the mean water level the measured velocities are not very reliable, due to poor current meter response as the sharp spikes and "ringing" in the data indicate. However, for this elevation the velocity predicted is in generally good agreement with the measured velocity. For the same elevation, the calculated velocity for the first crest in the wave profile is zero since the calculated crest elevation was less than the highest elevation.

The Stokes wave approximations to the wave of interest are shown in Fig. 5, and the measured and Stokes velocities for the various elevations are compared in Fig. 6. It is evident from Fig. 5 that the zero down-crossing wave matches

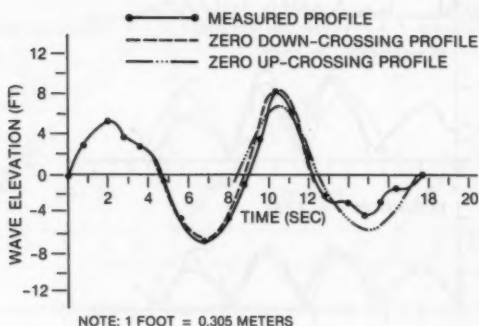
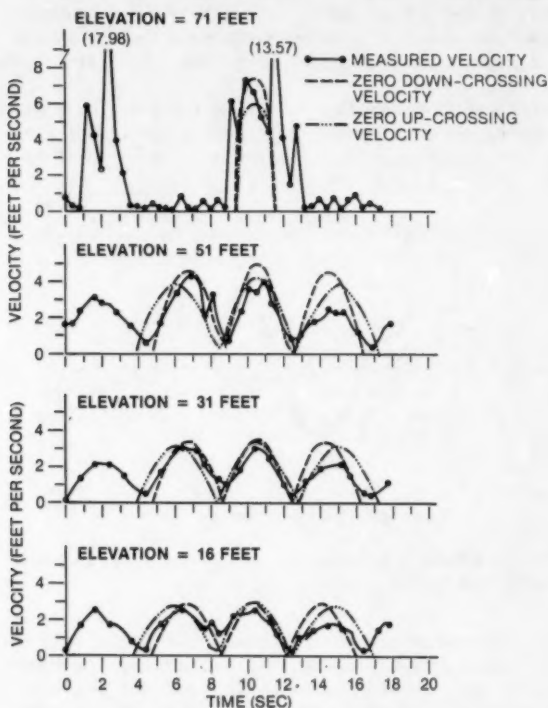


FIG. 5.—OTS Wave Profile as Compared to Zero Up-Crossing and Zero Down-Crossing Stokes Waves (Wave No. 10)

closely the corresponding part of the measured wave profile, whereas the zero up-crossing wave differs significantly from the corresponding measured wave profile in both the crest and the trough. However, the calculated velocities for the two Stokes waves show the opposite trends, i.e., the up-crossing velocities are closer to the data than the down-crossing velocities. The calculated velocities for the highest elevation, Fig. 6, are comparable to the measurements, but, owing to the uncertain quality of the measurements, no definitive comparisons can be drawn. The calculated velocities at the 51-ft (15.6-m) elevation from both Stokes waves are, overall, larger than the data, for the crest and following trough, by as much as 25% and 70%, respectively. For the lower elevations, the calculated velocities compare better with the data, the up-crossing velocities being smaller than the down-crossing velocities, and closer to the data.

From the aforementioned comparisons, several observations can be made. The crest and trough values for the zero down-crossing wave are larger than those for the zero up-crossing wave, and the same is true for the velocities.

As noted previously, the up-crossing velocities are in better agreement with the data for these particular wave profiles, but, for other irregular wave profiles for which the down-crossing wave is smaller than the up-crossing wave, it is conceivable that the down-crossing velocities will be closer to the data. The differences between the velocity measurements and the Stokes velocities are greatest for the following trough for which the differences between calculated and measured trough elevations are largest. Also, it would appear that if the



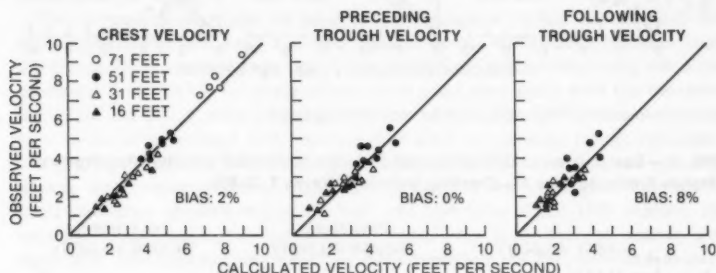
NOTE: 1 FOOT PER SECOND = 0.305 METERS PER SECOND

FIG. 6.—Stokes Wave Velocity Magnitude as Compared to OTS-Measured Velocity for Various Elevations (Wave No. 10)

Stokes wave would match both the crest and trough elevations of the measured wave profile, the Stokes velocities would, in general, be larger than the measured velocities. These observations suggest that the accurate prediction of velocities for irregular waves using Stokes representations is not a straightforward exercise; even if the "right" height is chosen for the crest velocity, the trough velocities will probably not be predicted adequately.

From the results of the EXVP and Stokes procedures, it becomes evident that the EXVP solution matches the data closer than the Stokes solution. This is true for the extreme crest and trough values as well as the rest of the wave and velocity profiles. The accuracy of the velocity prediction before and after the wave crest can have a twofold impact on the force calculation since the maximum force, e.g., for a vertical pile, normally occurs away from the wave crest, and, thus, both the flow velocity and resulting acceleration contribute to the force. It should also be noted that the Stokes procedure fails to predict higher velocities under the preceding wave trough than under the wave crest, as is observed in the data and predicted by EXVP.

The measured extreme velocities for the 10 waves studied have been differentiated on the basis of the crest, preceding trough, and following trough values and in terms of the four elevations in the water column. These data have been compared with the corresponding data from the EXVP and Stokes representations (Figs. 7-9). From the 10 waves only nine waves were used in these figures



NOTE: 1 FOOT PER SECOND = 0.305 METERS PER SECOND

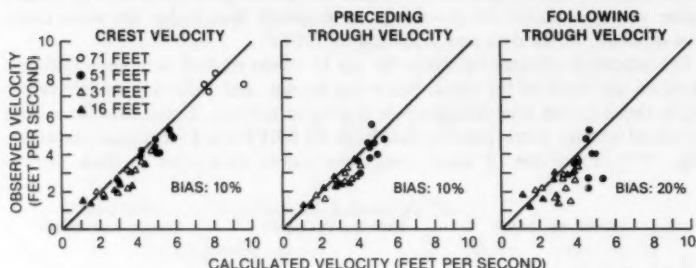
FIG. 7.—Comparison of OTS-Measured Extreme Horizontal Velocity Magnitude with EXVP-Predicted Velocity (Waves 1, 3-10)

since the extreme velocity values of wave no. 2 were outside the time band ± 0.5 sec about the corresponding extreme values of the wave profile. The measured values for the highest elevation that were used in the comparisons were only those that were subjectively judged of good quality.

Overall, the EXVP velocities, Fig. 7, are in better agreement with the measurements than the Stokes velocities, Figs. 8, 9; this is especially so under the wave troughs. The EXVP correlations show no significant differences in terms of elevation; the crest velocities show minimal bias (on the high side) and about 10% scatter; the velocities for the preceding trough also show minimal bias, if any, but more scatter, about 20%; the velocities for the following trough show a small bias, on the low side, and greater scatter than the velocities for the preceding trough. Part of the scatter present is probably due to wave spreading. However, the differences between the crest and trough velocity correlations are consistent with the differences between the measured and calculated extreme crest and trough elevation values—the percent differences for the troughs are greater than those for the crests. It is believed that if the

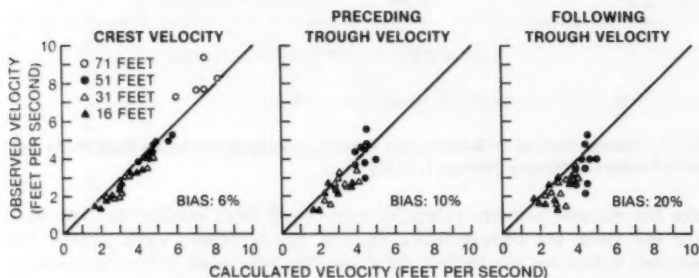
matching of the trough elevations were to be improved and a greater segment of the measured profile were taken into account, the scatter in the trough velocity correlations would be reduced even further.

As with the EXVP correlations of the extreme velocities, the correlations for the Stokes velocities, Figs. 8, 9, are better for the crests than for the troughs of the waves considered. For the zero up-crossing waves, the crest velocities for the elevation above the mean water level are biased on the low side and



NOTE: 1 FOOT PER SECOND = 0.305 METERS PER SECOND

FIG. 8.—Comparison of OTS-Measured Extreme Horizontal Velocity Magnitude with Stokes-Predicted Zero Up-Crossing Velocity (Waves 1, 3–10)



NOTE: 1 FOOT PER SECOND = 0.305 METERS PER SECOND

FIG. 9.—Comparison of OTS-Measured Extreme Horizontal Velocity Magnitude with Stokes-Predicted Zero Down-Crossing Velocity (Waves 1, 3–10)

for the remaining elevations, on the high side; the net bias is minimal, but the scatter is about 20%. The trough velocities show significant bias and considerable scatter—as much as 40% for the following trough. The same general observations can be made for the zero down-crossing waves; however, for these waves (as compared to the zero up-crossing waves) the bias and scatter are slightly larger for the crests, but smaller for the preceding troughs.

Although the Stokes-wave up-crossing representation gives different crest

velocities than the down-crossing representation, it is believed, as was noted earlier, that this is only true for the particular waves studied here for which the preceding trough is larger than the following trough. For waves where the following trough is larger than the preceding trough, the up-crossing correlation for the crest should be comparable to the down-crossing correlation here. Therefore, for a large group of waves, the up-crossing and down-crossing correlations will not be distinctly different, and the scatter for each Stokes representation will be comparable to the combined scatter shown here for both representations.

CONCLUSIONS

The EXVP procedure for calculating wave velocities can treat with accuracy single symmetric waves of relatively arbitrary crest-to-height ratios for a given wave height, period, and water depth, including Stokes-type waves of fixed crest-to-height ratios.

This procedure may also be used to treat irregular waves. Its accuracy for such applications has been checked against ocean wave measurements from the Ocean Test Structure experiment. Wave profiles and corresponding velocities predicted from EXVP for these waves show good agreement with the measurements for the entire wave period and water column. The EXVP crest velocities were in closer agreement with the data than were the extreme trough velocities.

The EXVP predictions matched the data significantly better than the common Stokes wave representations, especially under the wave troughs. The EXVP crest velocities showed negligible bias and less than about 10% scatter; the extreme trough velocities exhibited no significant bias, but the scatter was 20%–30%. The Stokes crest velocities were biased on the high side and showed a 20% scatter, and the extreme trough velocities had considerable bias (also on the high side) and more than 50% scatter.

Finally, this study has demonstrated that, in general, improved accuracy in predictions of velocities for irregular ocean waves is obtained if the theoretical formalism used accounts for a greater portion of the wave profile than the single wave of interest. It has also shown that the EXVP procedure has the capability to account for more than one wave with acceptable accuracy. In contrast, the common Stokes wave formalism can at best match only a single wave.

ACKNOWLEDGMENTS

The writer is indebted to J. C. Heideman for his help with the analysis of the Ocean Test Structure data.

APPENDIX I.—REFERENCES

1. Beckmann, H., and Merwin, J. E., "Wave Forces on Conductor Pipe Group," ASCE Specialty Conference, San Francisco, Calif., Civil Engineering in the Oceans IV, Vol. II, Sept., 1979.
2. Chappellear, J. E., "Direct Numerical Calculation of Wave Properties," *Journal of Geophysical Research*, Vol. 66, No. 2, Feb., 1961.
3. Dean, R. G., "Stream Function Representation of Nonlinear Ocean Waves," *Journal*

- of *Geophysical Research*, Vol. 70, No. 18, Sept., 1965.
4. Dean, R. G., Lo, J. M., and Johansson, P. I., "Rare Wave Kinematics Versus Design Practice," ASCE Specialty Conference, San Francisco, Calif., Civil Engineering in the Oceans IV, Vol. II, Sept., 1979.
 5. Farris, R. H., and Law, V. J., "Transformational Discrimination for Unconstrained Optimization," *IEC Fundamentals*, Vol. 11, 1972, pp. 154-161.
 6. Haring, R. E., and Spencer, L. P., "The Ocean Test Structure Data Base," ASCE Specialty Conference, San Francisco, Calif., Civil Engineering in the Oceans IV, Vol. II, Sept., 1979.
 7. Ippen, A. T., ed., *Estuary and Coastline Hydrodynamics*, McGraw-Hill Book Co., Inc., New York, N.Y., 1966.
 8. Lambrakos, K. F., "The Extended Velocity Potential Versus Stokes Wave Representation," *The Journal of Geophysical Research*, to be published.
 9. Lambrakos, K. F., and Brannon, H. R., "Wave Force Calculations for Stokes and Non-Stokes Waves," *OTC 2039*, Sixth Annual Offshore Technology Conference, Houston, Tex., May 6-8, 1974.
 10. Skjelbreia, L., and Hendrickson, J. A., "Fifth Order Gravity Wave Theory," *Proceedings*, Seventh Conference on Coastal Engineering, Chapt. 10, 1961, pp. 184-196.

APPENDIX II.—NOTATION

The following symbols are used in this paper:

- A_{nm} = matrix coefficient in Fourier expansion of velocity potential;
 B_{nm} = matrix coefficient in Fourier expansion of velocity potential;
 d = distance from bottom to mean water level;
 E_n = Fourier coefficient of velocity potential expansion in space;
 E_D = error in dynamic boundary condition;
 E_K = error in kinematic boundary condition;
 EXVP = extended velocity potential;
 EXVPD = Stokes' wave reduction of EXVP;
 F_n = Fourier coefficient of velocity potential expansion in space;
 g = acceleration of gravity;
 k_n = wave numbers for harmonic waves;
 L_n = wavelengths for harmonic waves;
 p = hydrodynamic pressure;
 Q = least-squares sum of errors in boundary conditions;
 t = time;
 T_n = wave periods of harmonic waves;
 u = horizontal component of water particle velocity;
 v = vertical component of water particle velocity;
 x = horizontal distance;
 z = vertical distance;
 η = wave surface elevation measured from mean water level;
 ρ = water density;
 ϕ = velocity potential function; and
 ω_n = angular wave frequency.

Subscripts

- s = wave surface;
 D = dynamic;
 K = kinematic; and
 p = spatial location.

OSCILLATORY ROUGH TURBULENT BOUNDARY LAYERS

By Iver Brevik¹

INTRODUCTION

The possibility of giving a mathematically simple and fairly accurate description of the oscillatory rough turbulent boundary layer deserves considerable interest, in view of the practical importance of this physical phenomenon. Under natural conditions, the bed boundary layer below sea waves is often rough turbulent, and reliable knowledge about the varying fluid velocity near the bed and the associated bed shear stress is of primary importance when estimating, for instance, the magnitude of sediment transport. In the laboratory, a rough turbulent boundary layer may conveniently be produced in water tunnel experiments above a rough bed.

Considerable work has so far been made to delineate the essential features of this kind of boundary layer. On the experimental side, the oscillating water tunnel experiments of Jonsson (6) and Jonsson and Carlsen (8) play a prominent role, and the theory of the present paper will later be compared with the observations in their Test No. 1, which was the most accurate of their two series. Other experimental investigations, using different experimental methods, have been carried out by Kalkanis (10) and Horikawa and Watanabe (5).

On the theoretical side, the most detailed mathematical treatment of the rough boundary layer is probably the one of Kajiura (9). The tenor of his treatment is to divide the whole boundary layer into three sublayers: an inner, an overlap, and an outer layer, each layer with its characteristic mean turbulent viscosity. It should be borne in mind that Kajiura's theory is a mean field theory in the sense that the turbulent viscosity $\nu_t = \nu_t(z)$ is taken as a function of the height z above the (theoretical) bed only; the time variation of ν_t has been ignored. Of course the omission of the time dependence of ν_t is an approximation for which the validity can only be checked a posteriori by comparing with accurate observations. Also, it should be noted that Kajiura's theory deals with the general case where the relative excursion amplitude near the bed is great enough to produce an overlap layer; for smaller excursion amplitudes the overlap layer vanishes (Eq. 2).

Now Kajiura's theory with its separation of the whole boundary layer into

¹Lect., Div. of Port and Ocean Engrg., The Univ. of Trondheim, Trondheim, Norway.

Note.—Discussion open until January 1, 1982. To extend the closing date one month, a written request must be filed with the Manager of Technical and Professional Publications, ASCE. Manuscript was submitted for review for possible publication on June 10, 1980. This paper is part of the Journal of the Waterway, Port, Coastal and Ocean Division, Proceedings of the American Society of Civil Engineers, ©ASCE, Vol. 107, No. WW3, August, 1981. ISSN 0148-9895/81/0003-0175/\$01.00.

three sublayers is formally complicated in that it requires matching of the analytic solutions of the basic differential equation at the two boundaries between the inner-overlap and the overlap-outer layers. Although the agreement between this theory and the Danish measurements indicates that the physical basis for the theory is sound, one may wonder if the theory is not, after all, unduly complicated. The present paper addresses itself to the following question: is it possible to reduce the mathematical complexity of Kajiura's theory and yet maintain reasonable good agreement with the observations? Specifically, the consequences of assuming a two-layer (instead of a three-layer) model will be worked out. The change involves omitting the inner part of the boundary layer from the description. The advantage one obtains from this performance is that no matching procedure is to be carried out at the lower end of the overlap layer. The price that has to be paid for this simplification is that the analytic solution for the fluid velocity, in contrast to Kajiura's solution, has to be terminated at a fixed level $z = z_0$ above the bottom. Such a situation is in fact well known from the theory of rough turbulent unidirectional flow with a logarithmic velocity profile, the expression for the fluid velocity has no meaning below the level at which it becomes equal to zero. Moreover, it seems to be rather common among more recent workers in the field to choose a way of approach where the analytic solution is terminated some distance above the bed (2,3,4).

The answer to the above question is affirmative. It is possible to reduce the model to a two-layer model and still obtain reasonable results. The opportunity will be taken to discuss the position of the upper limit of the overlap layer.

Finally, the reader is referred to the recent general treatment of Jonsson on rough turbulent boundary layers (7). This extensive work focuses attention on the existence of universal laws, i.e., the "law of the wall" and the "defect law for fluid velocity," which seem to hold in boundary layers of this kind. Moreover, this work contains a survey over earlier developments in the field.

BASIC ASSUMPTIONS AND EQUATIONS

The present theory is assumed to hold in the region $z \geq z_0$, where $z = 0$ defines the theoretical bed level. If the bed is very rough, as it may be when it is covered by artificial ripples, then the theoretical bed level will be lying somewhat lower than the top of the ripples. There seems at present to be no rule from which one can predict the magnitude of this small displacement theoretically. In practice, one determines the level $z = 0$ when fitting the observed velocity profile above the bed to a logarithmic distribution. The quantity z_0 will be determined from the equation

$$z_0 = \frac{k_N}{30} \dots \dots \dots (1)$$

in which k_N = Nikuradse's parameter. k_N can be determined experimentally by fitting the observed velocity profile to a logarithmic profile, as shown by Jonsson and Carlsen (8). If this distribution shall be useful, k_N must obviously be a quantity independent of the wave phase. Probably, k_N depends on the bed geometry only, so that it has the same value in the case of steady unidirectional

flow. Thus, if the bed is covered by artificial ripples, one may actually predict $k_N = 4\eta$, in which η = ripple height.

Consider now the region above $z = z_o$. As mentioned above, there will in general be an overlap layer if the nearbed excursion amplitude, A_b , is great enough. Specifically, Kajiura estimates that the overlap layer is present if the condition

$$\frac{A_b}{k_N} \geq 30 \quad \dots \dots \dots (2)$$

is satisfied. In the following, it will be assumed that the physical conditions are such that the overlap layer exists. The first task is now to choose a reasonable form of the mean turbulent viscosity ν_t in this layer. There seems to be rather wide agreement among research workers that the linear distribution is an adequate one:

$$\nu_t(z) = \kappa \hat{u}_f z \quad \dots \dots \dots (3)$$

in which κ = von Kármán's constant. For clear water, as assumed here, $\kappa = 0.40$. Further, \hat{u}_f = maximum of the bed friction velocity. Eq. 3 will henceforth be adopted in the overlap layer.

The next point is to estimate the position of the boundaries of the overlap layer. Kajiura (9) estimated the lower boundary to be located at the height $z = 15z_o$. As Jonsson (7) has remarked, this seems to be too much. Horikawa and Watanabe (5) plotted the results for ν_t from Jonsson's Test No. 1. It shows that the agreement with the linear form goes down to almost the top of the ripples. (Fig. 1) Making use of this observation, what will be done here is to assume the simplest imaginable picture, namely an overlap layer which extends as far down as to $z = z_o$. It seems natural to expect that the small uncertainties in the location of the lower boundary should not significantly affect the magnitude of the nearbed fluid velocity or its phase.

The overlapping layer will be assumed to extend to $z = \Delta$, where Δ is as yet undetermined. When comparing theory and experiment below, two different proposals for Δ will be investigated. In the outer layer ($z > \Delta$), it will be assumed that ν_t is a constant. Moreover, continuity of ν_t will be required at $z = \Delta$, so that

$$\nu_t = \kappa \hat{u}_f \Delta \quad \dots \dots \dots (4)$$

in the outer layer. The constancy of ν_t in the outer layer and the continuity at $z = \Delta$ are requirements similar to those made by Kajiura. At this point one might wonder if it would not have been more physically reasonable to assume a form of ν_t in the outer layer that decreases with height. For instance, Lundgren (11) assumed a form for ν_t that increased linearly with z for small z and decreased exponentially with z for great z . A form of this kind may actually be more physically satisfactory; in consequence, the basic equation of motion, Eq. 9, in general becomes solvable only by numerical methods. In the outer layer, there is great scatter in the experimental data. Probably, the idea of introducing a time independent turbulent viscosity is not very adequate here. It seems, therefore, to be desirable to keep the form of ν_t as simple as possible in order to be able to give an analytic solution for the fluid velocity.

After establishing the form of the viscosity coefficient, turn now to the basic equation of motion. It may be written as

$$\frac{\partial}{\partial t} [u(z, t) - U(t)] = \frac{\partial}{\partial z} \left[\frac{\tau(z, t)}{\rho} \right] \dots \dots \dots (5)$$

in which $u(z, t)$ = horizontal fluid velocity, $U(t)$ = free stream velocity, i.e., above the boundary layer, $\tau(z, t)$ = shear stress, and ρ = density of water.

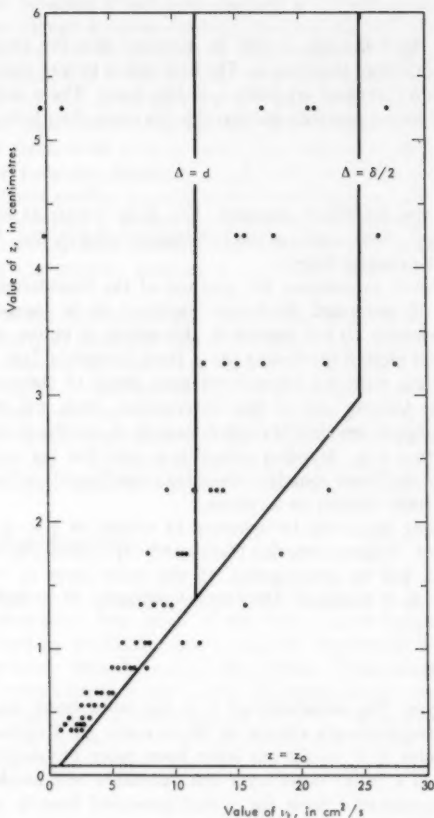


FIG. 1.—Turbulent Viscosity. Data from Jonsson and Carlsen (8)

In Eq. 5, it has been assumed that the nonlinear convective term is negligible. Moreover, it has been assumed that the boundary layer is so thin that the horizontal pressure gradient $\partial p / \partial x$ can be replaced by the term $-\rho dU/dt$ following from potential theory.

Following Jonsson (7) it is convenient to introduce the defect velocity, u_d , measuring the deviation from the free stream velocity:

$$u_d(z, t) = u(z, t) - U(t) \quad \dots \dots \dots (6)$$

The idea of a position dependent but time independent viscosity means that one can write the shear stress as

$$\tau(z, t) = \rho \nu_t(z) \frac{\partial u}{\partial z} \frac{(z, t)}{\partial z} = \rho \nu_t(z) \frac{\partial u_d}{\partial z} \frac{(z, t)}{\partial z} \quad \dots \dots \dots (7)$$

It is now convenient to introduce complex notation. The free stream velocity will be written as $U(t) = U \exp(i\omega t)$, in which U = real velocity amplitude. Similarly, one may write

$$u(z, t) = u(z) e^{i\omega t}, \quad u_d(z, t) = u_d(z) e^{i\omega t} \quad \dots \dots \dots (8)$$

in which $u(z)$ and $u_d(z)$ are in general complex due to the phase shift relative to the free stream velocity. Eq. 5 may now be written as

$$\frac{d}{dz} \left[\nu_t(z) \frac{du_d(z)}{dz} \right] - i\omega u_d(z) = 0 \quad \dots \dots \dots (9)$$

It is fortunate that this equation is explicitly solvable both when $\nu_t(z)$ varies linearly with z and when it is a constant. The solutions will be given in the next section.

SOLUTION OF BASIC EQUATION

Consider first the overlap layer in which $\nu_t(z)$ is given by Eq. 3. Introducing the nondimensional variable,

$$\xi = \left(4\omega \frac{z}{\kappa \hat{u}_f} \right)^{1/2} \quad \dots \dots \dots (10)$$

it turns out that Eq. 9 reduces to the standard differential equation for the Kelvin functions of zeroth order, with ξ as the independent variable (1). It is convenient to write the solution as

$$u_d = UD^{-1} [A(\text{ber } \xi + i\text{bei } \xi) + B(\text{ker } \xi + i\text{kei } \xi)] \quad \dots \dots \dots (11)$$

in which D is a constant quantity defined by

$$\begin{aligned} D = & [(\text{ber}_1 \xi_\Delta - \text{bei}_1 \xi_\Delta) \text{ker } \xi_o - (\text{bei}_1 \xi_\Delta + \text{ber}_1 \xi_\Delta) \text{kei } \xi_o \\ & - (\text{ker}_1 \xi_\Delta - \text{kei}_1 \xi_\Delta) \text{ber } \xi_o + (\text{kei}_1 \xi_\Delta + \text{ker}_1 \xi_\Delta) \text{bei } \xi_o] \\ & + i [(\text{bei}_1 \xi_\Delta + \text{ber}_1 \xi_\Delta) \text{ker } \xi_o + (\text{ber}_1 \xi_\Delta - \text{bei}_1 \xi_\Delta) \text{kei } \xi_o \\ & - (\text{kei}_1 \xi_\Delta + \text{ker}_1 \xi_\Delta) \text{ber } \xi_o - (\text{ker}_1 \xi_\Delta - \text{kei}_1 \xi_\Delta) \text{bei } \xi_o] \quad \dots \dots \dots (12) \end{aligned}$$

In this expression, ber_1 , bei_1 , etc. = first order Kelvin functions (1). The expressions for ξ_o and ξ_Δ are given by Eq. 10 with $z = z_o$ and $z = \Delta$, respectively. The quantities A and B are nondimensional constants, in general complex, that have to be determined from the boundary conditions. The reason it is necessary to keep both A and B in Eq. 11 is connected with the assumed finiteness

of the boundary layer. If, by contrast, the linear variation of v_t with z were assumed to hold for great values of z , then one might put $A = 0$ because the magnitudes of ber and bei increase rapidly for great values of ξ .

Now consider the solution of Eq. 9 in the outer layer, in which v_t is given by Eq. 4. One may write the solution as

$$u_d = -UTD^{-1} \exp [-(1+i)\beta(z-\Delta)] \quad (13)$$

$$\text{in which } \beta = \left(\frac{\omega}{2\kappa \hat{u}_r \Delta} \right)^{1/2} \quad (14)$$

Further, T is a new constant, in general complex. In writing Eq. 13, use has been made of the requirement that $u_d \rightarrow 0$ when $z \rightarrow \infty$. The minus sign in front of the equation has been added for convenience, as the physical defect velocity is ordinarily negative. The solution for u_d in the outer layer may of course also be expressed in terms of ξ , but it is more simple to express it directly in terms of z , in Eq. 13.

It is, in principle, straightforward to determine the complex constants A , B , and T from the boundary conditions at the two interfaces of the boundary layer. First, as $u(z_o) = 0$, i.e., $u_d(z_o) = -U$, one obtains from Eq. 11

$$A(\text{ber } \xi_o + i\text{bei } \xi_o) + B(\text{ker } \xi_o + i\text{kei } \xi_o) = -D \quad (15)$$

Second, continuity of u_d at $z = \Delta$ implies that

$$A(\text{ber } \xi_\Delta + i\text{bei } \xi_\Delta) + B(\text{ker } \xi_\Delta + i\text{kei } \xi_\Delta) = -T \quad (16)$$

Third, there is the condition of continuity of the shear stress at $z = \Delta$. As v_t has been assumed continuous at this level, it follows from Eqs. 7 and 8 that $du_d(z)/dz$ itself is also continuous. This condition leads to the equation

$$A(\text{ber}_1 \xi_\Delta + i\text{bei}_1 \xi_\Delta) + B(\text{ker}_1 \xi_\Delta + i\text{kei}_1 \xi_\Delta) = iT \quad (17)$$

Here use has been made of the relations (1)

$$\text{ber}' \xi + i\text{bei}' \xi = \frac{1-i}{\sqrt{2}} (\text{ber}_1 \xi + i\text{bei}_1 \xi)$$

$$\text{ker}' \xi + i\text{kei}' \xi = \frac{1-i}{\sqrt{2}} (\text{ker}_1 \xi + i\text{kei}_1 \xi) \quad (18)$$

From Eqs. 15, 16, and 17 the constants may be determined:

$$A = \text{ker}_1 \xi_\Delta - \text{kei } \xi_\Delta + i(\text{kei}_1 \xi_\Delta + \text{ker } \xi_\Delta) \quad (19)$$

$$B = -\text{ber}_1 \xi_\Delta + \text{bei } \xi_\Delta - i(\text{bei}_1 \xi_\Delta + \text{ber } \xi_\Delta) \quad (20)$$

$$T = [\text{ber}_1 \xi_\Delta \text{ker } \xi_\Delta - \text{bei}_1 \xi_\Delta \text{kei } \xi_\Delta - \text{ker}_1 \xi_\Delta \text{ber } \xi_\Delta + \text{kei}_1 \xi_\Delta \text{bei } \xi_\Delta] \\ + i[\text{ber}_1 \xi_\Delta \text{kei } \xi_\Delta + \text{bei}_1 \xi_\Delta \text{ker } \xi_\Delta - \text{ker}_1 \xi_\Delta \text{bei } \xi_\Delta - \text{kei}_1 \xi_\Delta \text{ber } \xi_\Delta] \quad (21)$$

The relative simplicity of the expressions for A and B in Eqs. 19 and 20 was the reason the expression for u_d in the overlap layer was given initially as in Eq. 11. Thus, once ξ_o and ξ_Δ are known under given physical circumstances, it is, in principle, straightforward to calculate D , A , B , and T from Eqs. 12, and 19-21 and thereafter calculate u_d . The Kelvin functions may in general

be found from tabular works (1). Note that in the case of small arguments, for instance, when $\xi = \xi_0$, the approximate analytic expressions to the Kelvin functions are often useful. These expressions will not be written down here. The reader is referred to (1).

It may be worthwhile to give the formal expressions for the magnitude \hat{u}_d and the phase ϕ_d of the defect velocity:

$$u_d = -\hat{u}_d e^{-i\phi_d} \quad (22)$$

in which the conventions follow Jonsson (7) (therewith $\phi_d = 0$ at the point in which the fluid velocity u vanishes). Now define, in standard notation, amplitudes and phases of D , A , B and T : $D = \hat{D} \exp i\phi_D$, $A = \hat{A} \exp i\phi_A$, $B = \hat{B} \exp i\phi_B$, $T = \hat{T} \exp i\phi_T$. Similarly, write for the Kelvin functions

$$\text{ber } \xi + i \text{bei } \xi = \hat{M} e^{i\Theta}, \quad \text{ker } \xi + i \text{kei } \xi = \hat{N} e^{i\theta} \quad (23)$$

The final expressions then take the following form. In the overlap layer:

$$\hat{u}_d = U \hat{D}^{-1} [\hat{A}^2 \hat{M}^2 + \hat{B}^2 \hat{N}^2 + 2 \hat{A} \hat{B} \hat{M} \hat{N} \cos(\phi_A - \phi_B + \Theta - \theta)]^{1/2} \quad (24)$$

$$\tan \phi_d = - \frac{\hat{A} \hat{M} \sin(\phi_A - \phi_D + \Theta) + \hat{B} \hat{N} \sin(\phi_B - \phi_D + \theta)}{\hat{A} \hat{M} \cos(\phi_A - \phi_D + \Theta) + \hat{B} \hat{N} \cos(\phi_B - \phi_D + \theta)} \quad (25)$$

whereas in the outer layer:

$$\hat{u}_d = U \hat{T} \hat{D}^{-1} \exp[-\beta(z - \Delta)] \quad (26)$$

$$\phi_d = \beta(z - \Delta) + \phi_D - \phi_T \quad (27)$$

In the expressions on the right, the only quantities varying with z are \hat{M} , \hat{N} , Θ and θ . Amplitudes and phases of the defect velocity are now explicitly calculable inserting Eqs. 12, 14, 19, 20, and 21. It should be noted in passing that ϕ_d in accordance with Eq. 27 varies linearly with z in the outer layer. This is a direct consequence of the assumption that $v_t = \text{constant}$; the linearity as such has no direct bearing on the fact that the present boundary layer is a turbulent one. Qualitatively, the linear variation would be found in a laminar layer also.

Once u_d has been established, it is easy to find the fluid velocity u . Writing

$$u = \hat{u} e^{i\phi} \quad (28)$$

it follows from Eq. 6 that

$$\hat{u} = U \left[1 - 2 \frac{\hat{u}_d}{U} \cos \phi_d + \frac{\hat{u}_d^2}{U^2} \right]^{1/2} \quad (29)$$

$$\sin \phi = \frac{\hat{u}_d}{\hat{u}} \sin \phi_d \quad (30)$$

for all values of z .

COMPARISON WITH EXPERIMENT

Now compare the above theory with Test No. 1 of the Danish measurements (6,7,8). In this case, the existence of the overlap layer was obvious, as A_b/k_N

= 124; see Eq. 2. The wave period was $T = 8.39s$, the Nikuradse parameter $k_N = 0.91$ in. (2.3 cm), and the free stream velocity $U = 83.1$ in./sec (211 cm/s). The theoretical bed level was displaced 0.098 in. (0.25 cm) downwards relative to the top of the bed ripples. When fitting the experimental velocity profile for $u(z, t)$ to a logarithmic form, Jonsson and Carlsen (8) obtained values for $\rho^{-1} \tau_b(t)$ at the bed ranging from 62.0 in./sec² (400 cm²/s²) to 72.1 in./sec² (-465 cm²/s²). This indicates the following choice of friction velocity: $\hat{u}_f = (\hat{\tau}_b/\rho)^{1/2} = (430/\rho)^{1/2}$ cm/s = 20.7 cm/s (8.15 in./sec), which will henceforth be adopted. Correspondingly, $\xi_o = 0.167$.

Using the experimentally determined values for $u(z, t)$ and $\tau(z, t)$, one may calculate time dependent values for $v_i(z, t)$. For convenience, representative values from Jonsson and Carlsen (8) have been plotted in Fig. 1. The points refer to measurements differing 45° in phase. Negative values of v_i have been omitted. The points in the figure indicate that it really makes a reasonable approximation to represent v_i by a time independent, linearly varying function of z in the overlap layer, as was anticipated above in writing Eq. 7. The straight line in the lower part of the figure represents Eq. 3. The inner and outer limits of the overlap layer are, as one must expect, not fixed very accurately by

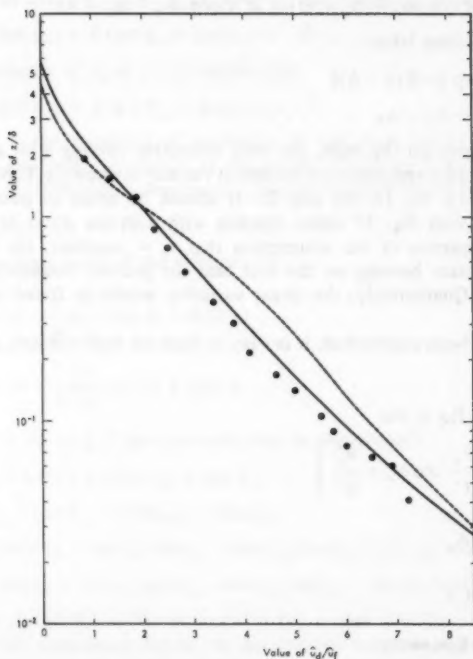


FIG. 2.—Dimensionless Defect Velocity, Relative to $\hat{u}_f = 20.7$ cm/s, $\delta = 6$ cm. Data from Jonsson (7), Test No. 1. —: $\Delta = 1/2 \delta$; - -: $\Delta = d$ (1 m = 3.28 ft)

the data. There seems to be no experimental evidence against extending the overlap layer down to $z = z_0$. Greater uncertainty is associated with determining the outer limit of the overlap layer. To investigate to some extent the sensitivity of the formalism with respect to a variation of the outer limit, two alternatives

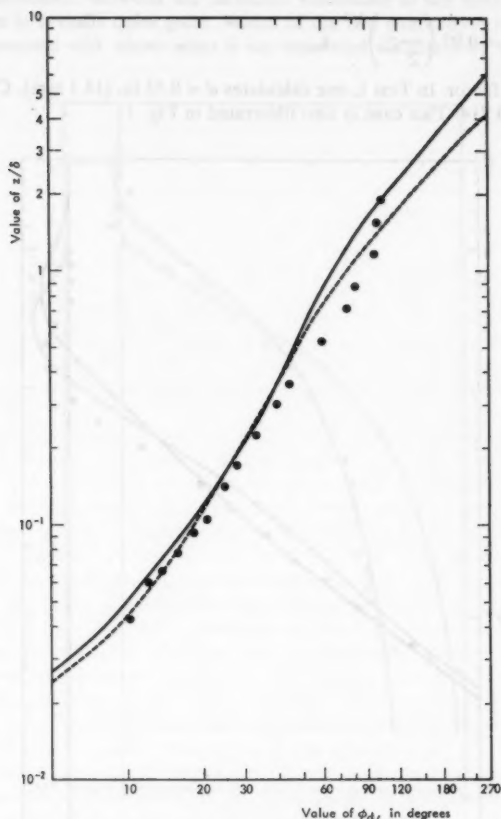


FIG. 3.—Phase of Defect Velocity ($\delta = 6$ cm). Data from Jonsson (7), Test No. 1.
—: $\Delta = 1/2 \delta$; - - : $\Delta = d$ (1 m = 3.28 ft)

for the magnitude of Δ will be worked out here. The first one is to put

$$\Delta = \frac{1}{2} \delta \dots \dots \dots (31)$$

(corresponding to the vertical line to the right in Fig. 1), in which $\delta =$ boundary

layer thickness as defined by Jonsson (7,8). In Test No. 1, δ was determined to be equal to 2.4 in. (6 cm). This case corresponds to $\xi_{\Delta} = 1.042$.

As the second alternative for Δ , Kajiura's expression (9) will be invoked:

$$\Delta = d \dots \dots \dots (32)$$

$$\text{in which } d = 0.05 \left(\frac{1}{2} f_w \right)^{1/2} A_b \dots \dots \dots (33)$$

f_w = friction factor. In Test 1, one calculates $d = 0.55$ in. (14.1 mm). Correspondingly, $\xi_{\Delta} = 0.714$. This case is also illustrated in Fig. 1.

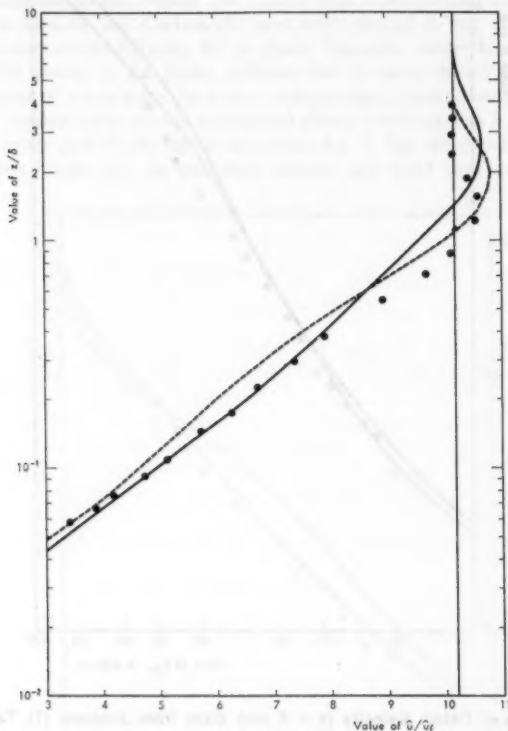


FIG. 4.—Dimensionless Fluid Velocity, Relative to $\hat{u}_f = 20.7$ cm/s $\delta = 6$ cm. Data from Jonsson and Carlsen (7,8), Test No. 1. —: $\Delta = 1/2 \delta$; - -: $\Delta = d$ (1 m = 3.28 ft)

Figs. 2 and 3 show calculated amplitudes and phases of the defect velocity, u_d , and Figs. 4 and 5 show corresponding quantities for the fluid velocity u . The experimental points from Test No. 1 are also shown. It seems in fact

that the two-layer model investigated here yields results in agreement with the observations. The gross features of the empirical variation of amplitudes and phases are reproduced by both the two input values for Δ . It is somewhat surprising to see how insensitive the final curves are with respect to Δ ; in Fig. 1 the difference between the turbulent viscosities in the outer region in the two cases is actually quite great. Which of the two alternatives for Δ yields the best agreement with observation is not answered definitely by the curves;

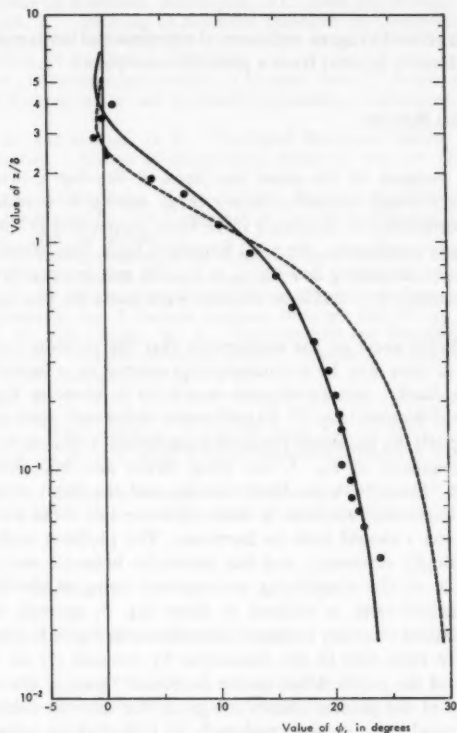


FIG. 5.—Phase of Fluid Velocity ($\delta = 6$ cm). Data from Jonsson (7), Test No. 1. —: $\Delta = 1/2 \delta$; - - : $\Delta = d$ (1 m = 3.28 ft)

in the region close to the wall ($z \lesssim \delta$), it seems yet as if the simple choice, $\Delta = 1/2 \delta$, fits the data most accurately. Especially regarding the phase of the fluid velocity (Fig. 5), this choice for Δ appears to give best agreement.

Kajiura's (9) gives his theoretical amplitudes and phases for the fluid velocity u under the physical conditions of Test No. 1. His figures are thus directly comparable to Figs. 4 and 5 in this paper. Inspection of the figures shows

that the agreement between theory and experiment is almost the same as that in the present case (with $\Delta = 1/2 \delta$) as in Kajiura's case.

Finally it ought to be mentioned that the curves in Fig. 3 are not very different from the straight line determined by the following formula, proposed by Jonsson (7) on empirical grounds,

$$\phi_d = 90^\circ \left(\frac{z}{\delta} \right)^{2/3} \dots \dots \dots (34)$$

This formula was found to agree with several experimental tests, and it, therefore, warrants considerable interest from a practical viewpoint.

SUMMARY AND FINAL REMARKS

1. The main purpose of the paper has been to develop a two-layer theory of the oscillatory rough turbulent layer, thus, aiming at a reduction of the mathematical complexity of Kajiura's three-layer theory (9). In the general case of large excursion amplitudes, the total boundary layer was assumed to consist of an overlap layer, extending down to $z_o = k_N/30$, and an outer layer extending from $z = \Delta$ outwards. Two different choices were made for the input parameter Δ ; see Eqs. 31-33.

2. The calculation rests on the assumption that the periodic variation of the fluid velocities in time may be adequately represented by a harmonic function, $\exp(i\omega t)$. Specifically, this assumption was used in deriving Eq. 9 from the basic equation of motion, Eq. 5. Experimental evidence, such as the Danish Test No. 1, supports the harmonic variation assumption. It should be remembered that, as a consequence of Eq. 7, the shear stress also becomes a harmonic function in time. Thus, both the fluid velocity and the shear stress are in the present theory harmonic functions in time. Observe that from the outset there is no reason u and τ should both be harmonic. The problem under study here is, after all, basically nonlinear, and this particular behavior encountered here is a consequence of the simplifying assumptions being made: first, that the nonlinear convective term is omitted in basic Eq. 5; second, that the time independent turbulent viscosity concept is introduced in Eq. 7. It may be pertinent in this context to refer also to the discussion by Jonsson (7) on the influence the nonlinearity of the problem has on the proposed "laws of the wall."

3. The results of the present theory are given for the two sublayers in Eqs. 10-30, and the results are shown graphically in Figs. 2-5 for parameter values pertinent to the Danish Test No. 1 (6,7,8). Reasonable agreement with the observations is in fact found, thus confirming the usefulness of the two-layer model. In the nearbed region, it appears that the choice $\Delta = 1/2 \delta$ (Eq. 31) gives accurate results. It should be noted, though, that the results are not very critical with respect to different input values for Δ . In conclusion, the obtained results are satisfactory, not only because they show the usefulness of the two-layer model as compared to the more complicated three-layer model, but also because they generally support the idea of introducing a turbulent viscosity, which is independent of time, at least in the nearbed region. This feature facilitates the mathematical treatment of the problem.

ACKNOWLEDGMENT

This work was sponsored by the Royal Norwegian Council for Scientific and Industrial Research under contract No. B 1810.7482.

APPENDIX I.—REFERENCES

1. Abramowitz, M., and Stegun, I. A., ed., *Handbook of Mathematical Functions*, The National Bureau of Standards, Washington, D.C., 1964, pp. 379-433.
2. Dungan Smith, J., "Modeling of Sediment Transport on Continental Shelves," *The Sea*, Vol. 6, *Marine Modeling*, E. D. Goldberg, et al., ed., John Wiley and Sons, Inc., New York, N.Y., 1977, pp. 539-577.
3. Engelund, F., "Waves Superposed on a Current, Part I," *Progress Report No. 49*, Institute of Hydrodynamics and Hydraulic Engineering, Copenhagen, Denmark, 1979, pp. 31-36.
4. Grant, W. D., and Madsen, O. S., "Combined Wave and Current Interaction With a Rough Bottom," *Journal of Geophysical Research*, Vol. 84, No. C4, 1979, pp. 1797-1808.
5. Horikawa, K., and Watanabe, A., "Laboratory Study on Oscillatory Boundary Layer Flow," *Proceedings of the 11th Conference on Coastal Engineering*, London, England, Vol. 1, Sept., 1968, pp. 467-486.
6. Jonsson, I. G., "Measurements in the Turbulent Wave Boundary Layer," *Proceedings of the 10th Congress IAHR*, London, England, Vol. 1, Paper 1.12, 1963, pp. 85-92.
7. Jonsson, I. G., "A New Approach to Oscillatory Rough Turbulent Boundary Layers," *Ocean Engineering*, Vol. 7, Oxford, England, 1980, pp. 109-152.
8. Jonsson, I. G., and Carlsen, N. A., "Experimental and Theoretical Investigations in an Oscillatory Turbulent Boundary Layer," *Journal of Hydraulic Research*, Vol. 14, No. 1, Delft, Holland, 1976, pp. 45-60.
9. Kajiura, K., "A Model of the Bottom Boundary Layer in Water Waves," *Bulletin of the Earthquake Research Institute*, Vol. 46, Tokyo, Japan, 1968, pp. 75-123.
10. Kalkanis, G., "Transportation of Bed Material due to Wave Action," *Technical Memorandum No. 2*, U.S. Army Coastal Engineering Research Center, Washington, 1964.
11. Lundgren, H., "Turbulent Currents in the Presence of Waves," *Proceedings of the 13th Conference on Coastal Engineering*, Vancouver, Canada, Vol. 1, July, 1972, pp. 623-634.

APPENDIX II.—NOTATION

The following symbols are used in this paper:

- A = quantity given in Eq. 19, \hat{A} = amplitude;
 A_b = nearbed excursion amplitude of fluid particles;
 B = quantity given in Eq. 20, \hat{B} = amplitude;
 D = quantity given in Eq. 12, \hat{D} = amplitude;
 d = Kajiura's outer limit, Eq. 33;
 f_w = friction factor;
 k_N = Nikuradse parameter;
 \tilde{M} = amplitude defined in Eq. 23;
 \tilde{N} = amplitude defined in Eq. 23;
 T = quantity given in Eq. 21, \hat{T} = amplitude;
 t = time;
 U = velocity of free stream;
 u = horizontal fluid velocity, \hat{u} = amplitude;

- u_d = defect velocity, \hat{u}_d = amplitude;
 \hat{u}_f = amplitude of bed friction velocity;
 z = height above theoretical bed level;
 β = quantity given in Eq. 14;
 Δ = height of outer limit of overlap layer;
 δ = boundary layer thickness;
 Θ = phase defined in Eq. 23;
 θ = phase defined in Eq. 23;
 κ = von Kármán's constant;
 η_t = turbulent viscosity;
 ξ = quantity defined in Eq. 10, ξ_o and ξ_Δ referring to $z = z_o$ and $z = \Delta$, respectively;
 ρ = density of water;
 τ = shear stress;
 ϕ = phase of u ;
 ϕ_A = phase of A ;
 ϕ_B = phase of B ;
 ϕ_D = phase of D ;
 ϕ_d = phase of u_d , Eq. 22;
 ϕ_T = phase of T ; and
 ω = angular frequency.

TECHNICAL NOTES

Note.—Discussion open until January 1, 1982. To extend the closing date one month, a written request must be filed with the Editor of Technical Publications, ASCE. This paper is part of the Journal of the Waterway, Port, Coastal and Ocean Division, Proceedings of the American Society of Civil Engineers, ©ASCE, Vol. 107, No. WW3, August, 1981.

TECHNICAL NOTES

To provide a place within ASCE for publication of technical ideas that have not advanced, as yet, to the point where they warrant publication as a Proceedings paper in a *Journal*, the publication of Technical Notes was authorized by the Board of Direction on October 16-18, 1967, under the following guidelines:

1. An original manuscript and two copies are to be submitted to the Manager of Technical and Professional Publications, ASCE, 345 East 47th Street, New York, N.Y., 10017, along with a request by the author that it be considered as a Technical Note.
2. The two copies will be sent to an appropriate Technical Division or Council for review.
3. If the Division or Council approves the contribution for publication, it shall be returned to Society Headquarters with appropriate comments.
4. The technical publications staff will prepare the material for use in the earliest possible issue of the *Journal*, after proper coordination with the author.
5. Each Technical Note is not to exceed 4 pages in the *Journal*. As an approximation, each full manuscript page of text, tables, or figures is the equivalent of one-half a *Journal* page.
6. The Technical Notes will be grouped in a special section of each *Journal*.
7. Information retrieval abstracts and key words will be unnecessary for Technical Notes.
8. The final date on which a Discussion should reach the Society is given as a footnote with each Technical Note.
9. Technical Notes will not be included in *Transactions*.
10. Technical Notes will be included in ASCE's annual and cumulative subject and author indexes.

The manuscripts for Technical Notes must meet the following requirements:

1. Titles must have a length not exceeding 50 characters and spaces.
2. The author's full name, Society membership grade, and a footnote reference stating present employment must appear on the first page of the manuscript. Authors need not be Society members.
3. The manuscript is to be submitted as an original copy (with two duplicates) that is typed double-spaced on one side of 8-1/2-in. (220-mm) by 11-in. (280-mm) white bond paper.
4. All mathematics must be typewritten and special symbols must be properly identified. The letter symbols used must be defined where they first appear, in figures or text, and arranged alphabetically in an Appendix.—Notation.
5. Standard definitions and symbols must be used. Reference must be made to the lists published by the American National Standards Institute and to the *Authors' Guide to the Publications of ASCE*.
6. Tables must be typed double-spaced (an original ribbon copy and two duplicate copies) on one side of 8-1/2-in. (220-mm) by 11-in. (280-mm) paper. An explanation of each table must appear in the text.
7. Figures must be drawn in black ink on one side of 8-1/2-in. (220-mm) by 11-in. (280-mm) paper. Because figures will be reproduced with a width of between 3 in. (76 mm) to 4-1/2 in. (110 mm), the lettering must be large enough to be legible at this width. Photographs must be submitted as glossy prints. Explanations and descriptions must be made within the text for each figure.
8. References cited in text must be typed at the end of the Technical Note in alphabetical order in an Appendix.—References.
9. Dual units, i.e., U.S. Customary followed by SI (International System) units in parentheses, should be used throughout the paper.

LINEARIZED SOLUTION TO INLET EQUATION WITH INERTIA

By Todd L. Walton, Jr.,¹ M. ASCE and Francis F. Escoffier,² F. ASCE

Various investigators (4), Van de Kreeke (8), King (5), Goodwin (2), Özsoy (7), Escoffier and Walton (1)] have proposed solutions to the hydraulic flow through inlets problem for simplified type inlet bay systems in which the ocean tide has been assumed sinusoidal and both inlet cross section and bay surface area are constant. Of these solutions, only Özsoy (5), and Escoffier and Walton (6), have retained the inertial term and provided an analytical solution. Additionally, Escoffier and Walton (6) considered the case of tributary inflow in their analytical approach. Özsoy (5) solves the inlet-bay problem with inertia using the describing function technique frequently used in the theory of nonlinear control systems (7), while Escoffier and Walton (6) use a "least squares" linearization approach to the problem.

The present note describes a solution technique using a linearization technique of equating friction-work over the tidal cycle in a nonlinear approach to friction-work in a linear approach, and thus avoids apriori assumptions of the form of bay tide. This method was first used by Lorentz (8) in tidal computations of the Dutch delta works and more recently has been applied by Van de Kreeke (2) in inlet-bay problems.

Starting with the basic equation of motion for one dimensional channel flow

$$\frac{du}{dt} = -g \frac{dh}{dx} - \frac{f}{8R} u|u| \quad \dots \dots \dots (1)$$

in which the advection of momentum term has been neglected and u = inlet channel velocity; g = acceleration of gravity; h = water surface elevation above channel bed; R = channel hydraulic radius; and f = Darcy-Weisbach friction factor. The second term on the right hand side of Eq. 1 can be linearized by the method of Lorentz (8) in the following equation

$$\int_0^{T/4} \frac{f}{8R} u|u| \cdot u \, dt = \int_0^{T/4} \frac{f}{8R} \kappa u \cdot u \, dt \quad \dots \dots \dots (2)$$

tidal work non-linear = tidal work linear.

¹Hydr. Engr., Evaluation Branch, Coastal Engrg. Research Center, Kingman Bldg., United States Army, Fort Belvoir, Va. 22060.

²Retired; formerly Chf., Hydr. and Sanitary Section, United States Army Corps of Engineers, Mobile, Ala.

Note.—Discussion open until January 1, 1982. To extend the closing date one month, a written request must be filed with the Manager of Technical and Professional Publications, ASCE. Manuscript was submitted for review for possible publication on March 26, 1980. This paper is part of the Journal of the Waterway, Port, Coastal and Ocean Division, Proceedings of the American Society of Civil Engineers, ©ASCE, Vol. 107, No. WW3, August, 1981.

If one assumes a harmonic channel velocity and performs the required integration the linear constant can be found as

$$\kappa = \frac{8}{3\pi} U_m \dots \dots \dots (3)$$

in which U_m = maximum channel velocity.

Integrating from the ocean end of the channel to the bay end

$$\frac{L}{g} \frac{du}{dt} + \frac{F}{2g} \left(\frac{8}{3\pi} U_m \right) u + h_b = h_o \dots \dots \dots (4)$$

in which $F = fL/4R$ = dimensionless friction parameter; h_b = elevation of water surface in bay; h_o = elevation of water surface in ocean; and L = effective length of inlet.

From continuity

$$u a_c = \frac{dh_b}{dt} A \dots \dots \dots (5)$$

in which a_c = cross-sectional area in gorge of inlet, A = water surface area of bay.

Combining Eqs. 4 and 5, assuming a sinusoidal ocean tide, and using the following defined dimensionless parameters

$$\hat{h}_o = \frac{h_o}{a_o} = \sin \sigma t = \sin \omega \tau$$

$$\hat{h}_b = \frac{h_b}{a_o}$$

$$\omega = \sigma \left(\frac{LA}{ga_c} \right)^{1/2}$$

$$\tau = t \left(\frac{ga_c}{LA} \right)^{1/2}$$

in which $\sigma = 2\pi/T$; T = tidal period; and a_o = ocean tide amplitude.

A dimensionless linear differential equation can be found

$$\frac{d^2 \hat{h}_b}{d\tau^2} + B \frac{d\hat{h}_b}{d\tau} + \hat{h}_b = \sin \omega \tau \dots \dots \dots (6)$$

in which $B = (F/2L)(LA/ga_c)(8/3\pi) U_m$.

The solution to equation 6 can be readily found to be

$$\hat{h}_b = \zeta \sin(\omega \tau - \epsilon) \dots \dots \dots (7)$$

in which $\zeta = a_b/a_o$ = bay response factor or "amplification" factor; a_b = bay tide amplitude.

$$\text{and } \zeta = [(1 - \omega^2)^2 + \omega^2 B^2]^{-1/2} \dots \dots \dots (8)$$

$$\epsilon = \tan^{-1} \left(\frac{\omega B}{1 - \omega^2} \right) = \text{bay phase lag} \dots \dots \dots (9)$$

As B has an implicit measure bay response U_m in it, another equation is needed to find U_m and thus ζ and ϵ in explicit form. An equation for U_m can be found by equating the tidal prism over a half tidal cycle to the flow through the inlet in the same time period.

$$\text{Tidal prism} = 2 a_b A = \int_0^{T/2} u a_c dt \dots \dots \dots (10)$$

From Eq. 10 U_m can be found as

$$U_m = \sigma a_0 \left(\frac{A}{a_c} \right) \zeta \dots \dots \dots (11)$$

Using Eqs. 8, 9, and 11, the following explicit representations of bay tide response factor, ζ , and bay phase lag ϵ can be found

$$\zeta = \left(\frac{\left[(1 - \omega^2)^4 + 4 \left(\frac{8D}{3\pi} \omega^2 \right)^2 \right]^{1/2} - (1 - \omega^2)^2}{2 \left(\frac{8D}{3\pi} \omega^2 \right)^2} \right)^{1/2} \dots \dots \dots (12)$$

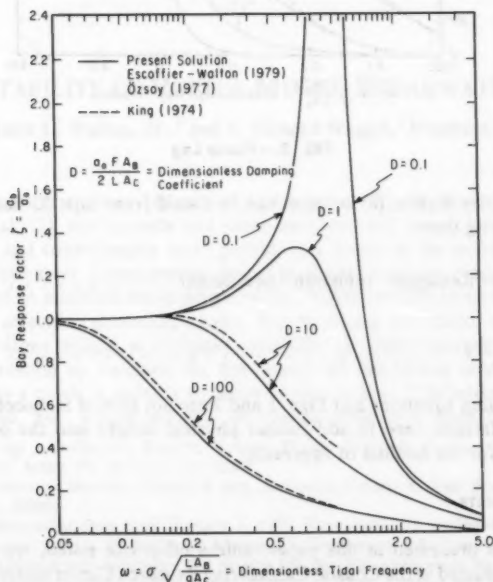


FIG. 1.—Bay Response

$$\epsilon = \tan^{-1} \left(\frac{\zeta \left(\frac{8D}{3\pi} \omega^2 \right)}{1 - \omega^2} \right) \quad (13)$$

in which $D = a_0 F A / 2 L a_c$ = dimensionless "damping" coefficient.

Note that the ω of this note corresponds to $\nu^{1/2}$ of Escoffier-Walton (1).

Graphical solutions of Eqs. 12 and 13 are presented in Figs. 1 and 2 for various values of the "damping" coefficient. It is noted that all solutions presented in Figs. 1 and 2 correspond well, with three of the solutions providing exactly the same answers [Özsoy (5), Escoffier-Walton (6), and present solution].

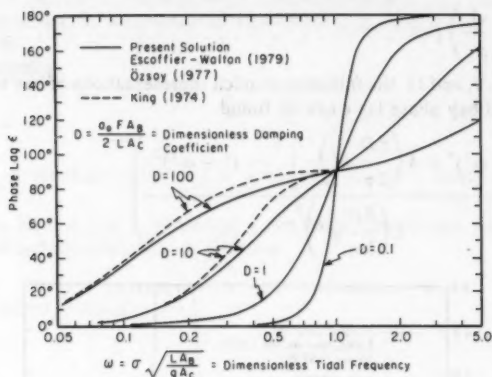


FIG. 2.—Phase Lag

The Escoffier-Walton (6) solution can be found from Eqs. 22 and 23 of that paper by noting that

$$K = \frac{1}{\omega D^{1/2}} = \text{Keulegan "repletion" coefficient} \quad (14)$$

$$\text{and } \epsilon = \frac{\pi}{2} - \tau \quad (15)$$

The preceding equations and Figs. 1 and 2 are not plotted in Escoffier-Walton (6) but are detailed here to add further physical insight into the problem and justification for the method of approach.

ACKNOWLEDGMENTS

The results presented in this paper, unless otherwise noted, were based on research conducted at the Coastal Engineering Research Center under the Coastal Engineering Research Program of the United States Army Corps of Engineers. Permission to publish this information is appreciated.

APPENDIX.—REFERENCES

1. Escoffier, F. F., and Walton, T. L., Jr., "Inlet Stability Solutions for Tributary Inflow," *Journal of the Waterway, Port, Coastal and Ocean Division*, ASCE, Vol. 105, No. WW4, Proc. Paper 14964, Nov., 1979, pp. 341-355.
2. Goodwin, C. R., "Estuarine Tidal Hydraulics," thesis presented to Oregon State University, at Corvallis, Oreg., in 1974, in partial fulfillment of the requirements for the degree of Doctor of Philosophy.
3. Graham, D., and McRuer, D., *Analysis of Nonlinear Control Systems*, Dover Publications, New York, N.Y., 1971.
4. Keulegan, G. H., "Tidal Flow in Entrances Water-Level Fluctuations of Basins in Communications with Seas," *Technical Bulletin No. 14*, Committee on Tidal Hydraulics, United States Army Engineer Waterways Experimental Station, Vicksburg, Miss., July, 1967.
5. King, D. B., "The Dynamics of Inlets and Bays," *Technology Report No. 22*, University of Florida, Gainesville, Fla., 1974.
6. Lorentz, H. A., "Verslag Staatscommissie Zuiderzee 1918-1926," *Staatsdrukkerij*, The Hague, Netherlands, 1926.
7. Van de Kreeke, J., "Water Level Fluctuations and Flow in Tidal Inlets," *Journal of the Waterway, Port, Coastal and Ocean Division*, ASCE, Vol. 93, No. WW4, Proc. Paper 5575, Nov., 1967, pp. 97-106.

STABILITY OF RUBBLE MOUND BREAKWATERS

By Todd L. Walton, Jr.,¹ and J. Richard Weggel,² Members, ASCE

Numerous investigators [Ahrens and McCartney (2), Thomsen, et al. (1972), Bruun, et al. (2), and Losada and Gimenez-Curto (6)] have shown that wave steepness, and consequently wave period, is a factor in the stability of rubble mound breakwaters. Some present design methods (5) do not explicitly consider wave period. A modified wave steepness dependent stability number, accounting for inertia effects is presented herein. The following derivation of an equation for armor stone weight at incipient instability (motion) generally parallels an earlier derivation by Raichlen (6), but retains lift and inertia terms in the final analysis. As a result, a stability equation similar to that of Iribarren and Nogales (7) is found, but, which includes an inertial parameter dependent on wave

¹Hydr. Engr., Evaluation Branch, Coastal Engrg. Research Center, Kingman Bldg., United States Army, Ft. Belvoir, Va. 22060.

²Chf. Evaluation Branch, Coastal Engrg. Research Center, United States Army, Fort Belvoir, Va. 22060.

Note.—Discussion open until January 1, 1982. To extend the closing date one month, a written request must be filed with the Manager of Technical and Professional Publications, ASCE. Manuscript was submitted for review for possible publication on April 15, 1980. This paper is part of the *Journal of the Waterway, Port, Coastal and Ocean Division*, Proceedings of the American Society of Civil Engineers, ©ASCE, Vol. 107, No. WW3, August, 1981.

steepness, H/L . Rubble mound armor stability is reduced when the inertia parameter becomes important.

Raichlen (6) has shown that when moments are taken about the point of contact (support) of an armor unit for the condition of incipient motion as shown in Fig. 1, the following equation can be found:

$$(F_D + F_I)c_1 l \cos \theta + F_L c_1 l \sin \theta = (\rho_s - \rho_w) g c_1 c_3 l^4 \sin (\theta - \alpha) \quad (1)$$

$$\text{in which } F_D = \frac{\rho_w}{2} C_D (c_2 l^2) u |u|, \quad (\text{drag force}) \quad (2)$$

$$F_I = \rho_w C_M (c_3 l^3) \left(\frac{du}{dt} \right), \quad (\text{inertia force}) \quad (3)$$

$$\text{and } F_L = \frac{\rho_w}{2} C_L (c_2 l^2) u^2, \quad (\text{lift force}) \quad (4)$$

and C_D , C_L , and C_M = the drag coefficient, the lift coefficient, and the virtual-mass coefficient respectively; θ = the angle of repose of the armor

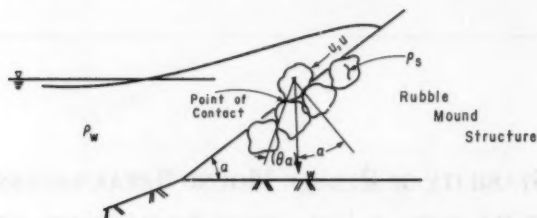


FIG. 1.—Definition Sketch for Incipient Motion of Armor Units [from Raichlen (6)]

unit; α = the angle the structure slope makes with the horizontal; l = a characteristic length of the armor unit; and $c_1 l$ = the distance from the point of support to the center of gravity of the unit; $c_2 l^2$ = the projected cross section area of the unit on a plane perpendicular to the direction of the velocity; and $c_3 l^3$ = the volume of the unit.

The terms, F_D and F_I , are the drag and inertia forces formulated similar to Morison, et al. (8). Noting that the weight of the armor stone is given by

$$W = \rho_s g c_3 l^3 \quad (5)$$

in which ρ_s = density of stone

$$\text{and that } \frac{\sin (\theta - \alpha)}{\cos \theta} = \tan \theta \cos \alpha - \sin \alpha \quad (6)$$

$$\text{and } S = \frac{\rho_s - \rho_w}{\rho_w} \quad (7)$$

it can be shown assuming that velocity up the slope is positive that

$$-u|u| \left(1 + \frac{C_L}{C_D} \tan \theta \right) = g \left(\frac{2c_3}{c_2 C_D} \right) \left(\frac{W}{\rho_s g c_3} \right)^{1/3} \left((S-1) (\tan \theta \cos \alpha - \sin \alpha) - \frac{C_M}{g} \frac{du}{dt} \right) \quad (8)$$

Assuming shallow water theory the velocity can be written as

$$u = \frac{\eta C}{h} \quad (9)$$

in which η = water surface elevation above the mean water level; C = wave celerity = \sqrt{gh} ; and h = water depth.

The water surface elevation η , is given by

$$\eta = \frac{H}{2} \sin \Psi \quad (10)$$

in which H = wave height; Ψ = wave phase angle = σt ; $\sigma = 2\pi/T$; t = phase time; and T = wave period.

It can be shown that

$$u|u| = \frac{gH}{\kappa} \sin \Psi |\sin \Psi| \quad (11)$$

$$\text{in which } \kappa = \frac{4h}{H} \quad (12)$$

$$\text{and } \frac{du}{dt} = \frac{\sigma HC}{2h} \cos \Psi = g\pi \left(\frac{H}{L} \right) \cos \Psi \quad (13)$$

The stability equation can then be solved for the weight of rock giving

$$W = \frac{c_3}{\left(\frac{2c_3\kappa}{c_2 C_D} \right)^3} \cdot \frac{-\rho_s g H^3 \left(1 + \frac{C_L}{C_D} \tan \theta \right) \sin^3 \Psi |\sin^3 \Psi|}{\left((S-1) (\tan \theta \cos \alpha - \sin \alpha) + C_M \pi \left(\frac{H}{L} \right) \cos \Psi \right)^3} \quad (14)$$

Defining N as a stability number given by

$$N = c_3 \left(\frac{2c_3\kappa}{c_2 C_D} \right)^{-3} \quad (15)$$

Assuming no lift force ($C_L = 0$) and no inertia force ($C_M = 0$) an equation similar to Iribarren and Nogales' (7) can be found if the peak downslope velocity is taken at its maximum ($\sin \Psi = -1$).

$$W = \frac{N \rho_s g H^3}{(Sg - 1)^3 (\tan \theta \cos \alpha - \sin \alpha)^3} \quad (16)$$

By retaining inertia and lift force terms, and shifting the wave phase angle,

Ψ , by π radians to reflect downslope velocities and accelerations, Eq. 16 can be rewritten as

$$W = \frac{N \rho_s g H^3 \left(1 + \frac{C_L}{C_D} \tan \theta \right) \sin^3 \Psi |\sin^3 \Psi|}{\left((Sg - 1)(\tan \theta \cos \alpha - \sin \alpha) - C_M \pi \left(\frac{H}{L} \right) \cos \Psi \right)^3} \dots \dots \dots (17)$$

Eq. 17 shows that the inertia force can lead to an instability phenomenon in which wave steepness is a critical factor.

As present model tests of rubble mound structures do not explicitly consider inertia, stability numbers of the "Hudson" (9) type such as N or K_D (in which $K_D = (\tan \theta \cos \alpha - \sin \alpha) / N \cot \alpha$ should be looked at critically when rubble mound structures are to be built utilizing laboratory stability numbers based on experiments conducted with wave steepness lower than those actually occurring at a field site.

On dividing Eq. 17 by $(S - 1)(\tan \theta \cos \alpha - \sin \alpha)$ a modified stability equation can be found of the form

$$W = W' P_s \dots \dots \dots (18)$$

$$\text{in which } W' = \frac{N \rho_s g H^3 \left(1 + \frac{C_L}{C_D} \tan \theta \right)}{(S - 1)^3 (\tan \theta \cos \alpha - \sin \alpha)^3} \dots \dots \dots (19)$$

$$\text{and } P_s = \frac{\sin^3 \Psi |\sin^3 \Psi|}{(1 - R \cos \Psi)^3} \dots \dots \dots (20)$$

$$\text{in which } R = \frac{C_M \pi \left(\frac{H}{L} \right)}{(S - 1)(\tan \theta \cos \alpha - \sin \alpha)} \dots \dots \dots (21)$$

P_s can be thought of as a "phase stability" number and R , and "inertia-gravity ratio" number.

As typical design would be in accordance with an equation of the type which would give a rock weight equal to W' , the designer should insure that site conditions do not produce a maximum P_s value greater than that produced in the laboratory tests on which the stability is based.

As an example, typical rubble mound breakwaters encompass slope angles from 1 on 3 (18.4°)–1 on 1.5 (33.7°). Typical design wave steepness might range from 0.01–0.10 (in which 0.14 is the deep water limiting wave steepness). Assuming an angle of repose, $\tan \theta = 1.0$ [see, e.g., Hedar (10)]; $S = 2.65$; and an inertia coefficient $C_M = 1.5$ (for a hemisphere on a plane surface); a typical range of R values would be $R = 0.045$ – 1.030 , with the higher value corresponding to the steeper slope (1 on 1.5) and larger wave steepness ($H/L = 0.10$).

Plots of Ψ max (phase angle corresponding to maximum P_s) versus R , and P_s versus R are given in Figs. 2 and 3. These figures provide some insight into conditions for which inertia effects become important. From Fig. 2 it is

apparent that as R increases P_s increases until as R approaches 1.0, P_s is much larger than it is for the case when inertia conditions are not considered ($R = 0, P_s = 1.0$). It is also apparent that high wave steepness and large rubblemound slope angles could be critical in design should laboratory model tests not encompass the same range of wave steepness characteristic of the site.

Eqs. 20 and 21 may also be used to establish a maximum allowable structure slope. Structures built having slopes steeper than the allowable slope run the

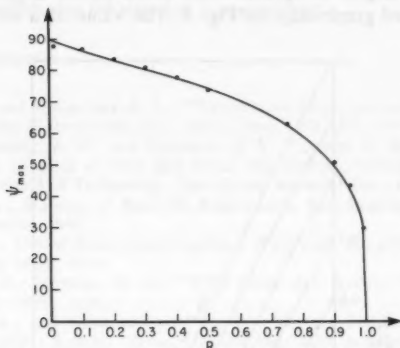


FIG. 2.—Plot of Phase Maximum Versus Inertia-Gravity Parameter Ratio

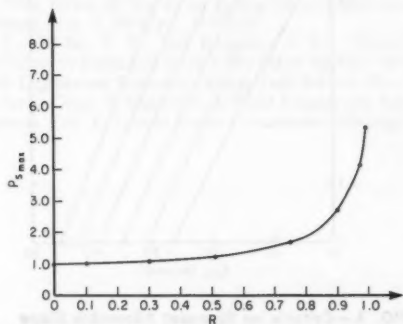


FIG. 3.—Plot of Phase Stability Number Versus Inertia-Gravity Parameter Ratio

risk of damage due to inertial effects. Fig. 3 suggests that values of R greater than about 0.5 will result in values of P_s greater than about 1.25 or the required armor unit weight may be under estimated by 25% unless a conservative stability coefficient is used. For larger values of R , the situation is worse; thus, some maximum value of R can be established beyond which an unacceptable risk of failure exists. The maximum wave steepness H/L and inertia coefficient, C_M , and the value of S along with the angle of repose for the armor, θ , then

determine a maximum structure slope. From Eq. 21

$$\tan \theta \cos \alpha - \sin \alpha = \frac{C_M \pi \left(\frac{H}{L} \right)}{(S-1) R} \quad (22)$$

in which the value of H/L is the largest expected waves steepness at the site and R is the largest acceptable value based on the largest acceptable P_s . Eq. 22 is presented graphically on Fig. 4. The value of α satisfying equation

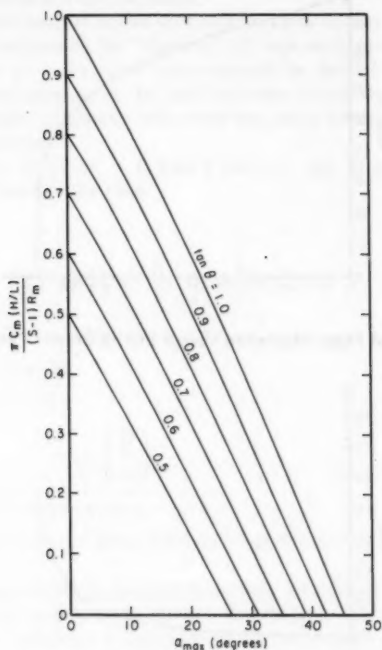


FIG. 4.—Criteria for Steepest Allowable Slope

22 establishes the steepest allowable structure slope. For example, if $C_M = 1.5$, $(H/L)_{\max} = 0.05$, $S = 2.65$, $\tan \theta = 1.0$ and the maximum R is 0.5 (corresponding to $P_s = 1.25$) then

$$\frac{C_M \pi \frac{H}{L}}{(S-1) R} = \frac{1.5 \pi (0.05)}{1.65 (0.5)} = 0.286 \quad (23)$$

From Fig. 3, for $\tan \theta = 1.0$, $\alpha_{\max} = 33.5^\circ$ or $\cot \theta = 1.51$. Slopes steeper than

1:1.5 could thus experience damage if the stability tests upon which the design was based did not encompass values of H/L as great as $H/L = 0.05$.

ACKNOWLEDGMENTS

The results presented in this paper, unless otherwise noted, were based on research conducted at the Coastal Engineering Research Center under the Coastal Engineering Research Program of the United States Army Corps of Engineers. Permission to publish this information is appreciated.

APPENDIX.—REFERENCES

1. Ahrens, J. P., and McCartney, B. L., "Wave Period Effect on the Stability of Riprap," *Civil Engineering in the Oceans/III*, ASCE, June, 1975, pp. 1019-1034.
2. Bruun, P., Günbak, A. R., and Kjelstrup, S. V., "Design of Mound Breakwaters," *Report No. 6*, Director of Port and Ocean Engineering, University of Trondheim, Norwegian Institute of Technology, Trondheim, Norway, Oct., 1979.
3. Hendor, P. A., *Stability of Rock-fill Breakwaters*, Scandinavian University Books, Göteborg, Sweden, 1960.
4. Hudson, R. Y., *United States Army Engineers Waterways Experimental Station Report 2-2*, Vicksburg, Miss., 1958.
5. Iribarren, C. R., Nogales, O. C., "XVII Perm. Int. Assoc., Navig. Congr. Sect. II," *Subject 3:119 39*, 1953.
6. Losada, M. A., and Gimenez-Curto, L. A., "On the Stability of Rubble Mound Breakwaters Under Regular Waves," *Proceedings Fifth International Conference on Port and Ocean Engineering*, August, 1979.
7. Morison, J. R., O'Brien, M. P., Johnson, J. W., and Schaaf, S. A., *American Institute Mining Metall. Petr. Eng. Petr. trans.* 189 (TP2846):149-54, 1950.
8. Raichlen, F., "The Effect of Waves on Rubble-Mound Structures," *Annual Review of Fluid Mechanics*, Vol. 7, 1975, pp. 327-356.
9. Thomsen, A. L., Wohlt, P. E., and Harrison, A. S., "Riprap Stability on Earth Embankments Tested in Large and Small-Scale Wave Tanks," *Technical Memorandum No. 37*, Coastal Engineering Research Center, Fort Belvoir, Va., June, 1972.
10. United States Army Corps of Engineers, *Coastal Engineering Research Center, Shore Protection Manual*, Vol. 2, United States Government Printing Office, Washington, D.C., 1977.

PARTICLE MOTION UNDER STOKES WAVES

By Eliezer Kit¹ and Michael Stiassnie²

We recall two well documented facts, see Phillips (1). First, the Eulerian mean velocity (averaged over a wave period) at any point below the wave troughs is exactly zero, thus causing zero mean mass flux across any vertical control section between the bottom and a fixed point deeper than the troughs. Second, the Lagrangian mean velocity of all water particles is a nonzero second order quantity, and is always in the wave propagation direction. At first sight, it seems justified to ask, as probably many students do, how can it be that while all individual particles move forward, the mean mass flux across the control section remains zero? In the present note we present, what is hoped to be, a clear and descriptive answer to this question.

In Fig. 1 we show the pathlines of four selected water particles during one wave period, starting from the instant in which the particles near the control section AB are moving upwards. Particle 1 crosses the section AB twice during a wave period and contributes nothing to the mean mass flux. Particle 2, which starts from a location nearer to AB crosses the control section only once, from left to right, thus contributing to a positive mass flux. (The writers define the flux in the wave propagation direction "as positive.") All particles in zone 1, (the zone shaded with horizontal lines) are the same type as particle 2. The width c of this zone is identical with the particle displacement during a wave period and is given, according to Phillips, as follows:

$$c = \pi k \alpha^2 \cdot \frac{ch [2k(z+h)]}{sh^2(kh)} \dots \dots \dots (1)$$

in which α is the wave amplitude, k the wave-number and h the mean water depth.

The area of zone 1, A_1 , is given by

$$A_1 = \int_{-h}^{-H} c(z) dz = \frac{\pi \alpha^2}{2} \cdot \frac{sh [2k(h-H)]}{sh^2(kh)} \dots \dots \dots (2)$$

where H is the depth of the point B beneath the mean water surface ($H > \alpha$).

It can be shown, accurate to order α^2 for the mass flux, that all particles

¹Research Engr., Coastal and Marine Research Inst., Technion-City, Haifa, Israel.

²Senior Lect., Faculty of Civ. Engrg., Technion-Israel Inst. of Tech., Haifa, Israel.

Note.—Discussion open until January 1, 1982. To extend the closing date one month, a written request must be filed with the Manager of Technical and Professional Publications, ASCE. Manuscript was submitted for review for possible publication on March 11, 1980. This paper is part of the Journal of the Waterway, Port, Coastal and Ocean Division, Proceedings of the American Society of Civil Engineers, ©ASCE, Vol. 107, No. WW3, August, 1981. ISSN 0148-9895/81/0003-0202/\$01.00.

at the initial instant. Thus the area of the relevant part of zone 2 is decreasing from πab , for B at $z < \alpha$, to zero, for B at $z = \alpha$, causing the mean flux to increase from zero to $\pi \alpha^2 / T \coth(kh)$, as should be expected.

A new approach is used in this short note to show that, despite the fact that all individual water particles move forward, the mean mass flux across a vertical control section (from the bottom to a point located below the wave troughs) remains zero.

APPENDIX.—REFERENCE

1. Phillips, O. M., *The Dynamics of the Upper Ocean*, Section 3.3, Cambridge University Press, Cambridge, England, 1977.

DISCUSSION

Note.—This paper is part of the Journal of the Waterway, Port, Coastal and Ocean Division, Proceedings of the American Society of Civil Engineers, ©ASCE, Vol. 107, No. WW3, August, 1981. ISSN 0148-9895/81/0003-0207/\$01.00.

DISCUSSIONS

Discussions may be submitted on any Proceedings paper or technical note published in any *Journal* or on any paper presented at any Specialty Conference or other meeting, the *Proceedings* of which have been published by ASCE. Discussion of a paper/technical note is open to anyone who has significant comments or questions regarding the content of the paper/technical note. Discussions are accepted for a period of 4 months following the date of publication of a paper/technical note and they should be sent to the Manager of Technical and Professional Publications, ASCE, 345 East 47th Street, New York, N.Y. 10017. The discussion period may be extended by a written request from a discussor.

The original and three copies of the Discussion should be submitted on 8-1/2-in. (220-mm) by 11-in. (280-mm) white bond paper, typed double-spaced with wide margins. The length of a Discussion is restricted to two *Journal* pages (about four typewritten double-spaced pages of manuscript including figures and tables); the editors will delete matter extraneous to the subject under discussion. If a Discussion is over two pages long it will be returned for shortening. All Discussions will be reviewed by the editors and the Division's or Council's Publications Committees. In some cases, Discussions will be returned to discussors for rewriting, or they may be encouraged to submit a paper or technical note rather than a Discussion.

Standards for Discussions are the same as those for Proceedings Papers. A Discussion is subject to rejection if it contains matter readily found elsewhere, advocates special interests, is carelessly prepared, controverts established fact, is purely speculative, introduces personalities, or is foreign to the purposes of the Society. All Discussions should be written in the third person, and the discussor should use the term "the writer" when referring to himself. The author of the original paper/technical note is referred to as "the author."

Discussions have a specific format. The title of the original paper/technical note appears at the top of the first page with a superscript that corresponds to a footnote indicating the month, year, author(s), and number of the original paper/technical note. The discussor's full name should be indicated below the title (see Discussions herein as an example) together with his ASCE membership grade (if applicable).

The discussor's title, company affiliation, and business address should appear on the first page of the manuscript, along with the *Proceedings* paper number of the original paper/technical note, the date and name of the *Journal* in which it appeared, and the original author's name.

Note that the discussor's identification footnote should follow consecutively from the original paper/technical note. If the paper/technical note under discussion contained footnote numbers 1 and 2, the first Discussion would begin with footnote 3, and subsequent Discussions would continue in sequence.

Figures supplied by the discussor should be designated by letters, starting with A. This also applies separately to tables and references. In referring to a figure, table, or reference that appeared in the original paper/technical note use the same number used in the original.

It is suggested that potential discussors request a copy of the *ASCE Authors' Guide to the Publications of ASCE* for more detailed information on preparation and submission of manuscripts.

MIXING OF BUOYANT SURFACE JET OVER SLOPING BOTTOM^a

Closure by Bijan Safaie,³ A. M. ASCE

The writer would like to thank Adams for his interest in the writer's work and for his valuable discussion. It appears further clarification and discussion on the mechanism of separation and the corresponding normalization is warranted. This, together with the writer's comments on the points brought up by the discussor, is presented in the following.

The writer's observation, from the side glass window, indicated that the mechanism of separation was very similar to that of a buoyant ball entering a fluid with certain initial kinetic energy. In fact, one can show that, neglecting friction, such a ball can penetrate in the vertical direction to a limited distance, say $L \propto V^2/g'$, in which L = the maximum penetration of the ball; V = the velocity of the ball in the vertical direction; and g' = the modified gravitational acceleration based on the density of the ball and the fluid. The movement of large-scale turbulent eddies were very similar to that of the buoyant ball previously mentioned. This observation led the writer to select kinetic energy flux and buoyancy flux as important parameters in forming the proper length scale, L_3 . Based on these observations, the water depth at the separation point can physically be interpreted as the maximum depth which large-scale eddies can penetrate. Based on these comments and the available experimental data, the following observations can be made:

1. The normalized maximum penetration depth is a function of source densimetric Froude number, $F_o(h)$, only and is independent of both aspect ratio and bottom slope. This can be seen in Fig. 11 where data points correspond to various values of aspect ratio and bottom slope. The same functional relationship is expected for maximum penetration depth of surface buoyant jets discharged into deep water. Carter's data shown in Fig. 11 substantiates this hypothesis by noting that his data is for BSJ discharged into deep water and that they follow other data points closely. Therefore, experimental evidence does not support the finding in Ref. 24 that ϕ = constant in Eq. 33 for surface jets in deep water.

2. Although the dimensional analysis and normalization of h_s presented by the discussor is valid, the normalization which was used to obtain Fig. 11 has an advantage in unifying the data points which were obtained under dissimilar conditions.

3. In general, based on the experience with submerged buoyant jets, Q_o and A_s were expected to have small effects on the dynamics of the BSJ, however, this is not a valid assumption for BSJ over sloping bottom. Note that experimental

^aNovember, 1979, by Bijan Safaie (Proc. Paper 14954).

³Asst. Prof. of Civ. Engrg., State Univ. of New York, Parker Engrg. Building, Buffalo, N.Y. 14214.

evidence obtained from various sources substantiate this point (see Fig. 13).

4. The writer suggested that the lateral extent of the attachment region to be approximately equivalent to the nonbuoyant spread of a turbulent jet with the same source geometry and velocity. This was based on the flow visualization using dye crystals and photographs. Other methods of determination might result in different values, moreover, very accurate determination of the lateral extent of attachment region experimentally is rather difficult by noting that the angle of spread for nonbuoyant jets is approx 9° – 12° .

INLET STABILITY SOLUTIONS FOR TRIBUTARY INFLOW^a

Closure by Francis F. Escoffier,⁶ F. ASCE
and Todd L. Walton, Jr.,⁷ M. ASCE

The writers would like to thank Bruun and Mehta for their interesting discussions and for drawing attention to the notions of inlet stability as opposed to inlet equilibrium. Bruun discusses the subject of inlet equilibrium where sedimentary "equilibrium" implies that an inlet channel flushes as much sand away as it takes in by littoral drift feeder currents. The writers refer to hydraulic "stability" rather than sedimentary "equilibrium" as the title of the paper implies. The writers concur with Bruun that littoral drift imposes different constraints on the inlet. This has been taken into consideration by a varying factor p as given in Eq. 46 which depends on the method in which the channel fills. It is recognized that due to varying wave action on different shores that different values of p would result. Sedimentary equilibrium can best be expressed as Bruun (11) has noted by a constant inlet channel velocity for a particular exposed shoreline.

It is mistakenly noted by Bruun that Walton and Adams (16) work on outer inlet shoals versus tidal prism does not account for wave action when, in fact, a criteria for wave action has been taken into account by a wave energy parameter $H^2 T^2$ (in which H = wave height; and T = wave period).

The writers concur with Bruun in his comment that "it is dangerous to accept fixed ratios or too strict generalizations on inlet behavior." As is too often the case, inlets seem to have a "sixth sense" of their own which continues to defy the engineers attempts to quantify them. If progress is too be made though, such attempts must be tried and judged accordingly as qualitative arguments lack the substance on which to base sound engineering decisions.

^aNovember, 1979, by Francis F. Escoffier and Todd L. Walton, Jr. (Proc. Paper 14964).

⁶Retired; formerly Chf., Hydr. and Sanitary Section, U.S. Army Corps of Engrs., Mobile, Ala.

⁷Hydr. Engr., Evaluation Branch, Dept. of the Army, Coastal Engr. Research Center, Corps of Engrs., Kingman Building, Fort Belvoir, Va. 22060; formerly Asst. Prof., Extension, Marine Advisory Program, Coastal and Oceanographic Engr. Lab., Univ. of Florida, Gainesville, Fla.

WAVE FORCE ANALYSIS: AN ALTERNATE PROCEDURE^a

Closure by Yuan Jen,³ M. ASCE

The writer would like to thank Garrison for his constructive comments. The writer fully realizes the complexity of the flow phenomenon and the limitation of the method suggested in the original paper, and wishes to clarify a few points that might have mislead the readers.

The proposed method of wave force analysis was in fact based on the premise that the forces acting on a section of a cylindrical pile can be described by the particle velocity, acceleration, pile diameter and fluid properties (Eq. 1). The physical meaning of this assumption was adequately described in the original paper. The writer fully agrees with Garrison that the particle motion history is an important consideration. The proposed method did not neglect the effect of motion history entirely, since the motion history is somewhat represented by u , a and I , where I is directly related to the "displacement ratio" cited by Garrison. It is fair to say that a more complete representation of motion history is needed for further advancing the state-of-the-art on wave force calculation. However, the lack of a detailed representation on particle motion history (which is common in most research works on the related subject) should not overshadow the key points taken in the paper. It was not the intention of this paper to correlate the drag and inertia coefficients with the Reynolds number and Iversen's Modulus based on instantaneous fluid kinematics. The suggestion of the paper was to bypass the step of using the Morison's equation altogether. Eqs. 7 and 8 were used to illustrate the fact that the proposed method is more general than the Morison's approach. In other words, if one accepts the use of Morison's equation with a given pair of C_d and C_m , Eq. 7 should indicate that the dimensionless force $\phi_1(t)$ is a linear function of I with C_m being the slope and C_d the intercepts. The relationship between ϕ_2 and I , as shown in Eq. 8, constitutes a hyperbolic function. This suggests that a plot of ϕ_1 or ϕ_2 versus I for various R can be made to calculate the C_d and C_m if Morison's equation is applicable. The intent of this discussion is to demonstrate that the Morison's equation falls within the domain of the proposed method. But, the purpose of the paper was to encourage the use of the alternate procedure as proposed, which is to analyze wave force data based on Eqs. 5 and 6 without using C_d , C_m , and Morison's equation. The proposed approach simplifies the data analysis procedure because the direct measurement of wave kinematics may be used to correlate with wave force data without relying upon any wave theories. In addition, the results of simulation may be applied to design problems in a more direct manner. For example, in many instances the water particle kinematics may be measured rather easily during an offshore

^aFebruary, 1980, by Yuan Jen (Proc. Paper 15166).

³Dir. of Ocean Engrg., Dr. Maxwell C. Cheung & Assoc., 2081 Business Center Drive, Suite 110, Irvine, Calif. 92715.

drilling operation while the measurement of waves is more difficult. The proposed alternate procedure would allow wave force calculations to be made directly from the measured wave kinematic data and subsequently applied to the design of production facilities at the same site.

PERTURBATION METHODS IN DIFFRACTION^a

Closure by John V. Wehausen³

The existence of a formal second-order solution may not be in contention, as Isaacson states, but his original article (1) appeared to imply that it was of doubtful use because of the line of singularities. In fact, the crucial point does not concern just second-order solutions but the whole procedure, starting with first-order solutions, for each order yields a linear problem like the one discussed in the original paper. Only under special circumstances can one avoid these logarithmic singularities, and higher-order approximations cannot cancel those that occur earlier. Situations where the latter seems to occur are not really similar. Fortunately, one is generally interested in integrated pressures, so that finite values for force and moment result. Similarly, the leading-edge singularity in thin-wing theory does not prevent it from giving useful results for the lift even though the pressure distribution is incorrect near the leading edge.

The possible occurrence in the linearized problem of a logarithmic singularity at the intersection of the equilibrium free surface and boundary walls was already pointed out in 1910 by J. Hadamard (8), and further elaborated by G. Bouligand (9,10). In his second paper, Bouligand claims to prove that there are also singularities in the "exact" problem, but the writer finds the proof obscure. In the exact problem for a flapper wave-maker, there must, however, be a singularity at the intersection of the flapper and the bottom, just as in the linearized case.

Since submission of the writer's note the logarithmic character of the singularity has been confirmed by Miloh (11) and a solution to the second-order problem worked out for infinite depth by J. N. Hunt and R. E. Baddour (12,13).

APPENDIX.—REFERENCES

8. Hadamard, J., "Sur les Ondes Liquides," *C. R. Acad. Sci. Paris*, Vol. 150, 1910, pp. 609-611, 772-774.
9. Bouligand, G., "Sur les Équations des Petits Mouvements de Surface des Fluides Parfaits," *Bulletin de la Société Mathématique de France*, France, Vol. 40, 1912, pp. 149-180.

^aMay, 1980, by John V. Wehausen (Proc. Paper 15385).

³Prof. of Engrg. Science, Coll. of Engrg., Dept. of Naval Architecture and Offshore Engrg., Univ. of California, Berkeley, Calif. 94720.

10. Bouligand, G., "Sur les singularités à la paroi dans le problème des ondes liquides," *Bulletin des Sciences Mathématiques*, France, Vol. 40, 1926, pp. 89-96, 106-112.
11. Miloh, T., "Irregularities in Solutions of Nonlinear Wave Diffraction Problem by Vertical Cylinder," *Journal of the Waterway, Port, Coastal and Ocean Division*, ASCE, Vol. 106, WW2, Proc. Paper 15385, May, 1980, pp. 279-284.
12. Hunt, J. N., and Baddour, R. E., "Second-Order Standing Waves Bounded by Circular Cylinders," *Journal of the Waterway, Port, Coastal and Ocean Division*, ASCE, Vol. 106, WW1, Proc. Paper 15166, Feb., 1980, pp. 122-127.
13. Hunt, J. N., and Baddour, R. E., "Nonlinear Standing Waves Bounded by Cylinders," *Quarterly Journal of Mechanics and Applied Mathematics*, London, England, Vol. 33, No. 3, 1980, pp. 357-371.

Errata.—The following correction should be made to the original paper:

Page 290, paragraph 1, line 3: Should read "be an imposed pressure distribution and $z = Z(r, \theta)$, $r > a$, the equation" instead of "be the equation"

WAVE PROPULSION OF SPAR BUOYS^a

Discussion by R. M. Carson²

A number of experiments using model spar buoys have been conducted in the regular waves of a wave tank at the Institute of Oceanographic Sciences. The buoys often showed a velocity significantly different from that of a small surface marker, or of a dye streak. In many cases the buoy moved faster than the surface marker, but sometimes slower, and on occasion it actually moved toward the wavemaker, against the direction of wave propagation. The internal currents in the tank were not responsible; dye streaks in the water showed that the return circulation which accompanies wave action in a tank was well below the buoy at all times.

The explanation of these apparently paradoxical drift velocities seems to lie in the dynamics of the buoy relative to the water surface; these effects are over and above the effect detailed in the original paper. Both heave and pitch motions are important.

The buoy motion in regular waves can be characterised by ω_h and ω_p , the natural frequencies of the buoy in heave and pitch respectively, and by the wave excitation ω . In Fig. 3 the expected buoy response is shown diagrammatically for some alternative combinations of these frequencies. The amplitudes are of course purely schematic.

Two main consequences emerge:

^aAugust, 1980, by Thomas A. McClimans (Proc. Paper 15592).

²Sr. Lect., Dept. of Mechanical Engrg., Univ. of Nairobi, P.O. Box 30197, Nairobi, Kenya; formerly Lect. Inst. of Oceanographic Sciences, Wormley, Godalming, Surrey, United Kingdom.

1. With the sole exception of case A, the draft of the buoy is increased at the wave crest and reduced at the trough. This will lead to a reduction in the buoy velocity at the crest, and an increase at the trough. In turn this will reduce the effect described by the author.

2. With the exception of case A, the buoy possesses a vertical component of velocity relative to the water; this is especially marked when $\omega > \omega_h$. Further, the buoy may be at a large pitch angle to the vertical when the relative velocity is a maximum. In this case the relative flow will result in a horizontal component of force on the buoy—the lift force of a yawed cylinder. By inspection this

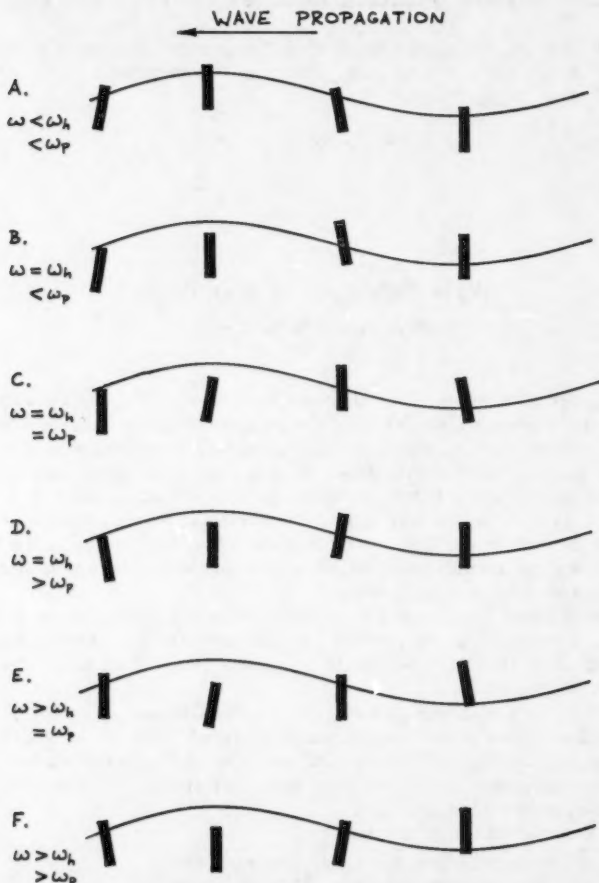


FIG. 3.—Spar Buoy Motion in Regular Waves

force is in the direction of wave propagation in case B, but against the wave in cases C, D, and F.

The experimental results do not permit a proper evaluation of these ideas; however, one case is suggestive. A pair of identical buoys were ballasted to the same value of draft, but were given different values of pitch inertia. When these models were tested side by side in the same regular wave field, it was found possible to make first one, and then the other proceed faster along the tank, depending on the wave frequency chosen. This can only be due to their pitch characteristics.

A further trial was performed at sea, using spar buoy drifters in a current meter evaluation (4). Floats of markedly different pitch characteristic showed very little separation when tracked together over periods of one and of two tidal cycles, which suggests that wave propulsion was not significant. This negative result may show that the resonance effects which are all too obvious in the regular wave train of a tank become less important in a real seaway. This may be due to the fairly sharp resonance (high Q) of the buoy response.

APPENDIX.—REFERENCE

4. Collar, P. G., "Near-Surface Current Measurement from a Surface Following Data Buoy (DB 1)—I," *Ocean Engineering*, Vol. 5, 1978, pp. 181-196.

LONGSHORE CURRENTS WITH WAVE CURRENT INTERACTION^a

Discussion by A. Swain²

The author is to be complimented for an interesting paper. However, the writer would like to clarify a few errors and extend the study to unsteady flow.

The unsteady longshore momentum equation, in the absence of body forces, can be written as

$$\frac{d}{dt}(\rho Vd) = \tau_{by} + \frac{d}{dx}(S_{xy}) \dots \dots \dots (22)$$

and the unsteady onshore-offshore momentum equation, without body forces, is

$$\frac{d}{dt}(\rho u d) = -\frac{d}{dx}(\rho g \bar{\eta}) - \left[\bar{\tau}_{bx} + \frac{d}{dx}(S_{xx}) \right] \dots \dots \dots (23)$$

^a August, 1980, by Robert A. Dalrymple (Proc. Paper 15592).

² Research Hydr. Engr., Wave Dynamics Div., United States Army Engineers, WES, P.O. Box 631, Vicksburg, Miss. 39180.

in which u = onshore-offshore velocity. Using the author's definition sketch for the coordinate axes, Eqs. 1, 3, 6 and 7, and the following equations

$$KC = K_{\infty} C_{\infty} + K_{\infty} V \sin \theta_{\infty} \dots (24)$$

$$\frac{d\theta}{dx} = \frac{\frac{1}{\cos \theta} \left[\frac{C}{\sin \theta} \frac{dc}{dx} - C \frac{dV}{dx} \right]}{\left(\frac{C}{\sin \theta} \right)^2} \dots (25)$$

$$\frac{dE}{dx} = \frac{1}{4} \rho g \kappa^2 d \frac{d(d)}{dx} \dots (26)$$

$$\frac{dC}{dx} = \left(\frac{g}{2C} \right) \frac{d(d)}{dx} \dots (27)$$

$$\frac{d(d)}{dx} = \frac{dh}{dx} + \frac{d\bar{\eta}}{dx} \dots (28)$$

$$U_m = \sqrt{\frac{2E}{\rho d}} = \frac{1}{2} \kappa C \dots (29)$$

Eq. 22 becomes

$$\begin{aligned} \frac{8\pi d}{f\kappa C} \cos \theta \frac{dV}{dt} &= V(1 + \sin^2 \theta) \cos \theta - \frac{\pi \kappa d}{f} \sin^2 \theta \cos 2\theta \frac{dV}{dx} \\ &+ \frac{\pi \kappa C}{f} \frac{d(d)}{dx} \sin 3\theta \dots (30) \end{aligned}$$

Eq. 30 represents the unsteady form of the longshore momentum equation. This equation can be solved analytically to predict the variation of longshore velocity with time. Note that for steady flow $dV/dt = 0$, and if the trigonometrical identities

$$\cos 2\theta = 1 - 2 \sin^2 \theta \dots (31)$$

$$\text{and } \sin 3\theta = 3 \sin \theta - 4 \sin^3 \theta \dots (32)$$

are used in Eq. 30, the later reduces to the author's Eq. 9, except the term $5 \sin \theta - 6 \sin^3 \theta$, which is an error in Eq. 9, must read $3 \sin \theta - 4 \sin^3 \theta$. In addition if we consider the bottom slope, m , to be constant, and neglect wave setup or wave set-down.

$$\frac{d(d)}{dx} = \frac{dh}{dx} = m \dots (33)$$

Eq. 30 reduces to the following linear differential equation

$$\frac{dV}{V(1 + \sin^2 \theta) \cos \theta + \frac{\pi \kappa C m \sin 3\theta}{f}} = \frac{f}{\pi \kappa m \sin^2 \theta \cos 2\theta} \frac{dx}{x} \dots (34)$$

Using the boundary conditions at $x = x_B$, $V = V_o$, in which x_B = width of the surf zone; and V_o = the longshore velocity at the outer limit of the surf zone, and integrating Eq. 34, gives

$$V = V_o \left(\frac{x}{x_B} \right)^P + \frac{\pi \kappa C m \sin 3\theta}{f \cos \theta (1 + \sin^2 \theta)} \left[\left(\frac{x}{x_B} \right)^P - 1 \right] \dots \dots \dots (35)$$

$$\text{in which } P = \frac{f \cos \theta (1 + \sin^2 \theta)}{\pi \kappa m \sin^2 \theta \cos 2\theta} \dots \dots \dots (36)$$

Eq. 35 represents the distribution of longshore currents in the surf zone for a constant beach slope. Likewise carrying out the derivatives of Eq. 23 and

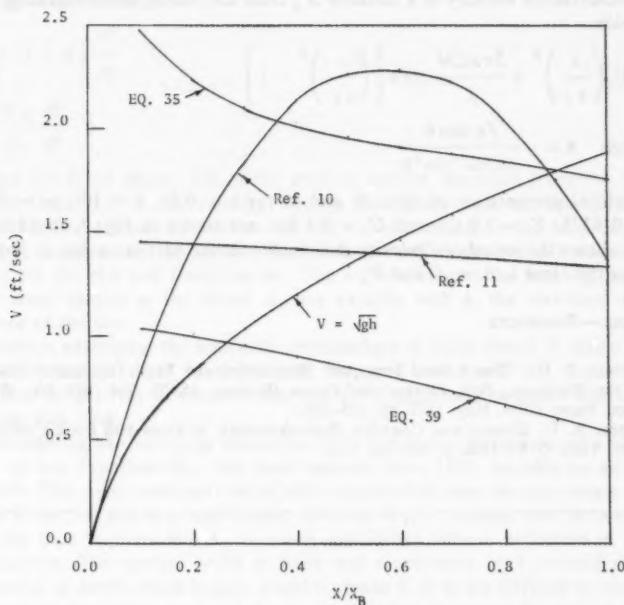


FIG. 3.—Distribution of Longshore Current (1 ft = 0.3048 m)

substituting Eqs. 25–29 into Eq. 23, the unsteady onshore-offshore momentum equation is

$$\begin{aligned} \frac{d}{C} \frac{du}{dt} + C \frac{d(d)}{dx} \left(1 + \frac{3\kappa^2}{8} \cos^2 \theta \right) &= C \frac{dh}{dx} - \frac{f\kappa V}{16\pi} \sin 2\theta \\ - \frac{\kappa^2}{4} \frac{d}{dx} \sin^3 \theta \frac{dV}{dx} &\dots \dots \dots (37) \end{aligned}$$

For steady flow $du/dt = 0$, and since $\sin 2\theta = 2 \sin \theta \cos \theta$, Eq. 37 reduces to the author's Eq. 8, except in that the term $(k^2 d/4) \sin^3 \theta (dv/dx)$ must be negative, which is an error. Eq. 37 can predict analytically the variation of onshore-offshore unsteady velocity distribution.

In addition, if we consider steady flow, neglect wave-setup or wave set-down, and use Eq. 33, Eq. 37 reduces to a linear differential equation of the form

$$\frac{dV}{\frac{3}{8} CM \kappa^2 \cos^2 \theta + \frac{f \kappa V \sin 2\theta}{16\pi}} = -\frac{4}{\kappa^2 M \sin^3 \theta} \frac{dx}{x} \dots \dots \dots (38)$$

Utilizing the boundary conditions at $x = X_B$, $V = U_o$, in which U_o = the onshore-offshore velocity at a distance X_B from the beach, and integrating Eq. 38 yields

$$V = U_o \left(\frac{x}{x_B} \right)^R + \frac{3\pi \kappa CM}{f} \cot \theta \left[\left(\frac{x}{x_B} \right)^R - 1 \right] \dots \dots \dots (39)$$

$$\text{in which } R = -\frac{f \kappa \cos \theta}{2\pi M \kappa^2 \sin^2 \theta} \dots \dots \dots (40)$$

A graphical presentation of Eqs. 35 and 40 for $k = 0.78$, $\theta = 10^\circ$, $m = 0.02$, $f = 0.018375$, $V_o = 3.0$ fps and $U_o = 0.3$ fps, are shown in Fig. 3. In addition Fig. 3 shows the longshore velocity distribution in the surf zone due to Komar (10) for the same k , θ , m , f , and V_o .

APPENDIX.—REFERENCES

10. Komar, P. D., "Beach Sand Transport: Distribution and Total Transport," *Journal of the Waterway, Port, Coastal and Ocean Division*, ASCE, Vol. 103, No. WW2, Proc. Paper 12916, May, 1977, pp. 225-239.
11. Ippen, A. T., *Estuary and Coastline Hydrodynamics*, McGraw-Hill Book Company, New York, N.Y., 1966, p. 425, Eq. 9.21.

WATER LEVEL VARIATIONS ALONG CALIFORNIA COAST^a

Discussion by Morrough P. O'Brien,³ Hon. M. ASCE

The data presented in the original paper seem to confirm the conclusion reached by Douglas W. Johnson (13) many years ago, namely that the elevation of mean sea level at any location depends upon the hydrography of the connection

^aAugust, 1980, by Raymond A. Smith and Robert J. Leffler (Proc. Paper 15614).

³Dean Emeritus and Prof. of Engrg. Emeritus, Dept. of Civ. Engrg., Coll. of Engrg., 412 O'Brien Hall, Univ. of California, Berkeley, Calif. 94720.

between the gage and the open ocean, and that the effect of the intervening hydrography may vary with time due to natural or man-made changes.

The paper does not specify the precise location of the tide gages considered, but the general character of their exposure to the open-ocean tide is known. In Fig. 5, the gage at San Diego, located inside the entrance, shows a rise in sea level with time, whereas the gages at Avila, Santa Monica, and Los Angeles, located in or near open ocean conditions, show a nearly constant level. The gage at Crescent City, representing nearly open ocean conditions, showed no change with time whereas the gage at San Francisco, located at the throat of the Golden Gate, showed a steady rise with time.

The hydraulic regimen, which determines the water surface elevation at the throat of an entrance, may be represented with simplifying assumptions by two equations, namely

$$\Delta H = (1 + K) \frac{V^2}{2g} \dots \dots \dots (2)$$

$$V = \frac{A_B}{A_C} \frac{dh}{dt} \dots \dots \dots (3)$$

During the flood phase, ΔH is the drop in surface elevation from the ocean to the throat, V is the velocity through the throat section, and K is the corresponding friction coefficient; on the ebb phase, ΔH is the drop between the bay surface and the throat. The friction coefficients are not necessarily equal for the ebb and flood phases. The surface area of the bay A_B and the flow cross section at the throat A_C are variable with h , the elevation of the surface of the bay.

Without examining the hydraulic relationships in more detail, it seems clear the difference in mean level between the open ocean and the throat of an entrance is: (1) Not obviously zero; and (2) depends on variables which may change with time.

Considering the tide-gage record at Fort Point, San Francisco, the surface area of San Francisco Bay has been reduced since 1855, possibly by as much as 30%. The cross-sectional area of this entrance falls near the area-prism curve of O'Brien (14) and is in equilibrium, the ratio A_B/A_C should then be constant, but the time required for A_C to reach equilibrium after a reduction in A_B is not known. The surface width is fixed and a reduction in A_C would require reduction in depth which in turn would increase K . It is not difficult to visualize changes in the surface area and the channels of San Francisco Bay which would account for the observed increase in the mean level as in Fig. 5.

These notes are an inadequate treatment of a subject which deserves much theoretical and experimental study. The temporal trend, and the causes, of sea level changes is an important consideration in coastal zone planning, but the data available are ambiguous. One clear requirement is an increase in the number of open-ocean tide gages.

APPENDIX.—REFERENCES

13. Johnson, D. W., "Studies of Mean Sea-Level," *Bulletin of the National Research Council*, No. 70, July, 1929.

14. O'Brien, M. P., "Equilibrium Flow Areas of Tidal Inlets on Sandy Coasts," *Coastal Engineering*, Vol. I, ASCE, New York, N.Y., 1967, pp. 676-686.

KNICKPOINT MIGRATION DUE TO BASELEVEL LOWERING^a

Discussion by Saburo Komura,⁴ M. ASCE

The authors' extension of the application of the heat diffusion equation to a head-cut process is very interesting, but practical application is limited because it requires the user to estimate the so-called "diffusion coefficient." In fact, diffusion coefficient is unknown and depends on the characteristics of water flow, sediment transport and so on. The writer believes that in the original paper there is considerable room for improvement in the theoretical development of very complex head cut process. In this discussion, the writer will concentrate on the determination method of diffusion coefficient for the head-cut migration process.

Substituting Eq. 17 into Eq. 15, the following equation of motion of a headcut is obtained:

$$\omega = \frac{jk}{\sqrt{\pi kt}} \exp \left[-\left(\frac{x}{2\sqrt{kt}} \right)^2 \right] + \frac{bk}{h} \dots \dots \dots (19)$$

in which $\omega = dx/dt$ (propagation velocity of headcut); $j = Y_0/h$ which is determined by the outlet conditions; and $b =$ the initial bed slope. The writer believes the second term of Eq. 18 should read bk/h instead of bk . From Eq. 19, the following dimensionless expression can be obtained:

$$\frac{\omega h}{k} = \frac{j}{\sqrt{\pi} \left(\frac{\sqrt{kt}}{h} \right)} \exp \left\{ - \left[\frac{\frac{x}{h}}{2 \left(\frac{\sqrt{kt}}{h} \right)} \right]^2 \right\} + b \dots \dots \dots (20a)$$

Taking \sqrt{kt}/h as a parameter, the relationship between $\omega h/k$ and x/h can be expressed as shown in Fig. 19. The equation of envelope appeared in Fig. 19 was obtained from the following two equations:

$$F \left(\frac{\omega h}{k}, Y, \frac{x}{h} \right) = 0 \dots \dots \dots (20b)$$

^aAugust, 1980, by Ze'ev B. Begin, David F. Meyer, and Stanley A. Schumm (Proc. Paper 15651).

⁴Prof., Dept. of Civ. Engrg., Gifu Univ., Kagamigahara, Gifu, Japan.

$$\text{and } F' Y \left(\frac{\omega h}{k}, Y, \frac{x}{h} \right) = 0 \quad \dots \dots \dots (21)$$

in which $Y = \sqrt{kt}/h$. Differentiating Eq. 20a with respect to Y , the parametric equation is obtained:

$$\frac{x}{h} = \sqrt{2} Y \quad \dots \dots \dots (22)$$

$$\text{or } Y = \frac{\frac{x}{h}}{\sqrt{2}} \quad \dots \dots \dots (23)$$

Substituting Eq. 22 into Eq. 20a

$$\frac{\omega h}{k} = \frac{j}{\sqrt{\pi e} \left(\frac{\sqrt{kt}}{h} \right)} + b \quad \dots \dots \dots (24)$$

in which e = the base of natural logarithms. Also, substituting Eq. 23 into Eq. 24, the equation of envelope is obtained:

$$\frac{\omega h}{k} = j \sqrt{\frac{2}{\pi e}} \left(\frac{h}{x} \right) + b \quad \dots \dots \dots (25a)$$

For $j = 2.0$, Eq. 25a becomes

$$\frac{\omega h}{k} = \frac{0.968}{\frac{x}{h}} + b \quad \dots \dots \dots (25b)$$

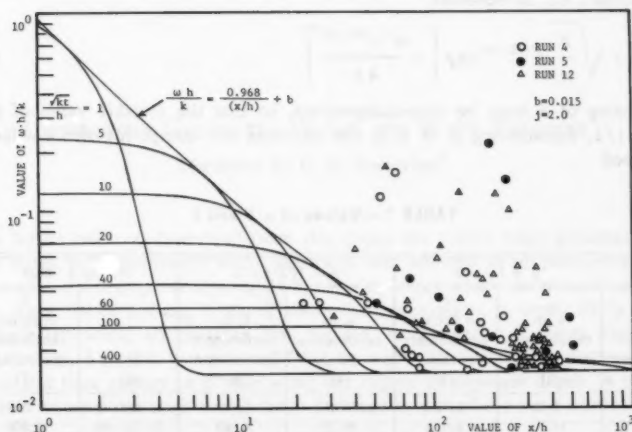


FIG. 19.—Relationship between $\omega h/k$ and x/h with \sqrt{kt}/h

Observation results on head-cut migrations can be expressed in the following general form:

$$x = \alpha t^\beta \quad (26)$$

Propagation velocity ω is obtained by differentiating Eq. 26 with respect to t

$$\omega = \frac{dx}{dt} = \alpha \beta t^{\beta-1} \quad (27)$$

By using Eqs. 26 and 27, Eq. 19 becomes

$$\alpha \beta = j \sqrt{\frac{k}{\pi}} t^{(1/2-\beta)} \exp \left[-\frac{\alpha^2 t^{(2\beta-1)}}{4k} \right] + \left(\frac{k b}{h} \right) t^{(1-\beta)} \quad (28)$$

The value of k should be time-independent, however for small value of t , the k -value obtained from this equation will be time-dependent. On the other hand, for $\beta = 1$ and a large value of t

$$j \sqrt{\frac{k}{\pi}} \exp \left(-\frac{\alpha^2 t}{4k} \right) << \frac{k b}{h} \quad (29)$$

$$\text{and } j \sqrt{\frac{k}{\pi}} \exp \left(-\frac{\alpha^2 t}{4k} \right) \rightarrow 0 \quad (30)$$

Accordingly, the following equation is obtained:

$$k \cong \frac{\alpha h}{b} \quad (31)$$

When the x -axis is taken along the initial bed surface, or $b \cong 0$ (very small bed slope), Eq. 28 becomes

$$\alpha \beta = j \sqrt{\frac{k}{\pi}} t^{(1/2-\beta)} \exp \left[-\frac{\alpha^2 t^{(2\beta-1)}}{4k} \right] \quad (32)$$

The value of k must be time-independent, so that the suitable value of β is $\beta = 1/2$. Substituting $\beta = 1/2$, the equation for computing the k -value is obtained

TABLE 1.—Values of α , β and k

Run number (1)	$\beta = 1, j = 2$		$\beta = 1/2, j = 2$		Author's Value	
	α , in centimeters per minute (2)	k , in square centimeters per minute (3)	α , in centimeters per minute ^{1/2} (4)	k , in centimeters per minute (5)	α (β) (6)	k , in square centimeters per minute (7)
4	5.42	1,720	56.45	1,650	23.4(0.69)	800
5	16.20	4,050	99.75	5,140	61.7(0.64)	1,800
11	3.67	1,320	39.63	810	—	500
12	5.18	1,300	65.08	2,190	—	1,000

$$k = \pi \left(\frac{\alpha}{2j} \right)^2 \exp \left(\frac{\alpha^2}{2k} \right) \dots \dots \dots (33)$$

Given values of j and α , a time-independent k -value can be obtained by trial and error. The initial value of k for a trial-and-error method can be estimated from the equation:

$$k = \frac{\alpha^2}{2} \dots \dots \dots (34)$$

This equation was obtained from Eqs. 22 and 26, i.e., $x = \sqrt{2kt} = \alpha t^\beta$, since $\beta = 1/2$. Table 1 shows values of α , β and k . It would be interesting to note that the authors' values of k are very small compared with the writer's values. The authors' data were analyzed by using Eqs. 31 and 33, and data for $b = 0.015$ (Run 4, 5, and 12, and $\beta = 1$) were plotted in Fig. 19.

Finally, the writer would like to mention the terminal time and distance of headcut. Assuming that $\omega h/k$ at the terminal time t_f has a value equal to $p\%$ greater than b . Using Eq. 24

$$t_f = \frac{100^2}{\pi e k} \left(\frac{j h}{p b} \right)^2 = \frac{1,171}{k} \left(\frac{j h}{p b} \right)^2 \dots \dots \dots (35)$$

The value of p would be 10% or so. Also, from Eq. 25a, the terminal distance x_f of headcut is given by

$$x_f = 100 \sqrt{\frac{2}{\pi e}} \left(\frac{j h}{p b} \right) = 48.4 \left(\frac{j h}{p b} \right) \dots \dots \dots (36)$$

LABORATORY GENERATED WAVES AND WAVE THEORIES^a

Discussion by D. H. Peregrine²

As far as one can determine from this paper the waves were generated in deep water by a pneumatic wave generator and allowed to propagate over a region of variable depth onto a region of constant depth where the measurements were made. Since nothing is stated about their generation, it seems likely that a simple sinusoidal air pressure was applied. It is clear, e.g., from Figs. 4, 5, 8(a), 8(b), 8(c) that the waves do not correspond to uniformly propagating waves and thus change in profile along the region of constant depth. A more valuable comparison with the theories for regular periodic waves would have

^aAugust, 1980, by Subrata K. Chakrabarti (Proc. Paper 15644).

²Reader in Mathematics, School of Mathematics, Univ. of Bristol, University Walk, Bristol BS8 1TW, England.

been obtained if some attempt to make them regular had been made, e.g., see Hansen and Svendsen (10). Otherwise, as the author states in his final sentence, the data refers only to the particular configuration of that tank.

The comparisons with theory clearly show that the author has failed to realize that in order to specify a wave solution completely the mean flow and mean depth must be determined as well as a suitable set of wave parameters. The difficulty this neglect has lead to is clearly evident in the comparisons of the profiles of u_{\max} and p_{\max} in Figs. 8(a), 8(b), and 8(c) where it is clear that the "theoretical" lines all correspond to different values of these mean quantities. The importance of clearly defining the mean flow, or equivalently the reference frame, for which theoretical work is developed has been recognized since Stokes (12) drew attention to it. More recently Jonsson (11) has drawn attention to its importance. The set-up and set-down due to water waves propagating from one depth to another is also a well known phenomenon, e.g., see Bowen, et al. (9).

APPENDIX.—REFERENCES

9. Bowen, A. J., Inman, D. L., and Simmons, V. P., "Wave 'Set-Down' and 'Set-Up,'" *Journal of Geophysical Research*, Vol. 73, 1968, pp. 5479-5490.
10. Hansen, J. B., and Svendsen, I. A., "Laboratory Generation of Waves of Constant Form," *Coastal Engineering*, Vol. I, ASCE, New York, N.Y., 1974, pp. 321-339.
11. Jonsson, I. G., "Energy Flux and Wave Action in Gravity Waves Propagating on a Current," *Journal of Hydraulic Research*, Vol. 16, 1978, pp. 223-234.
12. Stokes, G. G., "On the Theory of Oscillatory Waves," *Transactions of the Cambridge Philosophical Society*, Vol. 8, 1847, pp. 441-445.





